Magnetic trapping of transition-metal and rare-earth atoms using buffer-gas loading

A thesis presented

by

Cindy Irene Hancox

to

The Department of Physics

in partial fulfillment of the requirements

for the degree of

Doctor of Philosophy

in the subject of

Physics

Harvard University

Cambridge, Massachusetts

May 2005

To my mom

Thesis advisor

John Morrissey Doyle

Author

Cindy Irene Hancox

Magnetic trapping of transition-metal and rare-earth atoms using buffer-gas loading

Abstract

We report on the magnetic trapping of new species of transition-metal and rare-earth atoms using buffer-gas loading. This thesis details the results from two experiments. In the first experiment, we investigate the Zeeman relaxation rate in cold collisions of transition-metal (TM) and rare-earth (RE) atoms with He. The RE and TM atoms chosen for this study are in non-S-states, that is, they have finite orbital angular momentum and non-spherical electronic density distributions. The interaction anisotropy between non-S-state atoms and a collision partner may drive Zeeman relaxation via inelastic collisions. We find, however, that inelastic collisions are dramatically suppressed for transition-metal Ti and rare-earth atoms Pr, Nd, Tb, Dy, Ho, Er and Tm due to the unpaired electrons being "submerged" beneath a filled outer s shell. We successfully trap all of the rare-earth atoms studied. In addition to Ti, we also attempt to measure the inelastic collision rates for Sc, Y and Zr. We are only able to place a lower limit on the inelastic collision cross sections for Sc-He and Y-He collisions. We are unable to measure the inelastic collision cross section for Zr-He collisions due to inconsistent Zr ablation yields. In the second experiment, we trap and evaporatively cool atomic molybdenum. We observe two-body decay from the trap and determine the inelastic Mo-Mo collision rate.

Contents

List of Figures

List of Tables

Citations to Previously Published Work

Portions of this thesis have appeared previously in the following papers:

"Magnetic trapping of rare-earth atoms at milliKelvin temperatures", Cindy I. Hancox, Stephen C. Doret, Matthew T. Hummon, Linjiao Luo, and John M. Doyle, *Nature* **431**, 281–284 (2004).

"Suppression of angular momentum transfer in cold collisions of transition metal atoms in ground states with nonzero orbital angular momentum", Cindy I. Hancox, Stephen C. Doret, Matthew T. Hummon, Roman Krems, and John M. Doyle, *Physical Review Letters* **94**, 013201 (2005).

"Evaporative cooling of magnetically trapped atomic molybdenum", Cindy I. Hancox, Matthew T. Hummon, Scott V. Nguyen, and John M. Doyle, *Physical Review A* **71**, 031402 (2005).

Acknowledgements

First of all, I would like to thank my thesis advisor, John Doyle, for his support and encouragement during my time as a graduate student and for providing an exciting and friendly research environment to work in.

I have had the privilege of working with interesting and talented individuals throughout my time in graduate school. I had a great experience working with Jonathan Weinstein and Rob deCarvahlo during my first years in the lab. Jonathan and Rob are exceptional scientists and exceptional teachers. I couldn't ask for a better pair of folks to learn the ropes from. I gratefully acknowledge Charlie Doret and Matt Hummon for their work on the non-S-state atom experiments. The measurements presented in this thesis are as much a result of their efforts as mine. I thank Matt (again) and Scott Nguyen for their work on the molybdenum experiment. I am grateful to Roman Krems for the many hours he spent talking to me about cold collisions. I am much obliged to the above mentioned and the remaining members of the Doyle group who are too numerous to name for making life in the lab a lot of fun.

Warm thanks to my former roommates, Christina Molodowitch, Stephanie Yang, and Tanya Zelevinsky for all of the fun memories and for their continued friendship. I would also like to gratefully acknowledge the other good friends I have made here in Cambridge: Parisa Fallahi, Linjiao Luo, Bob Michniak, Melissa Wessels, and Shiyamala Thambyahpillai. I have spent a really good 6 years here and have you folks to thank in large part. I would also like to thank my best friend from college, Sabine Airieau, for her continued support and care.

I would like to thank my sisters Karen and Miyuki, my brother Jimmy, and my brother-in-law Tim for their encouragement through the years. I would like to thank

my mom for the lifelong love and support she has given me. I would not be in graduate school if not for the unbounded enthusiasm she has always shown for my education and for the help she is always ready to give. Finally, I thank my husband, Chip, for making my time in graduate school truly enjoyable and for taking such good care of me while I wrote this thesis.

Chapter 1

Introduction

In this thesis, we report on two experiments aimed at extending the scope of ultracold atom physics to new systems and understanding the general questions of how atoms act in collisions at low temperatures. We report on the suppression of interaction anisotropy in complexes of non-S-state (non-spherical atoms with finite orbital angular momenta) transition-metal and rare-earth atoms with helium. The resulting suppression of inelastic collisions enables us to magnetically trap the non-S-state lanthanides using buffer-gas loading. We also report on the magnetic trapping and evaporative cooling of S-state-atom molybdenum.

1.1 Extending the scope of ultracold atomic physics

Twenty years after the first demonstration of magnetic trapping [1] and ten years after the first observations of Bose-Einstein condensation in atomic vapors [2, 3, 4], new discoveries in the field of ultracold atomic physics continue apace. The past three years alone have yielded several new milestones, including the realization of long predicted BEC of molecules [5, 6, 7, 8], Bosonization of a Fermi gas [7], atom-

atom entanglement [9], and the accurate measurement of the Casimir force in atom - surface interactions [10].

While the field continues to grow, cooling and trapping experiments remain constrained to relatively few species. The prevalence of laser cooling has largely confined the world of cold atomic physics to atoms with simple internal level structures—primarily the alkali metals, alkaline earths, and metastable states of the noble gases.[1] We wish to extend the scope of cold atomic physics across the periodic table to a host of new paramagnetic species. We believe that adding to the cold atom arsenal will aid in areas of research currently underway, such as the formation of cold polar molecules, the creation of quantum degenerate dipolar gases, quantum computing using highly magnetic atoms, and precision measurements using heavy atoms to look for physics beyond the Standard Model—as well as open up the field to discoveries yet unlooked for.

To this end, we use a laser-free method of loading atoms into a magnetic trap called buffer-gas cooling, whereby atoms are cooled to below the depth of a magnetic trap via cold collisions with a cryogenically cooled helium buffer gas [13]. This method is independent of the internal level structure of the species-to-be-trapped and relies solely on elastic collisions with He.

The generality of buffer-gas loading makes it a natural tool for co-trapping of different atomic species. Our lab is currently in a collaboration with the Kleppner and Greytak groups at MIT to co-trap Li and H with the aim of creating a BEC of hydrogen with enhanced evaporative cooling efficiency via Li-H collisions, and of creating ultracold LiH molecules via photoassociation [14]. Photoassociation of polar molecules has recently been achieved with the production of ultracold metastable

[1]Notable exceptions include the recent achievements of quantum degeneracy in Yb [11] and Cr [12].

RbCs molecules [15]. We would like to apply photoassociation to systems beyond alkali dimers. Of particular interest are heteronuclear molecules with nitrogen. Not only is N important chemically, but it can also form molecules with large dipole moments (PN has an electric dipole moment of 2.75 Debye), making it an interesting candidate for a dipolar molecular gas [16].

There is currently much interest in the creation of degenerate dipolar gases. In such systems, the interparticle interaction is dominated by long-range, anisotropic dipole-dipole (either magnetic or electric) forces rather than the short-range van der Waals interactions. New effects predicted for dipolar Bose gases include geometry-dependent stability of the condensate (*e.g.* cigar-shape traps along the dipole axis may be unstable to collapse, whereas pancake traps would be stable) and modifications to the excitation spectrum of the condensate. New phases such as the "supersolid" and "checker-board" phases are predicted for a dipolar Bose gas placed in an optical lattice [16]. This area of research recently saw a breakthrough with the achievement of BEC in a gas of Cr atoms [12]. Cr has a large magnetic moment of 6 μ_{B}. While dipolar effects have not yet been seen, it may be possible to enhance the dipolar nature of the condensate by tuning the s-wave scattering length close to zero using a Feshbach resonance [12, 17].

Previously in our lab, buffer-gas loading was used to successfully trap Cr and Eu (7 μ_{B}), in each case producing 10^{12} trapped atoms in isotopic mixtures and, in the case of Eu, multiple hyperfine states [18, 19]. Other candidates for dipolar gases include the highly-magnetic rare-earth atoms Ho (9 μ_{B}), Tb (10 μ_{B}), and Dy (10 μ_{B}). For these atoms, the magnetic dipole-dipole interaction should be roughly equal to the van der Waals interaction and dipolar effects in the condensate should be readily seen. These atoms are magnetically trapped for the first time in this thesis work,

as described in the next section. Another interesting prospect for highly magnetic atoms [20] and polar molecules [21] is to use them as qbits in a quantum computer. In both proposals, the qbits are held in an optical lattice that is placed in a field gradient to allow for individual spectroscopic addressing of each site, while the dipole-dipole interaction provides the coupling between qbits.

The application of cooling and trapping to new heavy atom systems may offer new avenues for precision measurements and may aid in high-precision spectroscopy of these atoms due to the lengthening of the interaction time. Heavy atoms are of particular interest due to the large relativistic effects reflected in their spectra. For example, Dy is used to search for changes in the fine-structure constant (α) with time thanks to an "accidental" near-degeneracy of two opposite-parity states with different energy dependencies on α [22, 23].

Finally, extending cooling and trapping to new species will greatly enrich the field of cold collisions. The production and behavior of degenerate gases depends critically on the character of the interatomic collisions. Cold and trapped atoms are interesting even at temperatures above degeneracy as often their collisional properties are poorly understood. Cold collisions are a major focus of this thesis, as described in the next two sections.

1.2 Magnetic trapping of non-*S*-state atoms

The achievement of quantum degeneracy relies on evaporative cooling of trapped atoms to produce high densities and ultracold temperatures. With few exceptions [11, 24, 25], magnetic traps are used for this purpose. Magnetic traps confine atoms in low-field-seeking states, in which the electronic magnetic moment is aligned anti-parallel to the magnetic field. This alignment must be preserved during the collisional ther-

malization of the atomic cloud. While elastic collisions drive thermalization which mediates the buffer-gas loading and evaporative cooling, inelastic collisions induce reorientation of the magnetic moment of trapped atoms to more energetically favorable high-field-seeking states (Zeeman relaxation), leading to trap loss. The effect of inelastic loss on loading and evaporative cooling efficiency can be parametrized by a single number γ, the ratio of elastic and inelastic collision rates. Depending on the value of γ, buffer-gas loading and evaporative cooling can be straightforward ($\gamma > 10^4$) or impossible ($\gamma < 10$) [26].

The value of γ is determined by the electronic interaction anisotropy between the colliding atoms. Evaporative cooling and buffer-gas loading have so far been limited to S-state atoms, *i.e.* atoms with zero electronic orbital angular momentum and spherically symmetric electronic density distributions. The electrostatic interaction between atoms in S-states is not effective in driving Zeeman relaxation since it is isotropic [27]. However, if one or both of the colliding atoms has non-zero electronic orbital angular momentum (non-S-state atom), the electronic interaction between the atoms is anisotropic [27] and the atomic angular momentum can be strongly coupled to the rotational motion of the collision complex.

Theoretical studies have shown that there is a large degree of anisotropy in the electrostatic interaction of main-group non-S-state atoms Sr*(P), Ca*(P) and O(P) [28, 29] yielding $\gamma \sim 1$. Molecular beam experiments with O and Cl ($3s^2 3p^5\ ^2P$) at high temperatures (10^3 K) have also indicated a significant degree of interaction anisotropy in complexes of these atoms with He, leading one to expect $\gamma \sim 1$ [30, 31]. Several metastable non-S-state atoms have been magnetically trapped [32, 33, 34, 35, 36]; however, theoretical and experimental results on these atoms have indicated that evaporative cooling of these atoms would generally be impossible [28, 37, 38].

We proposed that inelastic collisions would be suppressed for transition-metal and rare-earth atoms in electronic ground states with non-zero orbital angular momentum due to the non-sequential filling of the electron orbitals. In most transition-metal atoms, the unpaired electrons occupy a partially filled d shell which is shielded by a closed spherical s shell of higher principal quantum number, *i.e.* the electron configuration is given by $nd^m(n+1)s^2$. Most rare earths have the electron configuration $nf^m(n+1)s^2(n+1)p^6(n+2)s^2$— the unpaired electrons partially fill an f shell which is shielded by multiple filled shells [39]. Such atoms should appear more spherical during a collision so that Zeeman transitions would be suppressed.

The non-S-state transition-metal atoms which don't follow the above filling order have a single electron in the outer s shell rather than a closed shell, giving the configuration $nd^m(n+1)s$. The rare-earth exceptions have an unpaired electron in the d shell resulting in the configuration $nf^m(n+1)s^2(n+1)p^6(n+1)d(n+2)s^2$. These atoms may also have some suppression of inelastic collisions. For the experiments presented in this thesis, however, we concentrate on the exclusively d-shell-filling transition metals and the exclusively f-shell-filling rare earths.

In this thesis, we present measurements of cold collisions rates of transition metal atoms Sc, Ti, Y and Zr with He, and of the magnetic trapping of rare earth atoms Pr, Nd, Tb, Dy, Ho, Er, and Tm (all of the exclusively f-shell-filling lanthanides). Chapter 2 provides an overview of the experimental techniques. Chapter 3 details the data and results for the transition metal experiments. While the measurements for Sc and Y provide only lower bounds on the inelastic rates, the measurements with Ti demonstrate that inelastic collisions are indeed highly suppressed, with $\gamma \sim 10^4$. In parallel with our experimental work, *ab initio* calculations of the elastic and inelastic collision rates for Sc-He and Ti-He collisions were performed [40]. The theoretical

results are in agreement with the experimental measurements and are summarized in Chapter 4.

Our rare earth results are detailed in Chapter 5. We find that inelastic collisions with He are suppressed for all species studied, with γ ranging from 30,000 to 450,000. In each case, we magnetically trap $(0.2 - 2) \times 10^{12}$ atoms at densities of $(0.2 - 8) \times 10^{12}$ cm^{-3} and temperatures of $\sim$800 mK.

The low anisotropy of the electrostatic interaction for non-S-state transition-metal- and rare-earth-atom complexes with He suggests that the polarizabilty of these atoms is nearly isotropic and that angular momentum transfer in the atom-atom collisions must also be suppressed [41]. This is encouraging for the prospects for the evaporative cooling of these atoms to ultracold temperatures.

1.2.1 Collapse of the d and f orbitals

The submergence of the unpaired electrons in the transition-metals and rare-earths is greatly accentuated by the "collapse" of the d- and f- orbitals whereby the radial wavefunction of these electrons becomes concentrated much closer to the nucleus. This effect is well illustrated in Figure 1.1, taken from "Theoretical calculations of the d-, f-, and g-electron transition series" by Griffin, Andrew, and Cowan [42]. The authors explain,

> Of particular interest [in Figure 1.1] are the abrupt changes with Z in the effective quantum number which precede the beginnings of the various d– and f–electron transition series. In each instance, there occurs a corresponding abrupt change in the nature of the d or f wave function, consisting primarily of an abrupt contraction (or "collapse") to smaller radii.

The orbital collapse comes as a result of a second potential well that develops at small radii where there is a large effective nuclear charge. A potential barrier exists

between the two wells such that each contains an independent set of energy levels and the electron density is concentrated in only one well. For small nuclear charge, Z, the electron occupies the outer well. As Z increases, the inner well deepens until, at the beginning of each transition series, the well becomes sufficiently deep that it houses a bound state of lower energy than the outer well.

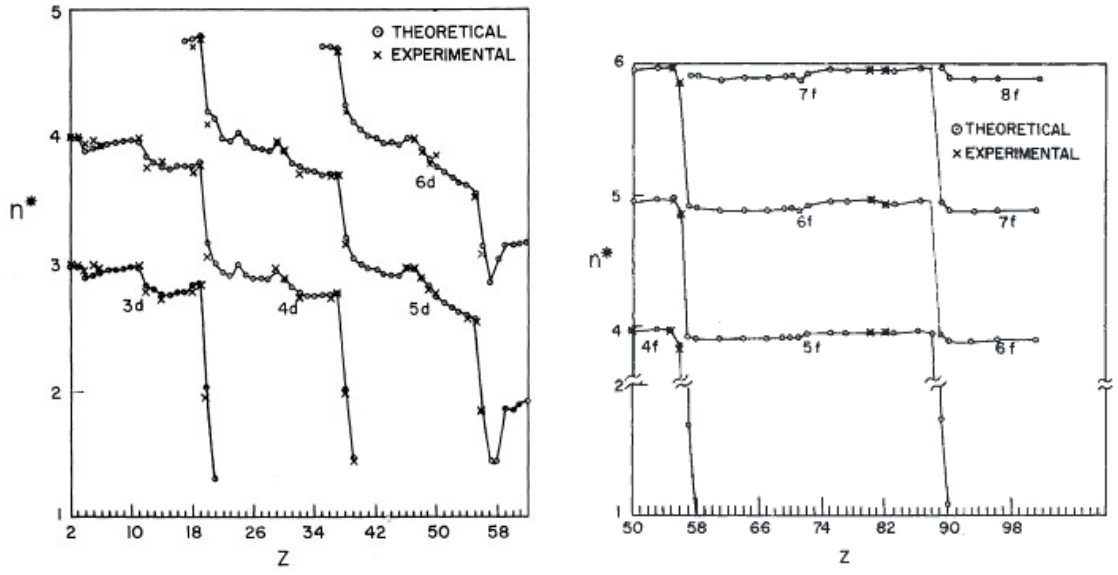

(a) d-orbital collapse (b) f-orbital collapse

Figure 1.1: Effective quantum numbers n^* for (a) d and (b) f electrons as a function of atomic number Z; $n^* = E_{\mathrm{B}}^{1/2}$, where E_{B} is the energy (in Rydbergs) to remove the d or f electron from the atom. From Reference [42].

1.3 Atomic molybdenum

Prior to our work with non-S-state atoms, we worked on the trapping and evaporative cooling of S-state transition metal atom molybdenum. Molybdenum is highly magnetic ($\mu = 6\ \mu_{\mathrm{B}}$) and has both bosonic and fermionic isotopes. Its large mag-

netic moment makes it straightforward to buffer-gas load into a magnetic trap and to achieve ample trap lifetimes for removing the buffer gas for thermal disconnect and subsequent evaporative cooling. Mo also provides an interesting comparison to atomic chromium, which is directly above Mo in the periodic table and has been previously studied in this lab.

1.3.1 Why molybdenum?

Atomic molybdenum has several features that make it an interesting candidate for an ultracold gas. Because of its large magnetic moment (6 Bohr magneton), the dipolar and van der Waals mean-field energies will be similar in a Mo Bose condensate, perhaps leading to new observable dipolar effects [16, 17, 43, 44, 45]. Mo has seven stable isotopes: two fermions and five bosons. This opens the possibility for sympathetic cooling [46, 47, 48], creation of both Fermi and Bose degenerate gases, and inter-isotope comparisons. In addition, experimental studies of cold, trapped atoms at temperatures above degeneracy can provide benchmark data for tests of collision and atomic structure theory [49]. Molybdenum is also important for a variety of studies including double beta decay [50] and biological proteins and enzymes.

As described above, inelastic collisions limit the efficiency of evaporative cooling inside a magnetic trap. Static magnetic traps confine atoms in high energy, low-field-seeking states. Inelastic spin-changing (i.e. Zeeman-state-changing) collisions lead to trap loss as atoms move to less-trapped or untrapped states. The dynamics of this loss also leads to heating [26]. It remains an open question as to whether quantum degeneracy can be reached in a magnetic trap with atoms having high magnetic moments as their inelastic spin-relaxation rates will, in general, be higher than for lower magnetic moment species (like the alkali metal atoms). So far, only atoms

with magnetic moments as high as 2 μ_B have been quantum condensed in a magnetic trap [51, 52].

A promising route for reaching degeneracy with high magnetic moment atoms is to evaporatively cool them in a magnetic trap only down to a temperature that is low enough for them to be transferred to a microwave trap [53, 54] or far-off-resonance optical dipole trap (FORT) [55]. In these types of traps the atoms are confined in the high field seeking, true ground state and evaporative cooling can be continued without inelastic loss. This was the method used in the recent achievement of Bose-Einstein condensation of Cr atoms ($\mu = 6\ \mu_{\mathrm{B}}$) [12]. In that experiment, the atoms are continuously loaded from a magneto-optical trap (MOT) into a Ioffe-Pritchard trap, where the first stage of evaporative cooling is performed. The atoms are then adiabatically transferred to an optical dipole trap for the final stage of evaporation through which degeneracy is reached with 50,000 Cr atoms remaining.

Here we report the magnetic trapping of large numbers of Mo atoms, measurement of the inelastic Mo–Mo collision rate constant, and evaporative cooling of Mo. These results are detailed in Chapter 6.

Chapter 2

Overview of non-S-state atom experiments

This chapter provides an overview of the apparatus and experiment techniques used in our non-S-state atom experiments. Briefly, transition metal (TM) or rare-earth (RE) atoms are produced via laser ablation of elemental metal targets mounted in a cell filled with a cold helium buffer gas and placed in a strong magnetic field. The atoms are observed via absorption spectroscopy, and the individual Zeeman level populations are monitored as a function of time. The relaxation of atoms from low field seeking states to lower-energy high field seeking states provides a measure of the inelastic collision rate in collisions with helium. The elastic collision rate is measured by observing the diffusion of atoms through the buffer gas at zero magnetic field. Inelastic collisions with helium are seen to be highly suppressed, allowing for the magnetic trapping of the RE atoms.

2.1 Apparatus

A new copper cryogenic cell was built as described in detail in the following section. The remaining cryogenic equipment and superconducting magnet are described in detail in the thesis of Jonathan Weinstein [56] and are only briefly reviewed here.

2.1.1 Cryogenic cell

The atoms are produced inside a 5" long, 2.7" diameter cylindrical copper cell, shown schematically in Figure 2.1. The cell is similar in design to the copper cells described in the theses of Jonathan Weinstein and Jinha Kim [56, 57] for trapping CaH and Eu, respectively. The cell is anchored to the mixing chamber of a dilution refrigerator by a 0.5" diameter, 10" long copper heat link. The heat link flares at the bottom into a flange which forms the top of the cell, and is mated to the cell walls with an indium seal. The heat link is machined out of a single piece of OFE copper and subsequently torch annealed.

Optical access to the cell is provided by a 2" diameter, 0.375" thick BK7 window mounted at the bottom of the cell. A wedged window with a 30' wedge angle is used to avoid etaloning of the probe beam. The window is sandwiched between the cell walls and a brass ring. An indium seal is made between the window and the cell walls, while an annulus of kapton sheet provides a buffer between the window and the ring below. The cell walls and bottom ring are each faced at a 15' angle to accommodate the window.

A 0.5" diameter silver-coated Pyrex mirror [58] is used to retro-reflect the probe beam is mounted at the top of the cell in a copper holder screwed onto the bottom surface of the heat link. The detection optics are described in Section 2.2. Ablation targets are glued to the interior face of the holder as described in Section 2.1.3. The

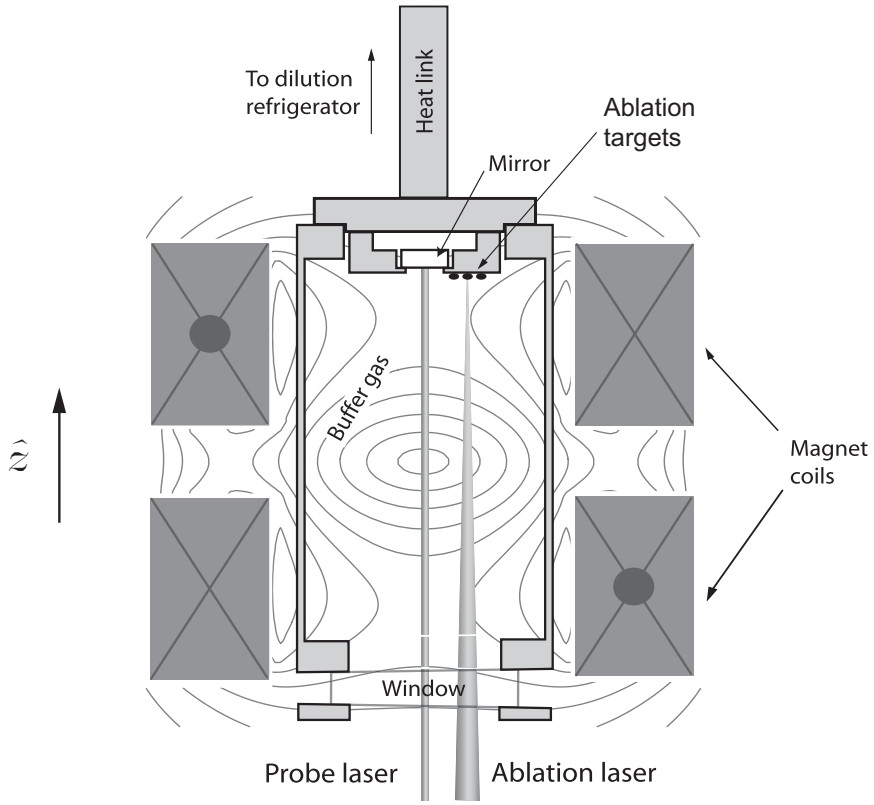

Figure 2.1: Schematic diagram of the cell.

ablation pulse is produced by a Q-switched, frequency doubled Nd:YAG laser [59]. The beam is steered by eye onto the desired ablation target using a mirror mounted just below the cryostat. Ablation pulse energies of 5-10 mJ with a 5 ns pulse length are used. Table 2.1 lists the measured ablation pulse energies for various Q-delays.

Table 2.1: Ablation pulse energies. 20 warm-up flashes used prior to each pulse.

Q-delay (μs)	Pulse energy (mJ)
325	5.7 ± 0.4
320	7.0 ± 0.4
310	9.6 ± 0.6

2.1.2 Magnet center tap

The cell is surrounded by a superconducting magnet consisting of two solenoids. The magnet was previously used to trap atomic chromium and was wired in these experiments for the anti-Helmholtz configuration for trapping (called the "new magnet" and described in detail in Jonathan Weinstein's thesis [56]). The data in the present experiment were taken in two "runs," or cooldown cycles, the first run looking at the transition metals, and the second run looking at the rare earths while also revisiting Ti. A center tap was added before the second run, allowing the magnet to be run in the Helmholtz configuration. The relatively uniform field profile produced by the Helmholtz magnet results in a sharp absorption peak for each Zeeman level, as discussed in Section 2.2.4.

The center tap was added as follows. The cask plates surrounding the magnet were removed to expose the existing soft-solder joint joining the two coils. This joint was left untouched, while a new lead was soft-soldered ∼1" away. The new lead is made of 2 mm diameter uninsulated 7:1 Cu:NbTi superconducting wire. One end of the lead was overlapped with the existing magnet wire over a length of 1.5 inches, and the two wires were wrapped tightly with smaller diameter superconducting wire. The assembly was held in place with two hemostats and soldered with 60/40 multi-core solder. The joint was then wrapped with mylar tape and helical teflon wrap. During the experiment, the magnet was successfully run Helmholtz with up to 40 A flowing through the center-tap lead (20 A in each coil), producing a field of 2.3 T in the cell.

2.1.3 Ablation targets

Target preparation

A high-purity elemental ablation target is used for each atom studied. The list of targets is given in Table 2.2. Most of the samples are procured as thin foils or as "pieces" of varying size. Squares ∼2 mm on a side are cut from each foil, and ∼ 2mm chunks are chosen or broken off from the pieces to serve as ablation targets. A whole slug is used for Ti. Each elemental target is roughened with coarse sandpaper and subsequently soaked in acetone in an ultrasonic cleaner for five minutes. The sample holder is likewise roughened with coarse sand paper and #54 holes (0.050" diameter) are drilled at each sample site prior to gluing to prevent the epoxy from shearing off during cooldown. A dab of Stycast 2860/FT epoxy is used for each target, filling each drilled hole and forming a plug which is gripped tightly by the copper during cooldown due to differential thermal contraction.

Table 2.2: Ablation targets, arranged by atomic number. [a]Cr is an S-state atom that is used in these experiments as a reference to measure the buffer-gas density in the cell (see Section 2.1.4).

Sample	purity (% REO)	geometry	stock number
Sc	99.9	0.005" foil	Alfa Aesar (AA) 00294
Ti	99.995	1/8" dia. × 1/8" length slug	AA 42394
Cr[a]	99.997	piece	AA 10151
Y	99.9	piece	AA 00615
Zr	99.8	0.02" foil	Goodfellow 046-688-35
Pr	99.9	0.01" foil	AA 10305
Nd	99.9	0.004" foil	AA 13964
Tb	99.9	0.005" foil	AA 00321
Dy	99.9	0.01" foil	AA 12381
Ho	99.9	0.01" foil	AA 10210
Er	99.9	0.01" foil	AA 12386
Tm	99.9	0.004" foil	AA 10374

Target integrity

Many of the atoms studied are reactive in their pure, elemental solid form. It was a concern that the ablation targets would oxidize during cell assembly, or that the targets would react with the epoxy used to glue them onto the sample holder.

Before the first run, test pieces were prepared for the reactive atoms (Sc, Y, and V) to be studied in that cooldown. The test pieces were each glued to a small copper slab, and the epoxy was allowed to cure in air overnight. It was found that the samples do not oxidize significantly overnight, nor indeed over 2-3 days, and that there was no adverse reaction with the epoxy.

The second run involves many more species, many of them reactive. It is found that some of these (Nd, Pr, La, and Ga) oxidize significantly over the course of a day. Therefore, for the second run, the samples are prepared and epoxied to the sample holder in air, but the holder is kept in a beaker filled with argon gas and covered with a layer of Parafilm M [60] film which was press sealed by hand around the top of the beaker while the epoxy sets. To minimize exposure, as much of the cell is assembled as possible before mounting the sample holder into the cell top and making the final indium seal between the cell top and cell walls. Once the cell is assembled, it is evacuated, filled with N_2 gas, and the buffer-gas fill line blanked off until the cell is mounted on the refrigerator. Once mounted, it is again evacuated, in preparation for cooldown.

Extra targets

Due to the long turnaround time in warm-up / cool-down cycling of the experiment, and thanks to the generality of laser ablation, we often put extra ablation targets in the cell "just in case." There is little overhead in doing so, and it leaves us with

additional options once the experiment is cold.

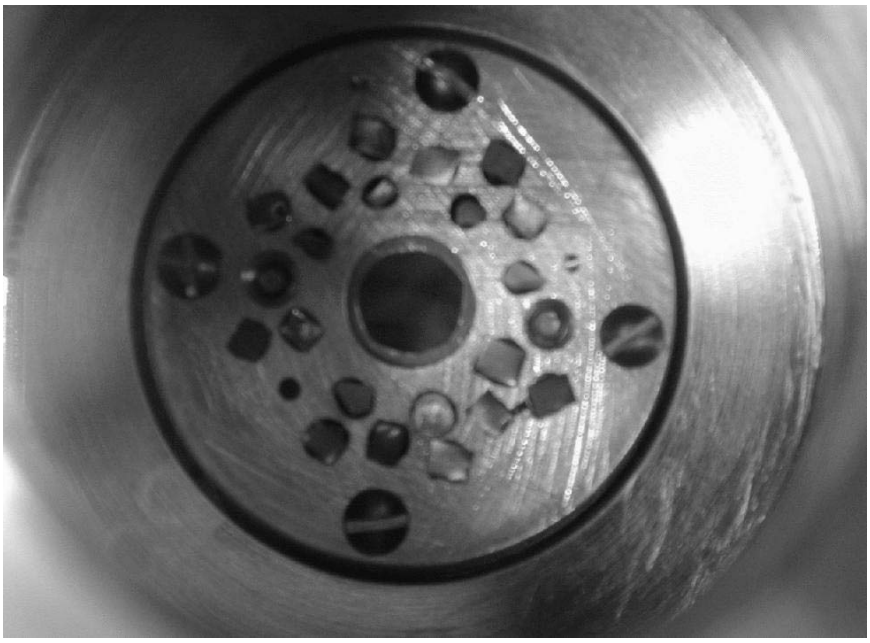

Figure 2.2: Photo of the sample holder used in the second run of the experiment. A total of 20 ablation targets are included in the cell. The cell mirror (and a mis-shapen kapton annulus serving as a buffer between the mirror and sample holder) can be seen at the center of the holder. The ablation targets are the various irregularly-shaped objects, not to be confused with the 4 round screw-heads and 2 screw-ends that are also visible in the photo.

In the second run of the non-S-state atom experiment, we include 20 different ablation targets (see Figure 2.2 for a picture of the sample holder). In addition to the rare-earth atoms discussed in Chapter 5 (Pr, Nd, Tb, Dy, Ho, Er, and Tm), we also have Sc, Ti, V, Cr, Fe, Y, Zr, Mo, La, Gd, Lu, Hf, and CaF_2 (a precursor for the molecule CaF [61]) targets in the cell.

2.1.4 Buffer gas

^{3}He buffer gas is introduced via a 1/16" diameter stainless-steel fill line which is brazed into the top of the cell. The buffer gas is added in steps, where a small

quantity of helium is added, and the resultant buffer gas density measured, until the desired density of $\sim 10^{16}$ cm^{-3} is reached. Once the gas is added, the amount of helium in the cell and fill line is held fixed by closing a room temperature valve. We find that it takes several hours for the gas to equilibrate in the cell; the measured buffer gas density in the cell increases during this time, then reaches a final steady value.

It is desirable that the buffer gas density be determined by the quantity of helium in the cell rather than the cell temperature (i.e. that the density not be vapor pressure limited). Therefore, during these measurements, the cell is maintained at an elevated temperature so that the saturated vapor pressure of helium is greater than the cell pressure.

The density of buffer gas in the cell is found by measuring the rate of diffusion of chromium atoms to the cell walls; see Section 3.3.

2.2 Detection

The atoms are detected via absorption spectroscopy. The optical transition used for each atom and the corresponding level data are listed in Table 2.3. These transitions are chosen for their strength (transition probabilities are all greater than 3×10^7 s^{-1}) and accessibility (all of the wavelengths used are in the visible or near UV, and can be produced with frequency doubled Ti:sapphire laser light). Additional constraints on the transitions chosen are discussed in Section 2.2.4.

A schematic of the optics used in ablation and detection is shown in Figure 2.3. A Coherent Verdi laser [64] which outputs 10 W of light at 532 nm is used to pump a Coherent 899-21 Ti:sapphire ring laser [65]. The Ti:sapphire laser is tunable from 700-1100 nm and outputs ∼1 W of continuous-wave light. The laser is tuned to

Table 2.3: Level information for the optical transitions used in absorption detection. List is arranged by ground-state term, then by atomic number. All data taken from Ref. [39], except [a]Ref. [62] and [b]Ref. [63].

Atom	Ground state		Excited state				λ	A
	Term	g_J	Term	J'	g'_J	Lvl (cm^{-1})	(nm)	(10^8 s^{-1})
Cr	$^7S_3$	2.002	^7P	4	1.7510	23498.84	426	0.315
Sc	$^2D_{3/2}$	0.799	^2F	5/2	0.857	25584.64	391	1.66
Y	$^2D_{3/2}$	0.798[a]	^2F	5/2	0.964[a]	24518.80[a]	408	1.1
Ti	$^3F_2$	0.66	^3D	1	0.50	25317.81	395	0.485
Zr	$^3F_2$	0.66[a]	^3G	3	0.82[a]	25729.96[a]	389	unknown
Tm	$^2F_{7/2}$	1.141	(7/2,1)	5/2	1.06	24418.02	410	0.90
Tb	$^6H_{15/2}$	1.33	(15/2,1)	13/2	1.391	23043.43	434	0.74[b]
Er	$^3H_6$	1.164	^7M	5	1.128	24083.17	415	1.8
Pr	$^4I_{9/2}$	0.731	^4L	7/2	0.865	21105.88	474	0.58[b]
Nd	$^5I_4$	0.603	^5H	3	0.650	21572.61	464	0.83[b]
Dy	$^5I_8$	1.242	^5K	9	1.22	23736.6	421	2.08
Ho	$^4I_{15/2}$	1.195	(15/2,1)	17/2	unknown	24360.81	411	1.6[b]

twice the wavelength of the atomic transition using a Burleigh wavemeter [66] for reference. The light is then frequency doubled with an LBO crystal [67] inside a resonant doubling cavity [68]. For Sc detection, a 390 nm diode laser system [69] may also be used (see Section 2.2.3).

The probe beam then passes through neutral density filter wheel so that the beam intensity entering the cell may be controlled. The beam is focused through a 50 micron pinhole to clean up its spatial profile. The focal lengths of the two lenses on either side of the pinhole are chosen such that the collimated beam leaving the optics table is 1 cm in diameter. The beam is then directed to an optical breadboard mounted on the bottom plate of the dewar. The beam diameter is reduced to 2 mm using an adjustable iris. A beamsplitter then splits the beam into "signal" and "reference" legs. The signal beam passes through a set of cryostat windows and into the cell, where it can be interact with the atom cloud. The beam retro-reflects off of a mirror at the

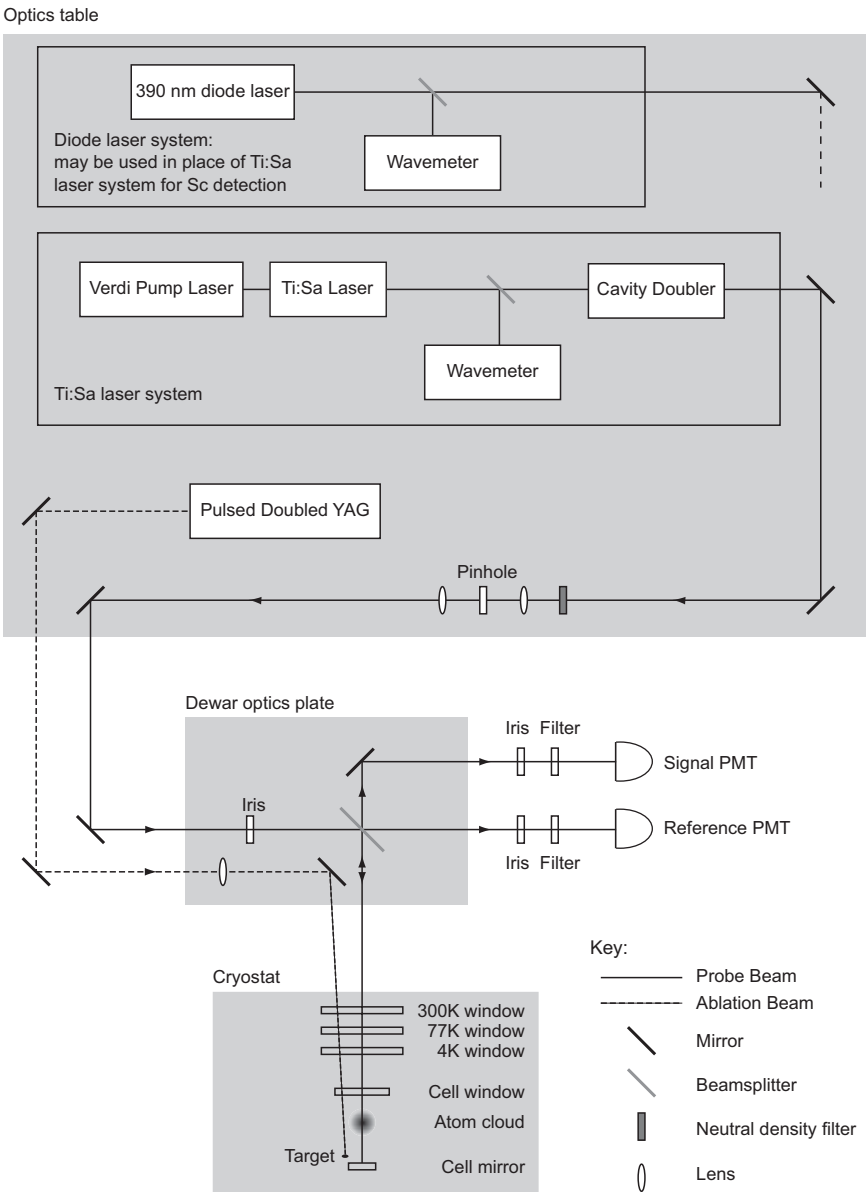

Figure 2.3: Optics setup.

far side of the cell, exits the cryostat, and is redirected to the "signal" PMT. The reference beam passes through the beamsplitter and goes directly to the "reference" PMT. Current outputs from each PMT then go to a SRS current preamp, and the output is fed into a data acquisition system, where the reference and signal voltages are digitized and stored in a data file on a computer. Further manipulation is done

in software (MATLAB is generally used). Intensity fluctuations in the primary laser beam are divided out by taking a ratio of the signal and reference voltages.

A baseline measurement is recorded prior to the ablation pulse. As there is some frequency dependence to the light transmitted by the cell optics, the baseline is measured as a function of laser frequency. The absorption of atoms in the cell is found by dividing the post-ablation signal by the baseline.

2.2.1 Ti:sapphire laser drift correction

The 899-21 Ti:sapphire ring laser is an actively stabilized, single frequency laser with a linewidth of ∼500 kHz. Two etalons in the lasing cavity force single-mode lasing, while the frequency is stabilized by locking to a reference cavity. Over short periods (1 second) the laser frequency is stable to less than a few MHz, however the laser is seen to drift tens of MHz over the course of a few minutes. A typical data set consisting of baseline measurement, ablation, and absorption time profile or spectrum lasts less than a second. However, for measuring the time profiles of the Zeeman level populations, the laser is parked on the absorption peak for a particular level and several data sets are taken in succession and averaged together. This both improves signal-to-noise and also allows us to average out shot-to-shot variations in ablation yields so that the populations of various Zeeman levels may be meaningfully compared. It is necessary to wait a few minutes between sets to allow the mixing chamber to cool from each ablation pulse. For data taken in the Helmholtz field, where the absorption peaks are as narrow as 100 MHz, the long term laser drift is unacceptable.

To combat the drift, we employ part of a laser locking system developed by Robert deCarvalho and described at length in his thesis [70]. Briefly, part of the Ti:sapphire

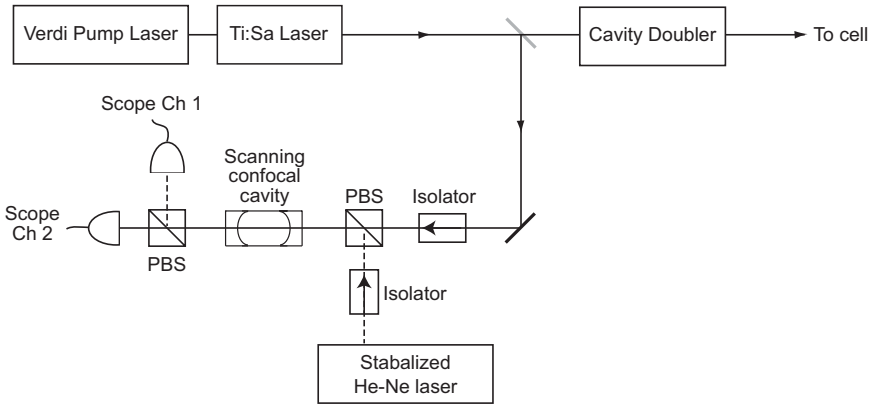

Figure 2.4: Laser drift monitor.

laser output is sent to a high-finesse, scanning confocal cavity along with the output from an ultrastable He-Ne laser (see Figure 2.4). The two lasers are linearly polarized in orthogonal directions so that they may be combined with a polarizing beam splitters (PBS) prior to entering the cavity. The transmitted beams are separated with a second PBS and are detected independently with two photodiodes, whose outputs are sent to a two-channel oscilloscope. The scope is triggered off of the cavity ramp, and the cavity is scanned such that transmission peaks from both lasers are observed. As the stabilized He-Ne laser [71] used has a drift of <2 MHz/hour, any observed relative drift is attributed to the Ti:sapphire laser. The drift is corrected by adjusting an analog voltage which controls the laser frequency.

2.2.2 Ti:sapphire laser scan calibration

The Ti:sapphire laser frequency may be scanned via an analog external input voltage that controls a galvomounted rotating Brewster plate in the reference cavity. As the rotation angle of this plate is scanned, so is the optical path length in the reference cavity, and thus the frequency to which the laser is locked. A linear voltage ramp maps to a linear frequency scan up to 30 GHz in width. The nominal width of the

scan for a ±5 V voltage ramp is chosen using a dial on the laser control box.

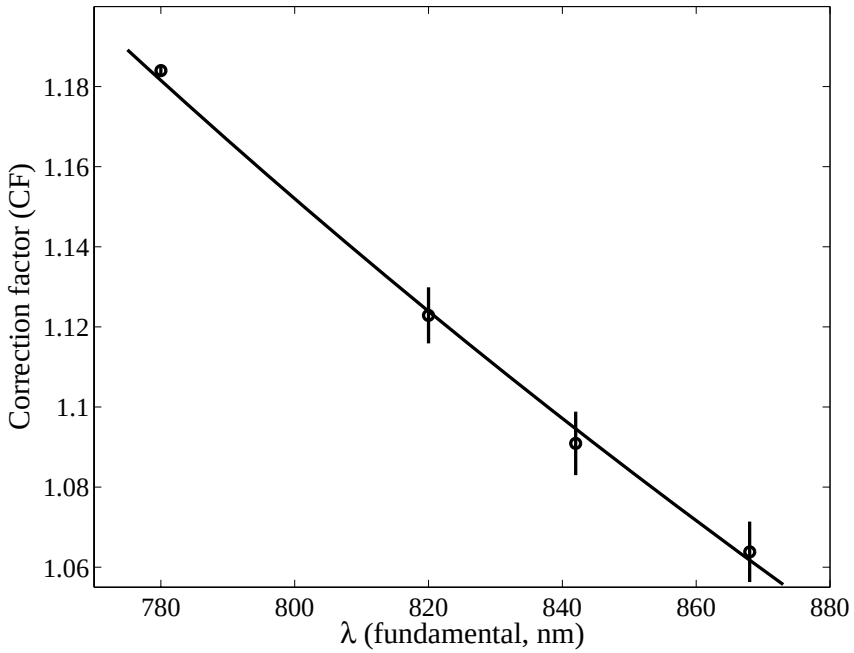

Figure 2.5: Frequency scan correction factor for Ti:sapphire laser as a function of wavelength. The nominal scan width provided by the laser control box must be multiplied by the correction factor to give the actual scan width. The open circles represent the measured correction factor at various wavelengths; the vertical bars represent the statistical error in measuring the transmission peak spacing. For the data point at 782 nm, the error bar is smaller than the open circle marking the data point due to a large number of measurements at this wavelength. The 2% systematic error in the etalon FSR is not included in the error bars. The solid line is a fit to CF= λ_0/λ and gives $\lambda_0 = 922$ nm.

The actual scan width is measured using a ULE etalon [72] with a free spectral range (FSR) of 5±0.1 GHz and linewidth of 10-30 MHz. The frequency-doubled laser output is sent to the etalon, and the transmitted beam is detected with a photodiode. The laser frequency is scanned over a nominal 3 GHz (fundamental) scan width, so that the doubled scan width exceeds the etalon FSR. The laser ramp center frequency is adjusted so that two transmission peaks are observed during each scan. The actual

frequency spacing between the peaks (5 GHz) is compared with the nominal spacing given by the control box. As shown in Figure 2.5, it is found that the nominal value is off by as much as 19%, and that the correction factor that must be applied varies with wavelength. This is expected since an addition to the path length in the cavity, ΔL, will lead to a change in lock wavelength of

$$\Delta\lambda = \frac{2\Delta L}{N}, \tag{2.1}$$

where N is the number of half-wavelengths in the cavity. For $\Delta L \ll L$ this is equivalent to a change in lock frequency of

$$\Delta f = \frac{2c\Delta L}{\lambda L}, \tag{2.2}$$

where c is the speed of light and L is the length of the reference cavity. If the nominal scan width is correct for a particular wavelength, λ_0, a correction factor, CF= λ_0/λ, is needed at all other wavelengths. A one-parameter fit to the measured correction factors shown in Figure 2.5 agrees well with the expected dependence on wavelength. All spectra in this thesis are shown with the appropriate correction factor applied.

2.2.3 Diode laser calibration

Scan width calibration

A grating-tuned diode laser [69] at 391 nm may be used instead of the doubled Ti:sapphire system for Sc detection. The diode laser system has the advantage that it may be frequency scanned at a high rate (up to 500 Hz), allowing spectra to be taken with fast time resolution. This is important for getting a time profile of the cloud temperature at early times following ablation pulse.

The diode laser uses a Littrow set-up, where the first order Bragg light from the grating is reflected directly back into the diode. The grating forms one end of a linear

laser cavity, while the back face of the diode forms the other. The laser wavelength is scanned by rotating the grating about the axis formed by the intersection of the grating plane and laser-diode back-face plane. Rotating the grating has the effect of changing the Bragg condition, and of changing the cavity length. The grating is coarsely rotated using a thumbscrew, while fine scanning is accomplished by applying a voltage to a piezo-electric actuator. The coarse adjustment causes the grating profile to shift enough that a new cavity mode is chosen, allowing a large change in laser wavelength. The fine scanning relies on the change in cavity length as the grating mount is rotated to shift the current cavity mode.

The frequency scan width for a given applied sinusoidal voltage ramp is calibrated by comparing spectra taken with the diode with those taken with the Ti:sapphire laser. This is readily done using the multiple hyperfine peaks in the Sc spectrum (see Section 3.4.1). We measure the spacing of a pair of peaks from a calibrated Ti:sapphire laser spectrum, and then use this spacing as a ruler to set the frequency scale of the diode spectra.

Phase correction

The voltage applied to the piezo is recorded along with the PMT signals. This voltage ramp is converted to a frequency ramp by assuming the frequency shift is proportional to the applied voltage, and using the scaling factor discussed in the previous section. We find, however, that for fast ramp rates the laser frequency ramp lags in phase behind the applied voltage ramp. We must correct for this lab before converting the applied voltage to laser frequency.

Figure 2.6 shows both the applied laser voltage and the laser intensity measured by the reference PMT for a 500 Hz ramp rate. The laser intensity is expected to change as

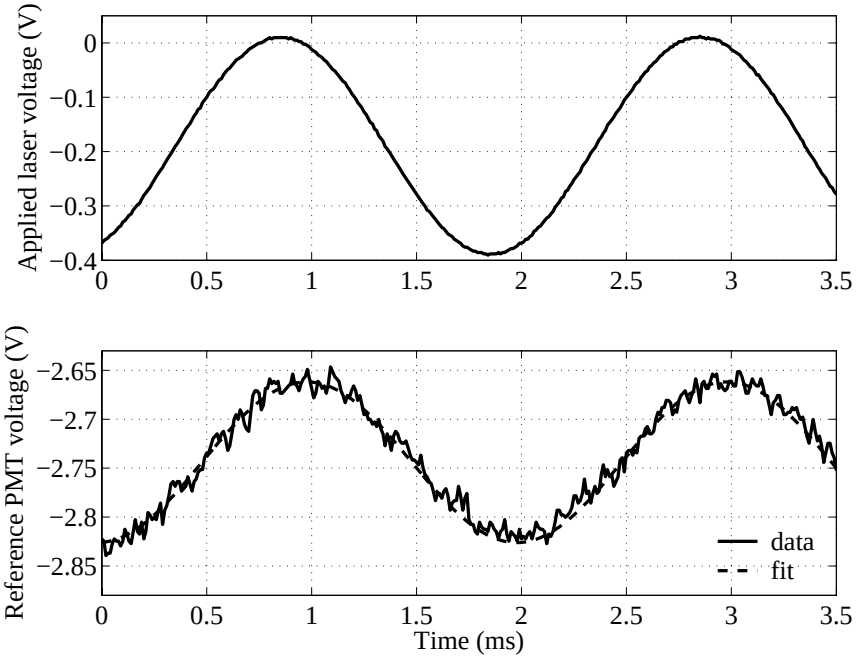

Figure 2.6: Diode frequency scan phase lag. The upper plot shows the applied voltage as a function of time for a 500 Hz ramp rate. The lower plot shows the laser intensity as measured by the reference PMT. The sinusoid fit is shown on the lower plot, but is omitted from the upper plot. There is so little noise on the applied laser voltage that the fit and measured curve completely overlap. The laser intensity lags the applied voltage by 22 degrees here.

the grating is scanned since the external cavity mode that selects the laser frequency shifts with respect to the internal diode mode[1] and grating profiles. Comparing the two plots, we see that the laser intensity lags the applied voltage ramp. The phase shift is found by fitting both curves with a sine function. The recorded applied laser voltage array is then shifted in time so that it is in phase with the laser intensity.

[1]The internal diode modes are created by the cavity formed by the two the diode faces.

2.2.4 Zeeman broadening with anti-Helmholtz magnet

The inelastic collision rate for collisions of TM atoms with helium is found by monitoring the individual TM Zeeman level populations over time with the magnetic field on. In order to monitor the population of a specific Zeeman level, it is necessary to spectroscopically isolate it. This is most readily done by applying a homogeneous magnetic field which splits the absorption lines from neighboring levels by an amount greater than the Doppler linewidth. The frequency shift for a particular $\Delta m = -1, 0$ or $+1$ transition from Zeeman level m is given by

$$\Delta f = (g'_J(m + \Delta m) - g_J m)\mu_{\rm B} B/h, \tag{2.3}$$

where B is the magnetic field strength, and h is Planck's constant. The frequency splitting between two neighboring Zeeman levels, m and $m-1$, is then

$$\begin{aligned} \Delta f_{m,m-1} &= [g'_J(m + \Delta m) - g_J m - (g'_J(m - 1 + \Delta m) - g_J(m-1))]\mu_{\rm B} B/h \\ &= (g'_J - g_J)\mu_{\rm B} B/h. \end{aligned} \tag{2.4}$$

For the transition metals studied, this splitting is $\sim$2 GHz/Tesla. Considering that fields greater than a Tesla are easily achieved, the lines are easily resolved with a homogeneous field. A fairly homogeneous field may be created with coils run in the Helmholtz configuration. However, as discussed in Section 2.1.2, for the first run of the experiment the applied field could only be run anti-Helmholtz, and the resulting spherical quadrupole field is decidedly inhomogeneous. The field profiles for both Helmholtz and anti-Helmholtz configuration are shown in Figure 2.7.

In the spherical quadrupole field, each transition line is broadened from the field-free transition frequency out to a maximum shift for atoms sitting at the trap saddle points. Adding to this the fact that there may be multiple transitions ($\Delta m = -1, 0, +1$) possible, it looks like the absorption signals from the various Zeeman levels

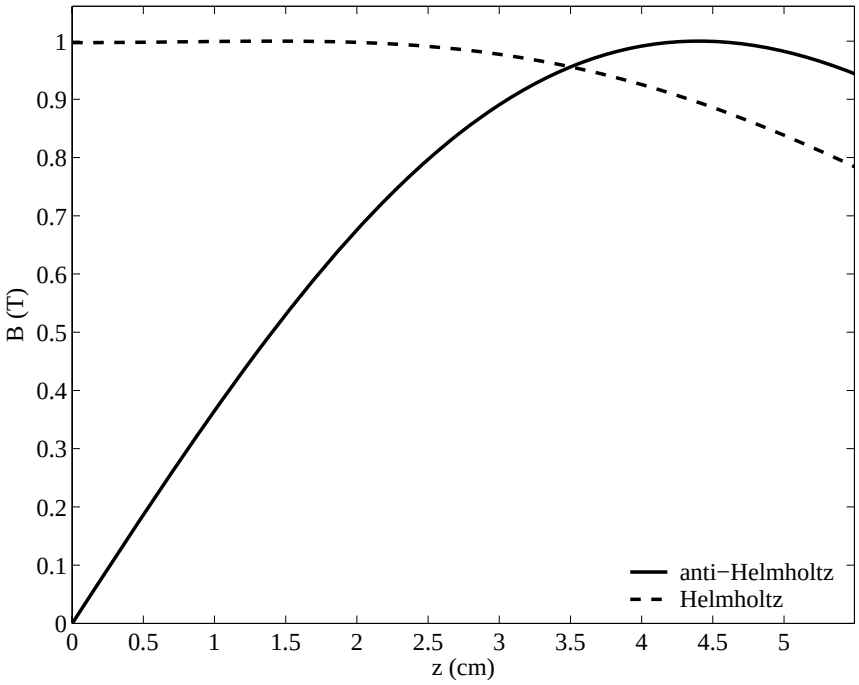

Figure 2.7: Magnetic field profiles along the probe beam (r=0) for Helmholtz and anti-Helmholtz current geometries. For convenience, the maximum field along the beam is made to equal $B = 1$ T in both cases. This corresponds to a 16 A coil current anti-Helmholtz, and 9 A coil current Helmholtz. The origin, $z = 0$, is the midpoint between the two coils. The field magnitude is symmetric about this point.

will be hopelessly muddled. As it turns out, however, it is generally possible to isolate atoms in the $m = \pm J$ levels as long the absorption transition is chosen so that the ground and excited levels satisfy one of the following sets of criteria:

$$J' = J + 1, \quad g_J < g'_J \tag{2.5a}$$

$$J' = J - 1, \quad g_J > g'_J \tag{2.5b}$$

$$J' = J, \quad g_J > g'_J \tag{2.5c}$$

In case a, the $m = +J$ and $m = -J$ levels are detected on the $\Delta m = +1$ and $\Delta m = -1$ transitions, respectively. For a particular field, B, these two transitions

will have the largest frequency shifts of all available transitions. The former will be shifted farthest blue, while the latter will be shifted farthest red. In case b, the $m = +J$ level is detected on the $\Delta m = -1$ transition, while the $m = -J$ transition is detected on the $\Delta m = +1$ transition. In case c, they are each detected on a $\Delta m = 0$ transition. In all cases, these lines will be shifted farther than any other available transition and will lie on opposite sides of the field free transition frequency. Of course, these shifts increase with increasing magnetic field. The farthest ends of a spectrum taken of atoms in the spherical quadrupole field will correspond to $m = \pm J$ atoms at the trap saddle points (this is the maximum field along the probe beam). The situation is made even better by the field being flat here— there is a large volume of atoms to interact with and thus an increase in signal. Note that all the transition-metal transitions used (see Table 2.3) satisfy criteria a or b. Transitions described by c are not used since it is generally not desirable to detect on a $\Delta m = 0$ transition. Due to the cylindrical symmetry of the coils, it is evident that along the axis of the cell, the local magnetic field must be pointed in $\pm\mathbf{z}$ direction. Since probe beam runs along the cell axis, the local magnetic field is generally parallel or anti-parallel to the probe beam. According to electric dipole selection rules [73], only $\Delta m = \pm 1$ transitions are allowed for the atoms probed.[2]

[2]Due to the finite beam size and errors in centering the beam, there will be some atoms for which some component of the field lies perpendicular to the beam, especially near the horizontal mid-plane of the cell. Along the mid-plane, the field increases in magnitude as r increases, and the field points in the radial direction. The atoms here will undergo $\Delta m = 0$ transitions, however, this is a small volume of atoms. Furthermore, these atoms do not sit at the field maximum so they will not be spectroscopically isolated.

2.2.5 Polarization issues with Helmholtz magnet

As discussed in the last section, detection with the anti-Helmholtz magnet is always performed on a $\Delta m = \pm 1$ transition due to electric dipole selection rules prohibiting most of the atoms lying on the beam from absorbing $\Delta m = 0$ light. In the second run, we exploit the fairly uniform field provided by the Helmholtz magnet when measuring time profiles of the high and low-field-seeking Zeeman levels. The field is again aligned parallel or anti-parallel to the probe beam, however in this case there is no symmetry about the cell mid-plane. Instead, the field is aligned in one direction along the length of the cell. This asymmetry can pose a problem when comparing absorption of high- and low-field-seeking atoms due to their being detected on opposing $\Delta m = \pm 1$ transitions.

To explain this further, consider Nd as an example. Nd is detected on the ${}^5I_4 \rightarrow {}^5H_3$ line. The low-field-seeking $m = 4$ state is detected on a $\Delta m = -1$ transition to the $m' = 3$ excited state level, whereas the high-field-seeking $m = -4$ state is detected on a $\Delta m = +1$ transition to the $m' = -3$ excited state level. Assume the current flow direction is chosen to be counter-clockwise, so that the magnetic field in the cell points in the $+\mathbf{z}$ direction. If the probe light is right circularly polarized (RCP),[3] it will interact with the high-field-seeking atoms, but not the low-field seekers. The opposite is true if the probe light is left circularly polarized (LCP). To make meaningful comparisons in the absorption of high- and low-field-seeking atoms, it would be necessary to ensure a high degree of control of the light polarization entering the cell. This is difficult to achieve due to the many cryostat windows the probe beam traverses. We instead take two sets of absorption measurements— one with the

[3]We define the light polarization with respect to the lab $+z$ axis. Note that when the probe beam retro-reflects off of the cell top mirror, it retains its polarization.

magnet current running clockwise, the other counter-clockwise— and average them. All absorption time profiles in this thesis taken with the Helmholtz geometry are a result of such an average. We use probe light that is roughly linearly polarized; any systematic difference in high- and low-field-seeking atom absorption due to differing amounts of RCP and LCP light should average out.

2.2.6 Effect of trapped fluxes on zero-field temperature measurements

The translational temperature of the gas following the ablation pulse may be found by fitting Voigt profiles to measured zero-field spectra. When making these measurements, the magnet leads are disconnected from the magnet power supply to ensure that no current is flowing through the coils. Nonetheless, the coils continue to produce a magnetic field due to trapped fluxes in the superconducting wire. The residual field was measured previously and was found to be ∼10 Gauss [56]. Nominal "zero-field" temperature measurements may be affected by this residual field due to Zeeman level shifts. Here we investigate the effect of Zeeman broadening on the spectra of Ti and Sc, which are used for determining translational temperatures in Sections 3.4.2 and 3.5.4.

Ti is detected on the $^3F_2 \rightarrow {}^3D_1$ transition at 395 nm. The $J = 2$ ground state consists of 5 Zeeman levels ($m_J = -2, \ldots, 2$), while the $J' = 1$ excited state is split into 3 levels ($m'_J = -1, 0, 1$). For zero magnetic field, the Zeeman levels for each electronic state are degenerate, producing a single $J \rightarrow J'$ absorption line. The degeneracy is lifted in a magnetic field and each transition line is shifted by the amount given in Eq. (2.3).

We estimate the effect of the residual field on the Ti absorption spectrum by sim-

ulating a Voigt profile for each $|Jm_J\rangle \rightarrow |J'm'_J\rangle$ transition at the shifted transition frequency and summing over all the allowed transitions. Each transition is weighted by the square of the Clebsch-Gordon coefficient linking the ground and excited Zeeman levels, $|\langle J, m_J; 1, \Delta m_J \,|J', m'_J\rangle|^2$, where Δm may be $0, \pm 1$ (the possible values for the photon angular momentum). Figure 2.8 shows the simulated spectrum for 500 mK Ti atoms in a 10 Gauss field. The individual line positions and their relative weights are indicated by the vertical lines. The true zero-field spectrum is shown by the dashed line. The residual field broadens the spectrum so that the apparent[4] temperature of the gas is now 570 mK. The fractional effect of the residual field decreases with increasing temperature. For the Ti translational temperatures measured in this thesis, the broadening from the residual field is small compared to the statistical fit errors and error due to the uncertainty in the calibration for the frequency scale of the spectrum.

We follow a similar treatment for Sc spectra, however in this case the electronic states are split into multiple hyperfine lines since Sc has nuclear spin ($I = 5/2$). Sc is detected on the ${}^2D_{3/2} \rightarrow {}^2F_{5/2}$ transition at 391 nm. For the translational temperature measurements described in Section 3.4.2, we scan over two hyperfine peaks: $F = 4 \rightarrow F' = 3$ and $F = 5 \rightarrow F' = 5$. Each F level consists of $2F + 1$ Zeeman sublevels, $m = -F, \ldots, F$, which are degenerate at zero field. In a small magnetic field the sublevels are shifted by an amount

$$\Delta f = m g_F \mu_B B, \tag{2.6}$$

where the g factor g_F is

[4]For the "apparent" temperature, we fit a single Voigt profile to the composite absorption spectrum.

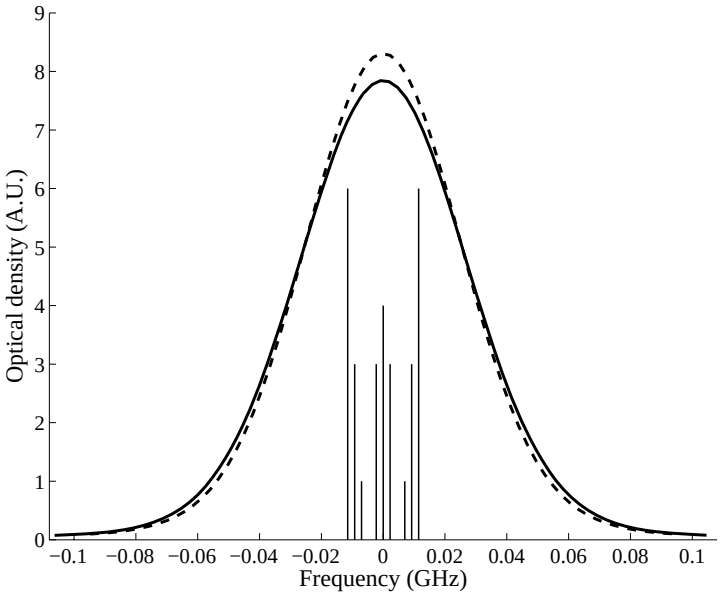

Figure 2.8: Simulated Ti spectra for $B = 0$ (dashed curve) and $B = 10$ Gauss (solid curve). The vertical lines indicate the individual $|Jm_J\rangle \rightarrow |J'm'_J\rangle$ line positions and relative intensities for the 10 Gauss spectrum.

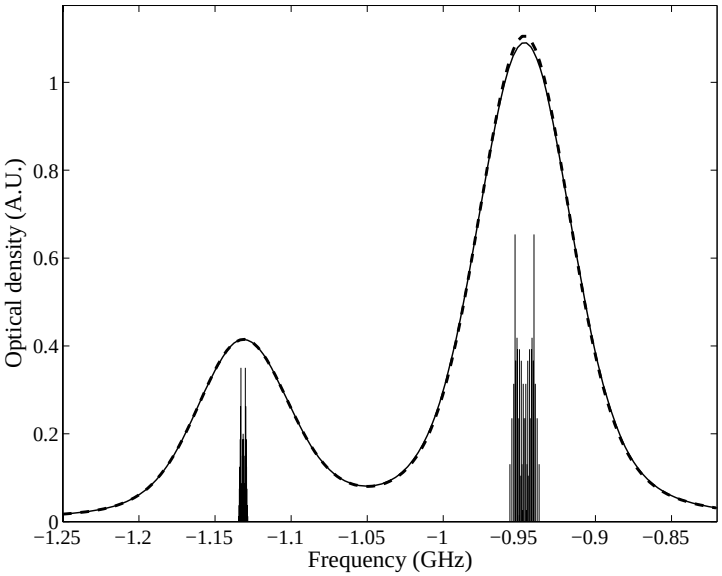

Figure 2.9: Simulated Sc spectra for $B = 0$ (dashed curve) and $B = 10$ Gauss (solid curve). The vertical lines indicate the individual $|Fm\rangle \rightarrow |F'm'\rangle$ line positions and relative intensities for the 10 Gauss spectrum.

$$g_F = g_J \frac{F(F+1) + J(J+1) - I(I+1)}{2F(F+1)}. \tag{2.7}$$

The simulated spectrum for 500 mK Sc atoms in a 10 Gauss field is shown in Figure 2.9. The true zero-field spectrum is also shown, and we see that the two spectra are nearly identical. The residual field has a negligible effect on the spectrum.

According to these estimates, the residual field in the cell from trapped fluxes has a small effect on the nominal zero-field spectra for Sc and Ti. However, this will not generally be the case. As an example, we show in Figure 2.10 the simulated absorption spectrum for 500 mK Dy ($I = 0$) atoms in a 10 Gauss field, along with the field-free spectrum, for the ${}^5I_8 \rightarrow {}^5K_9$ transition at 421 nm.[5] The 10 Gauss field has a large effect, elevating the apparent temperature to 1.2 K.

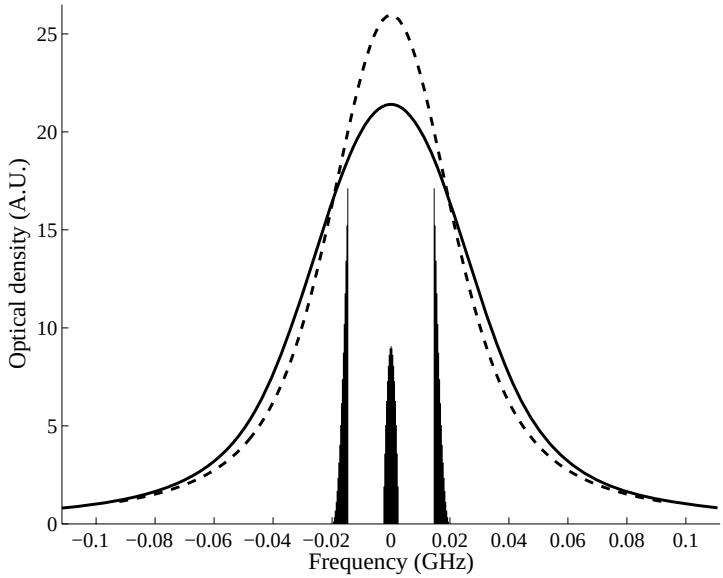

Figure 2.10: Simulated Dy spectra for $B = 0$ (dashed curve) and $B = 10$ Gauss (solid curve). The vertical lines indicate the individual $|Jm_J\rangle \rightarrow |J'm'_J\rangle$ line positions and relative intensities for the 10 Gauss spectrum. The lines are bunched into three groups corresponding to $\Delta m_J = -1, 0, 1$.

[5]Dy is not used to measure the translational temperature in the rare-earth experiments. This spectrum is merely shown for contrast.

Chapter 3

Transition metal results

In this chapter, we present the results from our experiment investigating the suppression of inelastic collisions in non-S-state atoms. We studied transition-metal (TM) atoms Sc, Ti, Y and Zr (Table 3.1) using the methods outlined in the previous chapter for measuring the elastic and inelastic TM-^{3}He collision rates.

Most of the data in this chapter are taken from the first run of the experiment, where we were constrained to running the magnet in the anti-Helmholtz configuration. While anti-Helmholtz is a trapping configuration, trapping was not our primary goal in this run. Even with favorable inelastic collision rates, trapping these atoms would be difficult in our cell due to their small magnetic moments (each has a magnetic moment less than $2\mu_{\mathrm{B}}$). In order to efficiently trap such atoms, a faster buffer-gas pump-out is required than can be achieved with this cell [74].

3.1 Elastic collision rate measurement

We determine the elastic cross section σ_{el} for TM-He collisions by monitoring the diffusion of the TM atoms through the helium buffer gas at zero magnetic field. As

Table 3.1: Transition-metal atoms studied, with ground-state term and magnetic moment (in units of μ_B).

Atom	Term	μ/μ_B
Sc	$^2D_{3/2}$	1.20
Y	$^2D_{3/2}$	1.20
Ti	$^3F_2$	1.32
Zr	$^3F_2$	1.32

derived in Ref. [75], the exponential lifetime for the diffusion of atoms through a much denser buffer gas in a cylindrical chamber of radius r and height h is given by

$$\tau = 2.1 n \sigma_d \sqrt{kT/\mu} \left((2.4/r)^2 + (\pi/h)^2 \right)^{-1}, \tag{3.1}$$

where n is the buffer gas density, σ_d is the diffusion cross section, and μ is the reduced mass. For our cell, $r = 3.2$ cm and $h = 11$ cm. The diffusion cross section is a measure of the forward momentum loss of the atoms as they diffuse through the buffer-gas and is given by

$$\sigma_d = \int \frac{d\sigma}{d\Omega}(1 - \cos\theta) \sin\theta d\theta d\phi, \tag{3.2}$$

where $d\sigma/d\Omega$ is the differential elastic scattering cross section and θ and ϕ are the polar and azimuthal scattering angles in the center-of-mass frame. For identical particles, the amplitudes for forward and backward scattering are equal so that $\sigma_d = \sigma_{el}$. For distinguishable particles, the diffusion and elastic cross sections differ in general, with the elastic cross section being somewhat larger than the diffusion cross section outside of scattering resonances. For Ti-He and Sc-He scattering, $\sigma_{el} \approx 2.5\sigma_d$ [76]. In this thesis, however, we take $\sigma_{el} = \sigma_d$ since the numerical factors relating the elastic and diffusion cross-sections are not known for all of the species studied.

3.2 Inelastic collision rate measurement

The inelastic collision rate for collisions of TM atoms with helium is found by monitoring the individual TM Zeeman level populations over time with the magnetic field on. Immediately following the ablation, all Zeeman levels are equally populated due to the high initial temperature of the gas as a result of the heat deposited by the ablation pulse. As the atoms thermalize with the cold buffer gas their kinetic energy becomes comparable to the splitting between Zeeman levels, and atoms in low-field seeking levels relax to lower-energy Zeeman states through inelastic collisions. We define the Zeeman temperature, T_{Z}, at a particular field B by equating the ratio of the local populations of two Zeeman levels, $|m\rangle$ and $|m'\rangle$, to the Boltzmann factor at a temperature T_{Z}:

$$\frac{N_{|m\rangle}}{N_{|m'\rangle}} = \exp\left(-\frac{g_J \mu_{\mathrm{B}}(m-m')B}{kT_{\mathrm{Z}}}\right), \tag{3.3}$$

where μ_{B} is the Bohr magneton and k is the Boltzmann constant. Atoms in low-field-seeking states relax to lower-energy states until the Zeeman temperature comes down to the translational temperature of the gas. If the Zeeman relaxation rate is longer than the translational thermalization rate, we may determine the cross section for inelastic collisions by measuring the rate at which T_{Z} relaxes to the translational temperature of the gas.

To model the time evolution of the level populations, we must consider that atoms may move back and forth between levels. For simplicity, we assume that the atoms have the same probability to be transferred to any level that is energetically allowed in the collision, and that the inelastic collision rate coefficient is $\Gamma_{\mathrm{in}}/(2J)$ for such a transition. We choose the denominator, $2J$, so that the total inelastic rate constant for the $m = J$ state is Γ_{in} (there are $2J$ Zeeman levels of lower energy than the

$m = J$ level). We thus assume that an atom in an arbitrary Zeeman level $|m\rangle$ is free to move to a lower energy state during an inelastic collision, however promotion to a higher lying Zeeman level $|m'\rangle$ with $m' > m$ will be suppressed by a factor $\exp\left(-g_J\mu_B(m'-m)B/kT_{\rm trans}\right)$, where $T_{\rm trans}$ is the translational temperature of the gas. The rate of change of the density of atoms in state $|m\rangle$ sitting in local field strength B is then

$$\begin{aligned}\dot{n}_m &= -\frac{\Gamma_{\rm in} n_{\rm He} n_m}{2J}\left[\sum_{m'>m} 1 + \sum_{m'>m}\exp\left(-\frac{g_J\mu_B(m'-m)B}{kT_{\rm trans}}\right)\right] \\ &\quad + \frac{\Gamma_{\rm in} n_{\rm He}}{2J}\left[\sum_{m'>m} n_{m'} + \sum_{m'<m}\left(n_{m'}\exp\left(-\frac{g_J\mu_B(m-m')B}{kT_{\rm trans}}\right)\right)\right]. \quad (3.4)\end{aligned}$$

We numerically integrate these coupled differential equations to fit the observed time evolution of the level populations for the inelastic rate coefficient $\Gamma_{\rm in}$. The buffer gas density, $n_{\rm He}$, is measured independently as described in Section 3.3. The translational temperature, $T_{\rm trans}$, may be fit simultaneously with $\Gamma_{\rm in}$; however it may also be measured independently by fitting a Voigt profile to spectra taken at zero magnetic field. The above model does not account for drift due to inhomogeneous fields or diffusion through the buffer gas, so it is only appropriate when the Zeeman relaxation time is much shorter than the drift-assisted diffusion time (we find that this is appropriate for the TM atoms studied). If the Zeeman relaxation time is much longer than the drift-assisted diffusion time, the equilibration of the Zeeman and translational temperatures will not be observed. Instead, trapping should be possible (assuming a sufficient trap depth). In this case, the inelastic rate can be measured by observing the loss rate of trapped atoms. This type of evolution is modeled in Section 5.5 for the rare earths.

Note that it is not necessary to experimentally track all Zeeman levels. We generally track only two, the $m = \pm J$ levels. Since the $m = J$ population is most affected

by inelastic collisions, it provides the best measure of $\Gamma_{\rm in}$. Since the $m = -J$ population is least affected by the inelastic collisions, its time profile provides a measure of the drift timescale. [1]

If we are able to observe the level populations over a period of time where $T_{\rm Z} >> T_{\rm trans}$, then the modeling becomes much simpler. We may then extract the inelastic rate constant simply from the exponential decay of the low-field-seeking, $m_J = J$, state, whose density rate of change reduces to $\dot{n} = -\Gamma_{\rm in}\, n_{\rm He}\, n$, giving $\Gamma_{\rm in} = 1/(\tau_{\rm in} n_{\rm He})$, where $\tau_{\rm in}$ is the measured exponential-decay time constant.

3.3 Buffer-gas density measurement

The helium buffer-gas density is found by measuring the rate of diffusion of Cr atoms at zero field and applying Eq. (3.1). Cr atoms are used since the elastic collision cross-section for Cr-^{3}He collisions is already known, $\sigma_{\rm el} = (1.1 \pm 0.4) \times 10^{-14}$ cm^2 [56]. A fit to the observed exponential decay gives a diffusion time constant of 113 ± 5 ms (Fig. 3.1). The buffer-gas temperature is measured by fitting a Voigt profile to Sc spectra taken using the same ablation and heating powers (see Section 3.4.2). We assume that the Cr temperature profile is similar to that of Sc since the same ablation energies are used, and the elastic cross-sections for Sc-^{3}He and Cr-^{3}He collisions are similar. Over the time period that the Cr diffusion is measured, the observed gas temperature is (0.8 ± 0.2) K. Using Eq. (3.1), we find that the buffer-gas density is $(1.6 \pm 0.6) \times 10^{16}$ cm^{-3}. Most of the error in the density is due to the uncertainty in the Cr-^{3}He elastic-collision cross section.

Constant heating is applied to the cell so that the cell temperature is 350 mK

[1] While atoms in different Zeeman levels will experience different potential surfaces, simulations show that for the TM atoms studied, the drift times will be similar [77].

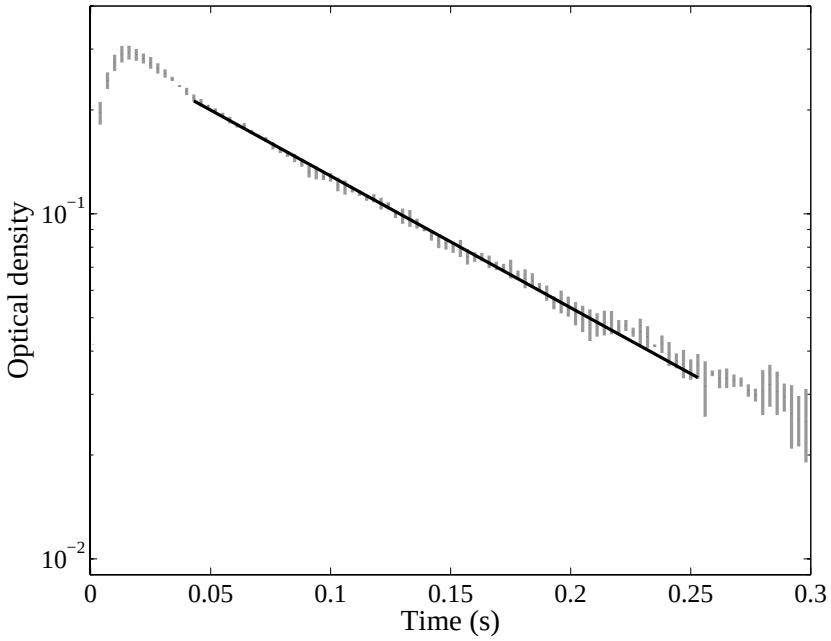

Figure 3.1: Buffer-gas density measurement. The observed peak optical density (proportional to number) of Cr atoms in the cell as a function of time following a 7 mJ ablation pulse at $t = 0$. The gray vertical bars and points are the mean and standard deviation obtained by time binning the combined data from 4 measured diffusion profiles. The diffusion time constant is independent of ablation yield, so we "normalize" the four individual profiles so their optical densities are equal at a particular time (0.05 s) before averaging and finding the standard deviation. This prevents the variation in ablation yield from contributing to the error in the diffusion time constant. The black line is a fit to exponential decay and gives a diffusion time constant of 113 ± 5 ms.

prior to the ablation pulse. This ensures that the buffer gas density is not limited by the saturated vapor pressure of ^{3}He.

3.4 Scandium

Here we present our measurements on scandium. We find that Zeeman thermalization due to collisions with the buffer gas proceeds so rapidly that we are only able to put a lower limit on the inelastic Sc-^{3}He cross-section.

In addition to measurements of the elastic and inelastic collision cross-sections, we also report on our measurements of the previously unknown hyperfine A and B constants for the excited $^2F_{5/2}$ state used in the absorption detection.

3.4.1 Hyperfine structure

Scandium has one naturally occurring isotope, ^{45}Sc, which has nuclear spin $I = 7/2$. The hyperfine constants for the ground state ($^2D_{3/2}$) are $A = 269.558$ MHz and $B = -26.360$ MHz [78]. At zero-field, the hyperfine interaction splits the ground state into four levels, with $F = 2, \ldots, 5$. The hyperfine constants for the excited state (see Table 2.3) were previously unknown; however, we are able to measure them from our zero-field spectra. The excited state is split into six levels, with $F' = 1, \ldots, 6$. Since electric dipole transitions obey the selection rules

$$\Delta F = 0, \pm 1; \quad F + F' \geq 1, \tag{3.5}$$

this results in a total of 12 absorption lines, of which we are able to resolve 11.

Fig. 3.2 shows a Sc spectrum taken with the magnet ramped to zero current which clearly shows multiple hyperfine peaks. We use the formulas for the hyperfine level shifts and relative line intensities from Appendix A to fit this spectrum for the excited state A' and B' hyperfine constants. We find $A' = (170 \pm 2)$ MHz and $B' = (-40 \pm 50)$ MHz.

3.4.2 Translational temperature

We measure the translational temperature of the gas by fitting a Voigt profile to the two Sc hyperfine peaks indicated in Fig. 3.2. We use the diode laser for these measurements since its fast-scanning allows us to take spectra with millisecond time

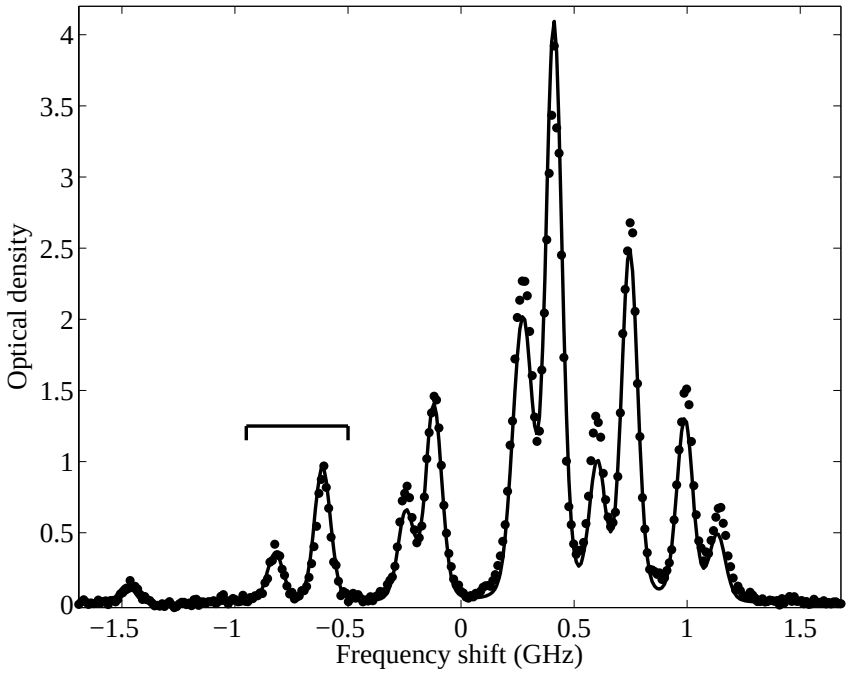

Figure 3.2: Sc zero-field spectrum for the $^2D_{3/2} \rightarrow {}^2F_{5/2}$ transition at 391 nm. The fit to the spectrum shown by the solid line gives values for the excited state hyperfine constants, $A' = (170 \pm 2)$ MHz and $B' = (-40 \pm 50)$ MHz. The two peaks indicated are used for measuring the translational temperature of the gas as described in Section 3.4.2.

resolution. Scanning over two peaks allows us to calibrate the frequency axis of each scan (see Section 2.2.3).

Fig. 3.3 shows an example of such a fit for two successive diode scans taken in the first milliseconds after the ablation pulse. We see that the Sc atoms have cooled somewhat between the two scans, however we expect the thermalization with the buffer-gas to occur much faster, within the first couple of milliseconds. The decrease in temperature seen is due to the cooling of the buffer-gas itself; the buffer gas absorbs heat from the ablation pulse and re-equilibrates with the cell walls over several milliseconds.

Fig. 3.4 shows the time profiles gathered from fitting successive spectra for two different ablation pulse energies. The cooling of the buffer-gas over the first few

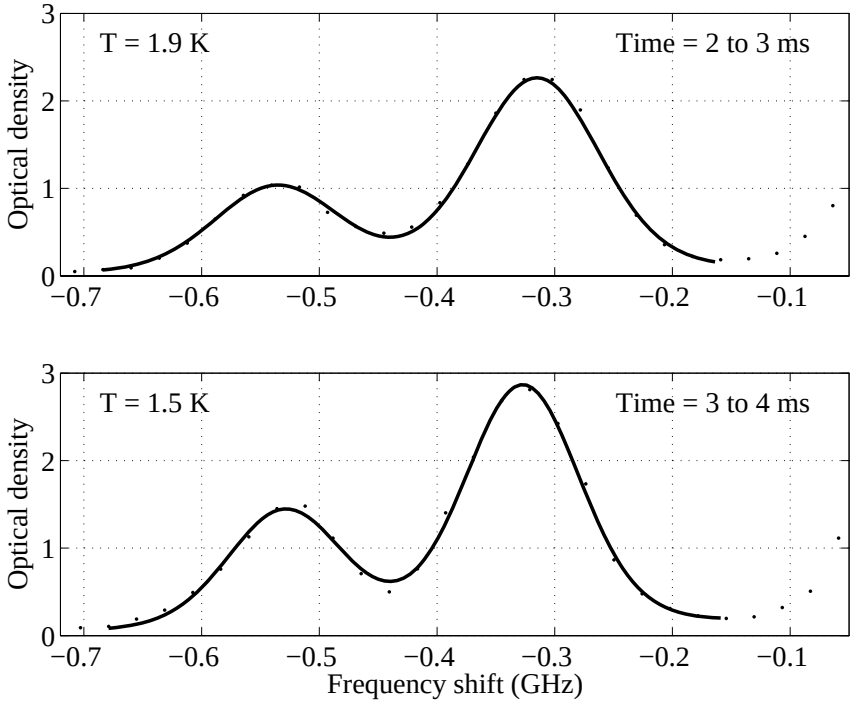

Figure 3.3: Voigt profile fits to two successive Sc spectra taken in the first few milliseconds after the ablation pulse.

milliseconds is evident. There is also a slow decrease in temperature which is due to the cell cooling, which occurs over several seconds. Note that we are not able to take any measurements in the first 2 ms after the ablation pulse. During this time, light from the ablation pulse overwhelms the probe signal in the PMTs.

3.4.3 Elastic collisions with He

We measure the Sc-^{3}He elastic-collision cross-section by observing the zero-field diffusion of Sc atoms through the buffer gas, and applying Eq. (3.1). Fig. 3.5 shows a one-body fit to the measured Sc number time profile, giving a diffusion time of 140 ± 10 ms. We find a Sc-^{3}He elastic cross-section of $(1.3 \pm 0.6) \times 10^{-14}$ cm^2 at a temperature of 0.8 ± 0.2 K.

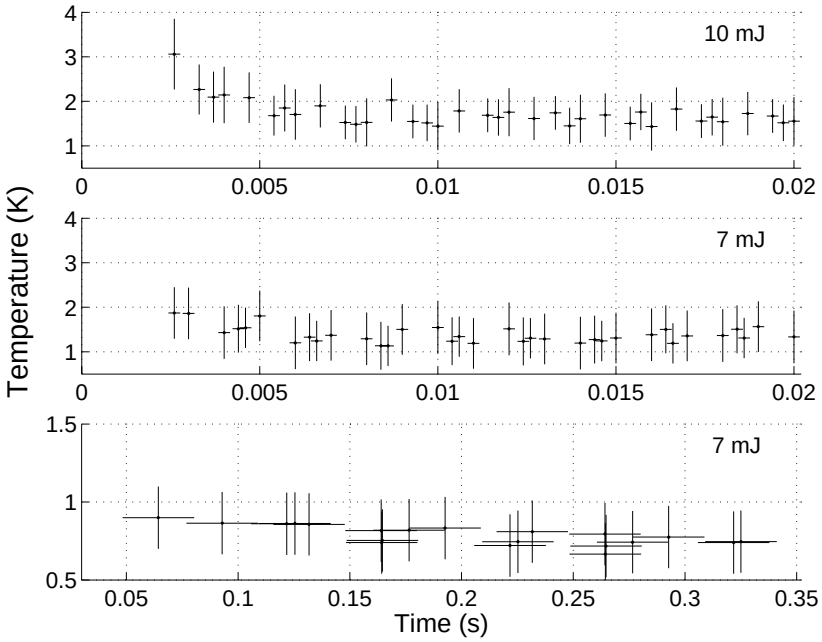

Figure 3.4: Sc translational temperature for two different ablation pulse energies. The statistical error in the Voigt fits and the systematic error from the laser frequency calibration are included in the error bars. The bottom panel shows the Sc temperature over an extended time period for an ablation pulse power of 7 mJ and shows the slow decrease in temperature due to the cell cooling.

3.4.4 Sc spectra in the anti-Helmholtz field

For the inelastic collision rate measurement, we ablate the Sc atoms into the buffer gas with the magnet ramped to a current of 60 A. This gives a field at the saddles of 3.8 T, which splits adjacent ground state Zeeman levels by 2.5 K, and the $m_J = \pm 3/2$ levels by 7.4 K. At a gas temperature of 1 K, this leads to a suppression of the $m_J = +3/2$ population by a factor of $e^{-7.4} = 6000$ compared to the population in the $m_J = -3/2$ level when the Zeeman temperature has equilibrated with the translational temperature of the gas.

Immediately following the ablation, all Zeeman levels for the electronic ground state are equally populated (the energy involved in the ablation is much greater than

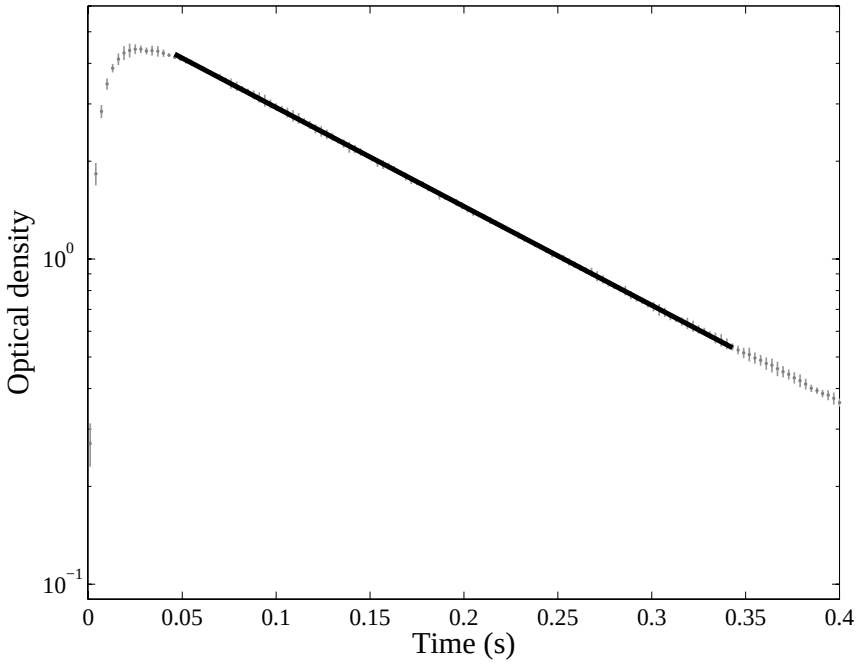

Figure 3.5: The observed peak optical density (proportional to number) of Sc atoms in the cell as a function of time following a 7 mJ ablation pulse at time $t = 0$. The gray vertical bars and points are the mean and standard deviation obtained by time binning the combined data from five measured diffusion profiles. The diffusion time constant is independent of ablation yield, so we "normalize" the five individual profiles so their optical densities are equal at a particular time (0.05 s) before averaging and finding the standard deviation. This prevents the variation in ablation yield from contributing to the error in the diffusion time constant. The black line is a fit to exponential decay and gives a diffusion time constant of 140 ± 10 ms.

the energy splittings between Zeeman levels). If the inelastic collision rate were very small, these atoms would diffuse throughout the cell without their Zeeman states changing, and we would observe a spectrum similar to Fig. 3.6a. The peaks at large absolute frequency shift are from the absorption of atoms at the field saddle regions, where the field is flat. The lower panel of Fig. 3.6a breaks up the simulated spectrum in the individual contributions from the various Zeeman levels. The peaks on the left (red) end of the spectrum are the $\Delta m = -1$ transitions, while the peaks on the right (blue) are from the $\Delta m = +1$ transitions. High-field-seeking levels dominate

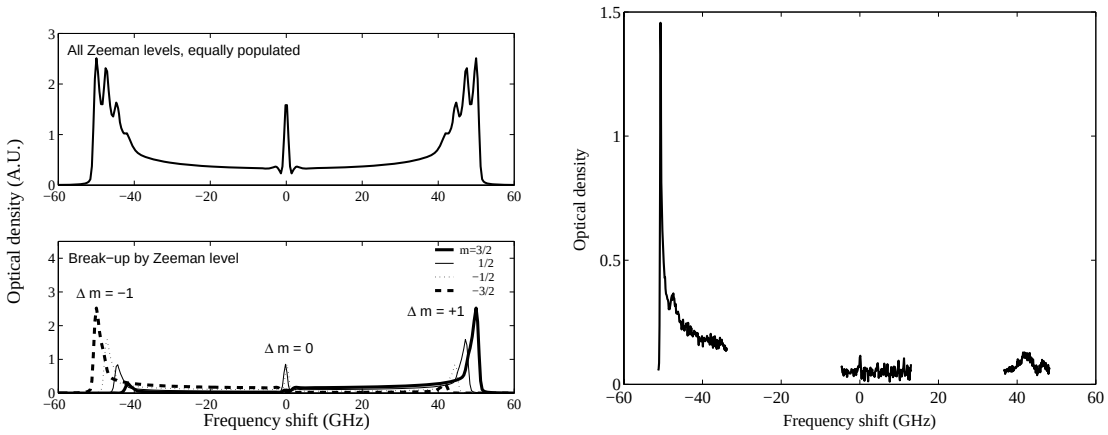

(a) Simulation (b) Measured

Figure 3.6: Sc spectra in the anti-Helmholtz field, with $B = 3.8$ T at the saddle points. (a) Simulation assuming uniform atom density in the cell. The top panel shows the simulated spectrum for equal populations in all Zeeman levels. The bottom panel breaks up this spectrum into the contributions from the individual Zeeman levels. (b) Observed spectrum 50 ms after the ablation pulse. We are unable to scan the laser over the entire frequency range, so this spectrum is pieced together from separate observations. The asymmetry in the spectrum compared to the simulation is due to Zeeman relaxation.

the left-hand side of the spectrum since the Clebsch-Gordon coefficients linking the ground and excited states favor $\Delta m = -1$ transitions for these levels. Similarly, low-field-seeking levels dominate the blue end of the spectrum. The peaks near zero frequency shift are from $\Delta m = 0$ transitions, which experience very little Zeeman broadening.

A spectrum measured 50 ms after the ablation pulse is shown in Fig. 3.6b. We are unable to scan the laser over the entire frequency range, so this spectrum is pieced together from 10 spectra spanning 17 GHz each. The relative frequency of each section is found using a wavemeter. We do not see a symmetric spectrum as in the simulation. Instead, we see that the low-field-seeking end of the spectrum is greatly

suppressed due to Zeeman relaxation of low-field seekers to high-field-seeking states. At 50 ms, the Sc atoms have achieved complete Zeeman thermalization, so that the Zeeman temperature has merged with the translational temperature of the gas. This puts a lower limit on the inelastic collision rate, but for a more precise measurement we wish to observe the Zeeman relaxation taking place. During the initial Zeeman thermalization, when the Zeeman temperature is much higher than the translational temperature, the low-field-seekers (LFS) decay as $\dot{n}_{\mathrm{LFS}} = -\Gamma_{\mathrm{in}} n_{\mathrm{He}} n_{\mathrm{LFS}}$. By fitting for the exponential decay time constant, we can find the inelastic collision rate coefficient $\Gamma_{\mathrm{in}} = (n_{\mathrm{He}} \tau_{\mathrm{in}})^{-1}$.

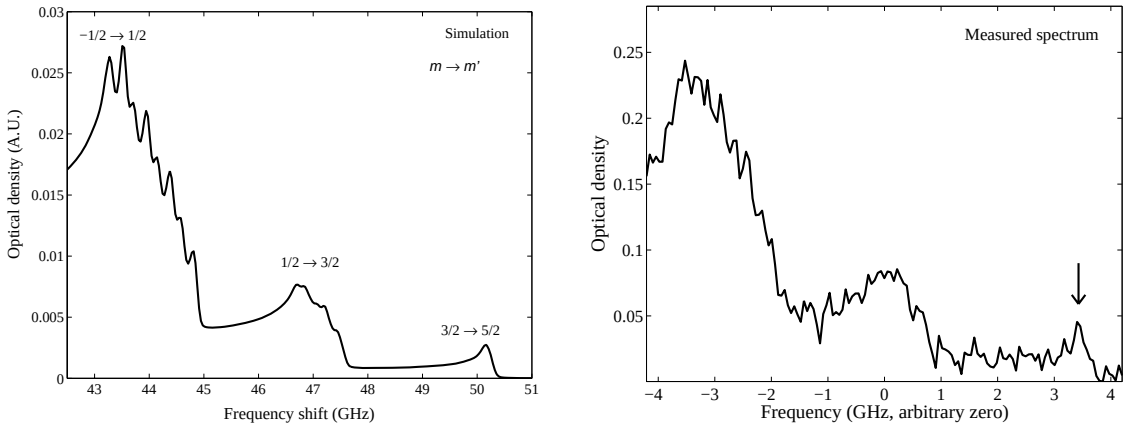

(a) Simulation (b) Measured

Figure 3.7: Centering guide for finding the low-field seeking, $m_J = +3/2$ absorption peak. (a) Simulation of $\Delta m = +1$ field-saddle peaks with the Zeeman levels thermalized to 1 K. (b) Measured spectrum, indicating where we center the laser for measuring the $m_J = +3/2$ absorption time profile. Comparing the two spectra, we are assured of measuring the absorption for the correct Zeeman level.

3.4.5 Inelastic collisions with He

We monitor the populations of the $m_J = \pm 3/2$ levels over time and use Eq. (3.3) to calculate the Zeeman temperature time profile. As shown in Fig. 3.6a it is possible to monitor the $m_J = \pm 3/2$ populations at the field saddles without spectroscopic interference from other Zeeman levels. Rather than scan over the peaks, we park the laser at the peak absorption frequency for each level so that we maximize the signal-to-noise and the time resolution (the laser has a limited scan rate). The wavemeter is not precise enough for setting the laser frequency on the absorption peaks. Instead, we scan the laser over the peak and adjust the center frequency until we are well centered on the peak, then stop scanning for subsequent measurements. The peaks are broad enough that any subsequent laser drift is unimportant.[2] The $m_J = -3/2,\ \Delta m = -1$ peak is easy to locate since it is the largest peak overall. The $m_J = +3/2,\ \Delta m = +1$ peak is more difficult since it is quite small, and after tens of milliseconds is almost lost in the noise.[3] To be sure that we center on the correct peak, we compare scanned spectra to a simulation with the Zeeman levels fully thermalized to a temperature of 1 K. Fig. 3.7 shows such a comparison, and indicates where we park the laser for the $m_J = +3/2$ population time profile measurements. It may seem odd that the various m_I lines are resolved for the $m = -1/2 \rightarrow m' = 1/2$ and $m = 1/2 \rightarrow m' = 3/2$ transitions, whereas only one line is visible for the $m = 3/2 \rightarrow m' = 5/2$ transition. This is merely a coincidence. In the high-field limit, the energies of the $|m_I, m_J\rangle$ eigenstates are:

[2]For narrow absorption peaks, the laser drift may be corrected; see Sec. 2.2.1.

[3]While the $m_J = +3/2$ state should start out with as many atoms as the $m_J = -3/2$ level, during the time it takes to scan the laser to acquire the centering information, most of the $m_J = +3/2$ atoms have relaxed to high-field seeking states.

$$E = g_J m_J \mu_B B + A m_I m_J, \tag{3.6}$$

where A is the hyperfine magnetic dipole coupling constant. For simplicity, we ignore the electric quadrupole coupling, which is small for Sc. The splitting between adjacent m_I levels at high field is then $\Delta f = A m_J$. The splittings happen to be about equal for the ground $m_J = 3/2$ and excited $m'_J = 5/2$ manifolds. The $m_J = 3/2$ manifold has a splitting between m_I states of (270 MHz)(3/2) = 405 MHz while the m'_J manifold has a spacing of (170 MHz)(5/2) = 425 MHz. Thus the splitting between adjacent m_I absorption peaks is only 20 MHz.

We average several sets of absorption profiles for each level to improve signal-to-noise and to average out variations in the number of atoms produced in the ablation. The measured profiles for the first 20 ms after the ablation pulse are shown in Fig. 3.8. While the number of atoms in the $m_J = -3/2$ remains fairly constant during this time, the number of atoms in the $m_J = +3/2$ state falls by a factor of 15. Are we seeing the Zeeman temperature come into equilibrium with the translational temperature? To answer this, we calculate the Zeeman temperature from the ratio of these two populations using Eq. (3.3) and compare with the translational temperature measured by fitting Voigt profiles to zero-field Sc spectra. The results are plotted in the lower panel of Fig. 3.8. We see that the Zeeman temperature has already merged with the translational temperature at our earliest measurement at 2 ms. The decrease in $m_J = +3/2$ level population seen is due to the cooling of the buffer-gas. As the translational temperature lowers, so does the fraction of atoms in the low-field-seeking state, so that the Zeeman and translational temperatures agree. While we are unable to observe the exponential decay of low-field-seekers as the Zeeman thermalization takes place, we know that this decay occurs before 2 ms, and so we place a lower limit

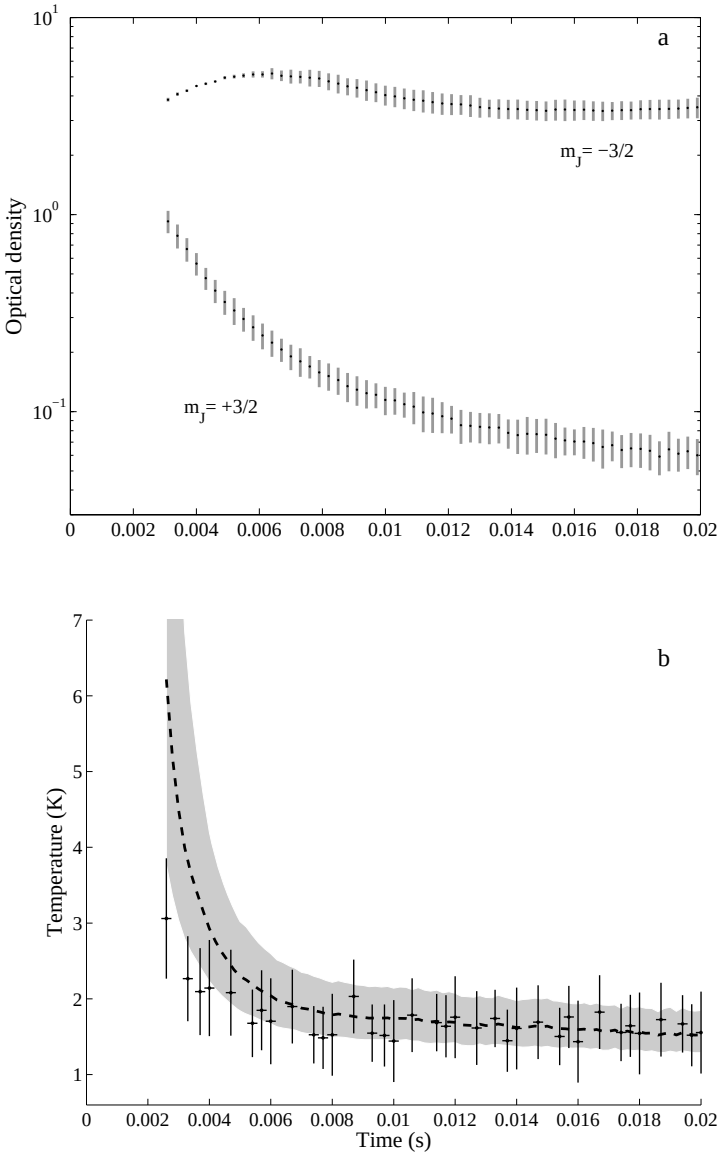

Figure 3.8: Zeeman level populations and temperature comparison for Sc atoms in a 3.8 T field. (a) Observed peak optical density (proportional to atom number) of Sc atoms in the $m_J = \pm 3/2$ levels as a function of time following a 10 mJ ablation pulse at time $t = 0$. The vertical bars and points are the mean and standard deviation obtained by time binning the combined data from four $m_J = -3/2$ and 10 $m_J = +3/2$ profiles. (b) Zeeman temperature (black line with error bars indicated by the shaded region) calculated from the level populations using Eq. (3.3), along with the measured translational temperature (black circles). The inelastic collision rate is large enough that the Zeeman temperature tracks the translational temperature of the gas.

on the inelastic collision rate coefficient of $\Gamma_{\text{in}} > 10^{-14}$ cm^3 s^{-1}. This puts an upper limit on the ratio of elastic to inelastic collisions of $\gamma < (1.6 \pm 0.3) \times 10^4$.

3.5 Titanium

3.5.1 Zero-field spectrum

Titanium has five naturally occurring isotopes (see Table 3.2), two with finite nuclear spin. There is one dominant isotope, ^{48}Ti, with 74% natural abundance and zero nuclear spin. Fig. 3.9 shows a zero-field spectrum taken at a temperature of 1 K in which all five isotopes are clearly resolved. Multiple hyperfine lines are evident for the isotopes with finite nuclear spin, ^{47}Ti and ^{49}Ti.

Table 3.2: Titanium isotopes.

Isotope	Natural abundance (%)	I
^{46}Ti	8.25	0
^{47}Ti	7.44	5/2
^{48}Ti	73.72	0
^{49}Ti	5.41	7/2
^{50}Ti	5.18	0

3.5.2 Elastic collisions with He

We measure the Ti-^{3}He elastic-collision cross-section by observing the zero-field diffusion of Ti atoms through the buffer gas, and applying Eq. (3.1). Fig. 3.10 shows a one-body fit to the measured Ti number time profile, giving a diffusion time of 150 ± 10 ms. We find the Ti-^{3}He elastic cross-section $(1.5 \pm 0.6) \times 10^{-14}$ cm^2 at a temperature of 0.8 ± 0.2 K. Most of the error in the measurement is attributed

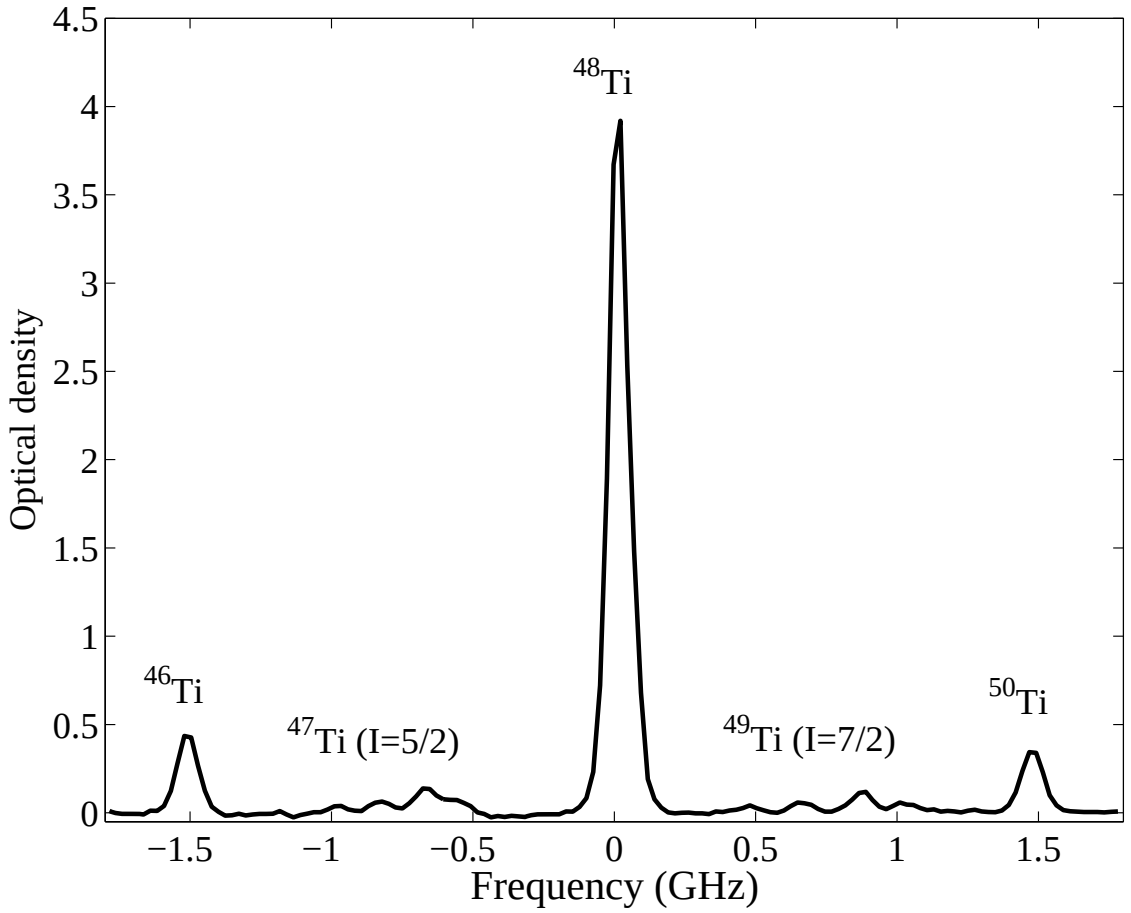

Figure 3.9: Zero-field spectrum of Ti at 1 K taken on the $^3F_2 \rightarrow {}^3D_1$ transition at 395 nm.

to the error in the Cr-^{3}He cross-section used to measure the buffer-gas density (see Section 3.3).

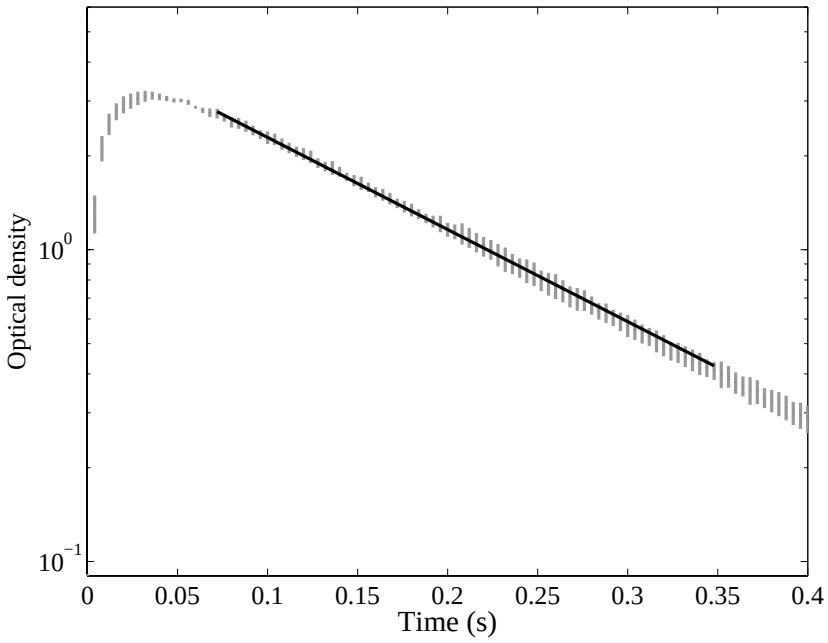

Figure 3.10: The observed peak optical density (proportional to number) of Ti atoms in the cell as a function of time following a 7 mJ ablation pulse at time $t = 0$. The gray vertical bars and points are the mean and standard deviation obtained by time binning the combined data from five measured diffusion profiles. The diffusion time constant is independent of ablation yield, so we "normalize" the five individual profiles so their optical densities are equal at a particular time (0.05 s) before averaging and finding the standard deviation. This prevents the variation in ablation yield from contributing to the error in the diffusion time constant. The black line is a fit to exponential decay and gives a diffusion time constant of 150 ± 10 ms.

3.5.3 Inelastic collisions with He in the anti-Helmholtz field

We measure the inelastic collision rate of Ti-^{3}He collisions by monitoring the populations of the high-field-seeking (HFS) $m_J = -2$ and low-field-seeking (LFS) $m_J = +2$ states over time in the anti-Helmholtz field. While the two populations should start out equal after the ablation pulse (the energies involved in ablation are much greater

than the Zeeman splittings between levels), LFS atoms relax to HFS states through inelastic collisions with the buffer gas.

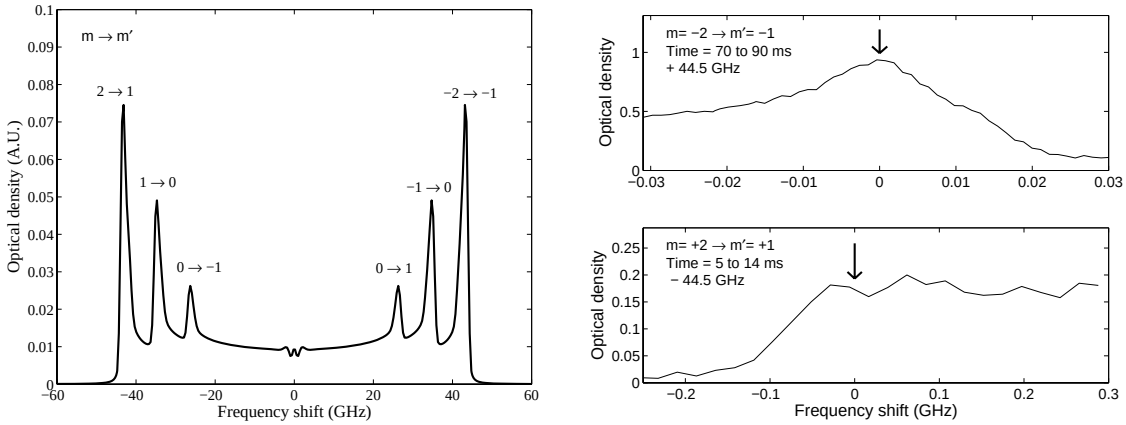

(a) Simulation (b) Measured spectra.

Figure 3.11: Ti spectra in the anti-Helmholtz field, with $B = 3.8$ T at the saddle points. (a) Simulation assuming uniform atom density in the cell, and uniform populations across the Zeeman levels. A gas temperature of 1 K is assumed. The low-field-seeking (LFS) field-saddle peak appears at a frequency shift of ~ -43 GHz from the field-free line, while the high-field-seeking (HFS) field-saddle peak appears at a frequency shift of $\sim +43$ GHz. (b) Measured HFS (upper plot) and LFS (lower plot) spectra used in centering the laser for the time profile measurements. The frequency shifts from the field-free line indicated in the upper-left corner of each plot are measured using the wavemeter. They agree well with the expected peak positions from the simulation. The arrows indicate the laser frequency used to measure the time profiles.

Fig. 3.11 shows a simulated Ti spectrum for the field strength used in these measurements, assuming uniform atom density in the cell and equal populations across Zeeman levels. Each absorption line is broadened by the inhomogeneous field from the field-free transition frequency for atoms at the center of the cell out to a maximum frequency shift for atoms at the field saddle regions, where the probe beam sees the highest magnetic field. Transitions with $\Delta m = +1$ are broadened toward the blue, while $\Delta m = -1$ transitions are broadened toward the red. Each line is peaked at

large frequency shift due to the large volume of atoms available at the flat saddle points of the field.

As with scandium, we monitor the atoms at the field saddle points so that we may spectroscopically distinguish the HFS and LFS atoms from atoms in the other Zeeman levels. The field-saddle peaks are well separated by > 8 GHz, allowing us to use the wavemeter to locate each peak. Fig. 3.11 shows the centering scans taken prior to parking the laser on the HFS and LFS saddle peaks for the population time profile measurements. The center frequencies of each spectrum relative to the ^{48}Ti field-free frequency are indicated and agree well with the peak positions from the simulation.

The measured profiles for the first 20 ms after the ablation pulse are shown in Fig. 3.12. We calculate the Zeeman temperature from the ratio of these two populations using Eq. (3.3) and compare with the measured Sc translational temperature profile. For the Sc temperature measurements, we fit Voigt profiles to spectra taken using a fast-scanning diode system (see Section 3.4.2). We do not directly measure the Ti translational temperatures since we do not have a diode that covers any strong optical transitions in Ti. We are unable to scan the Ti:sapphire laser used in Ti detection faster than a rate of ~ 40 Hz (*i.e.* 12.5 ms per spectrum) due to the limited speed of the resonant doubling cavity locking circuitry.[4] We expect, however, the translational temperature profile for Ti to be the same as that for Sc for the same ablation power and buffer-gas density. The temperature profile for Ti is verified by direct measurement in the second run of the experiment as discussed in Section 3.5.4.

[4]We discovered later that it would be possible to generate sufficient laser power for the probe beam by single-pass doubling through the crystal. We are then limited only by the scanning speed of the Ti:sapphire laser. Direct translational temperature measurements were made on Ti in the second run of the experiment, see Section 3.5.4.

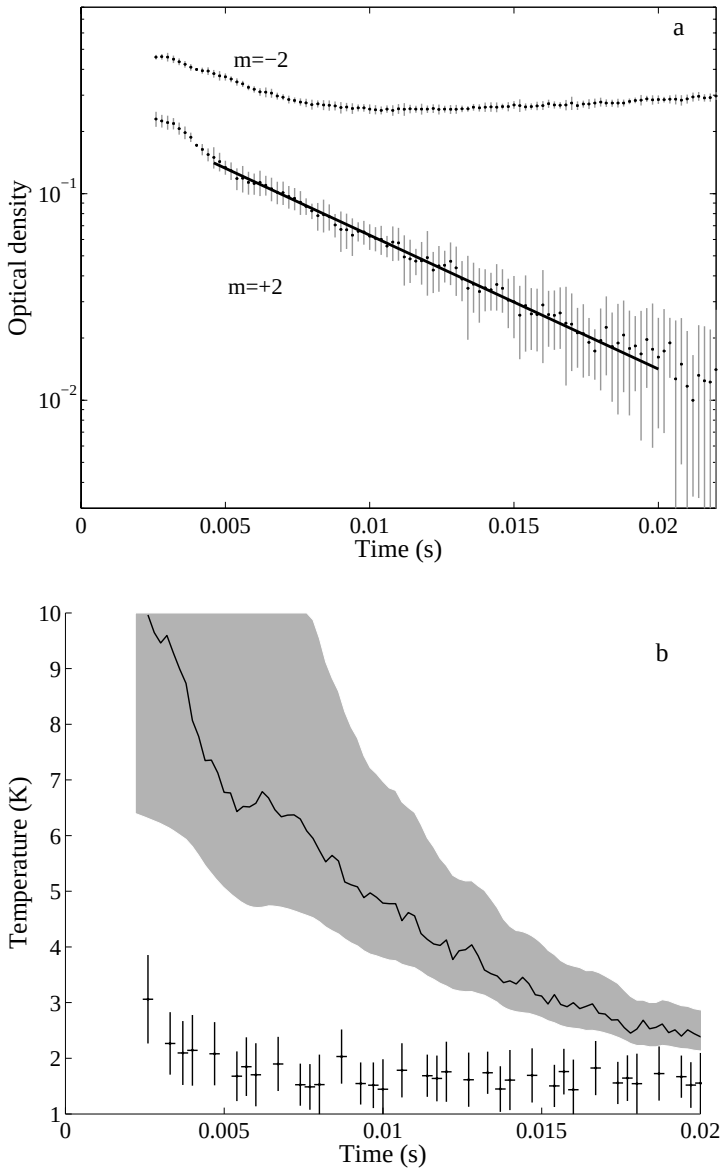

Figure 3.12: Zeeman level populations and temperature comparison for Ti atoms in a 3.8 T field. (a) Observed peak optical density (proportional to atom number) of Ti atoms in the $m_J = \pm 2$ levels as a function of time following a 10 mJ ablation pulse at $t = 0$. The vertical bars and points are the mean and standard deviation obtained by time binning the combined data from 15 sets each of $m_J = -2$ and $m_J = +2$ profiles. (b) Zeeman temperature (gray dashed line with error bars indicated by the shaded region), and measured Sc translational temperature (crosses). We expect the Ti translational temperature profile to be the same is that for Sc. The Zeeman temperature is initially very high, and merges with the translational temperature over 20 ms. We fit the exponential decay of the $m_J = 2$ level over this time, and find a decay constant of $\tau_{\text{in}} = (6 \pm 3)$ ms.

The Zeeman and translational temperatures are compared in Fig. 3.12. The Zeeman temperature is initially much higher than the translational temperature; the Zeeman level populations thermalize to the translational temperature over tens of milliseconds. We fit the observed exponential decay of atoms in the low-field-seeking $m_J = 2$ state over this time period to obtain the inelastic decay time $\tau_{\text{in}} = (6 \pm 3)$ ms. We use the measured buffer-gas density n_{He} to find the inelastic collision rate coefficient, $\Gamma_{\text{in}} = (\tau_{\text{in}} n_{\text{He}})^{-1}$. At a translational temperature of 1.8 K, $\Gamma_{\text{in}} = (1.1 \pm 0.7) \times 10^{-14}$ cm^3 s^{-1}, giving a ratio of elastic to inelastic collisions of $\gamma = (1.3 \pm 0.5) \times 10^4$. Comparing this result to values of γ near unity for O and Sr*, we see that inelastic collisions for Ti are highly suppressed.

3.5.4 Inelastic collisions with He in the Helmholtz field

We confirm our results for Ti in the second run of the experiment, where we run the magnet Helmholtz for improved signal-to-noise. We also directly measure the Ti translational temperature.

For the inelastic collision rate measurement, we ablate the Ti atoms into the buffer gas with a current of 20 A in each coil, producing a field of ∼2.3 T along the probe beam. A buffer-gas density of $(7.6 \pm 3.3) \times 10^{15}$ cm^{-3} is used. Fig. 3.13 shows the measured time profiles of the absorption from the HFS ($m_J = -2$) and LFS ($m_J = +2$) Zeeman levels. Their populations begin roughly equal, but the LFS atoms preferentially decay over the first ∼50 ms due to inelastic collisions.

We calculate the corresponding Zeeman temperature profile from the ratio of these two populations using Eq. (3.3), and compare the result to the measured translational temperature (Fig. 3.14). Here we measure the Ti translational temperature directly by fitting Voigt profiles to spectra taken at zero magnetic field. We are generally

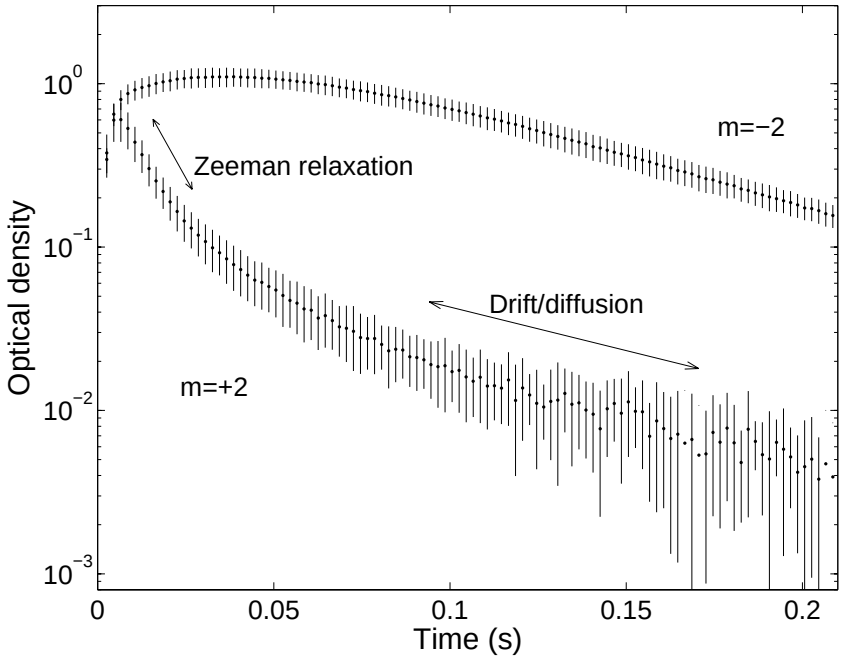

Figure 3.13: Peak optical density (proportional to atom number) of Ti atoms in the $m_J = \pm 2$ Zeeman levels as a function of time following a 10 mJ ablation pulse at time $t = 0$ in a 2.3 T magnetic field. The vertical bars and points are the mean and standard deviation obtained by time binning the combined data from 8 sets each of $m_J = -2$ and $m_J = +2$ profiles.

limited in how fast we may frequency scan the Ti:sapphire laser by the speed of the locking circuitry for the resonant doubling cavity. Since all the action in the LFS decay is happening in the first tens of milliseconds, we need millisecond resolution in our translational temperature measurements. To achieve a high scan rate, we frequency double the Ti:sapphire output with a single-pass through the doubling crystal. This cuts down our available probe power significantly; however, we generally attenuate the probe beam regardless to avoid optical pumping and power broadening effects. For the narrow scan widths needed to cover the ^{46}Ti zero-field absorption peak (0.2 GHz fundamental), we are able to frequency scan the laser at rates up to 200 Hz.[5] We

[5]As a gauge for how quickly we may scan the laser without damaging any of

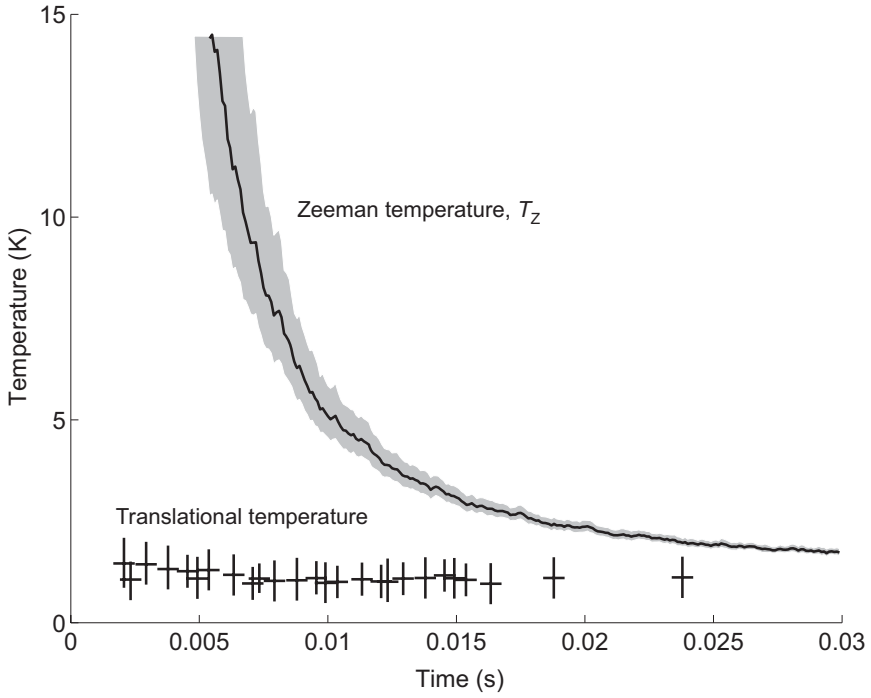

Figure 3.14: Ti Zeeman temperature (black line with error bars indicated by the shaded region) measured in the Helmholtz field, and measured translational temperature (crosses). The Zeeman temperature is initially very high, and merges with the translational temperature tens of milliseconds.

find that the laser scan is well-behaved for this scan rate, however the scan width is narrower than expected. We calibrate the scan width by comparing the Ti Doppler-broadened linewidth for fast and slow scans at the same time delay following the ablation pulse.

As with the anti-Helmholtz measurement, we find that the Zeeman temperature is initially much higher than the translational temperature, and falls over tens of milliseconds. We fit the early part of the decay of the $m_J = +2$ level, where $T_{\mathrm{Z}} >> T_{\mathrm{trans}}$, for exponential decay to get the inelastic decay time, $\tau_{\mathrm{in}} = 12 \pm 3$ ms. This

the scanning actuators, we limit the scan rate in GHz/s to what can be performed internally using the control box that came with the laser. This control box has a maximum 10 GHz scan width and maximum 4 Hz ramp rate, so for a 0.2 GHz scan width, so we assume it's safe to use a 200 Hz ramp rate.

is a factor of two longer than in the anti-Helmholtz measurement, providing good agreement for $\Gamma_{\rm in}$ since the buffer-gas density is now a factor of two smaller. We find $\Gamma_{\rm in} = (1.1 \pm 0.6) \times 10^{-14}$ cm^3 s^{-1}. The error on $\Gamma_{\rm in}$ is not much improved since most of the error is due to the uncertainty in the gas temperature and in the buffer-gas density rather than the uncertainty in $\tau_{\rm in}$.

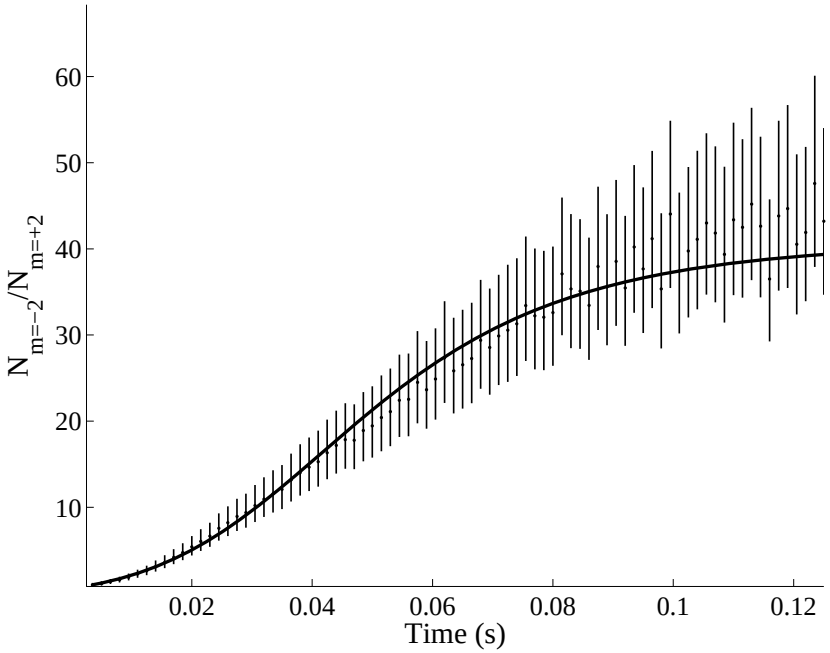

Figure 3.15: Ratio of Ti atoms in HFS and LFS states ($m_J = -2$ and $m_J = 2$, respectively) as a function of time following the ablation pulse. The fit uses the relaxation model Eq. (3.4) and finds $\Gamma_{\rm in} = 1.0 \times 10^{-14}$ cm^3 s^{-1} and $T_{\rm trans} = 1.1$ K.

The improvement in signal-to-noise allows us to follow the LFS state population at much later times, when the Zeeman level populations have relaxed to the translational temperature. Fig. 3.15 plots the ratio of HFS atoms to LFS atoms as a function of time. The ratio begins at unity, then steeply increases due to Zeeman relaxation via inelastic collisions. The ratio then levels off as the level populations come to their equilibrium values as described by a Boltzmann distribution at the translational

temperature. We use the model described by Eq. (3.4) to fit the ratio of atoms in the HFS and LFS states for $\Gamma_{\rm in}$ and $T_{\rm trans}$. We find $\Gamma_{\rm in} = 1.0 \times 10^{-14}$ cm^3 s^{-1}, in good agreement with the value found from fitting the early $m_J = +2$ decay, and $T_{\rm trans} = 1.1$ K, in good agreement with the Voigt profiles measurements at zero-field.

3.6 Yttrium

3.6.1 Egregious Ti:sapphire laser drift

Measurements on yttrium were hampered by difficulties in getting a stable output from the Ti:sapphire laser system at the wavelength needed for Y detection (408 nm, 24518.8 cm^{-1} see Table 2.3).[6] The output power was erratic, and the laser drift was egregious ($>$ 10 MHz drift in $<$ 1 s). We found that there is a strong water vapor absorption line at a frequency very close to half the Y transition frequency. The water vapor line is at 12259.60 cm^{-1} with a spectral line intensity of 1.7×10^{-23} cm^{-1}/(molecule cm^{-2}) and half-width (HWHM) of .4228 cm^{-1} [79]. Since our ring laser [65] has an open lasing cavity, it is not surprising that the output became unstable.

To help alleviate the problem, we tried sealing the openings in the case covering the laser with paperboard and tape, and flowing nitrogen (N_2) gas into the case. This helped somewhat, however we were unable to completely get rid of the extra laser drift.

[6]The output is frequency doubled, so the laser is tuned to half that frequency, or 12259.4 cm^{-1}.

3.6.2 Collisions with He

We measure the Y-^{3}He elastic-collision cross-section by observing the zero-field diffusion of Y atoms through the buffer gas, and applying Eq. (3.1). We find a diffusion time of (145±10) ms, which gives a Y-^{3}He elastic cross-section of $(1.4\pm0.6)\times10^{-14}$ cm^2 at a temperature of 0.8 ± 0.2 K. Most of the error in the measurement is attributed to the error in the Cr-^{3}He cross-section used to measure the buffer-gas density (see Section 3.3).

We measure the inelastic collision rate by monitoring the populations of the high-field-seeking (HFS) $m_J = -3/2$ and low-field-seeking (LFS) $m_J = +3/2$ states over time in the anti-Helmholtz field. The HFS level population is detected on the $\Delta m = -1$ transition to the $m'_J = -5/2$ manifold. The LFS population is detected on the $+3/2 \rightarrow +5/2$ transition. As with Sc and Ti, we monitor the atoms at the field saddle since these atoms will have the largest Zeeman line shifts, making them easy to isolate spectroscopically, and the flat saddle provides a large volume of atoms at constant field to interact with.

Each $m_J \rightarrow m'_J$ transition consists of $2I + 1$ discrete lines corresponding to $m_I = -I, \ldots, I$. [7] The splitting between adjacent m_I lines is $A'm'_J - Am_J$ (see Eq. (3.6)). For Sc this splitting is small (20 MHz), while for Y the splitting is 120 MHz, which is large enough that the $m_I = \pm1/2$ saddle absorption peaks are resolved. Fig. 3.16 shows a scan over the two HFS peaks. For monitoring the HFS population, we set the laser frequency to the peak of the outer (red) peak, which happens to correspond to atoms in the $m_I = 1/2$ hyperfine state. If we were to park the laser on the inner peak, we would have a combination of absorption from the

[7] There are only $2I + 1$ lines (rather than, say, $(2I + 1)^2$) since electric dipole transitions obey $\Delta m_I = 0$.

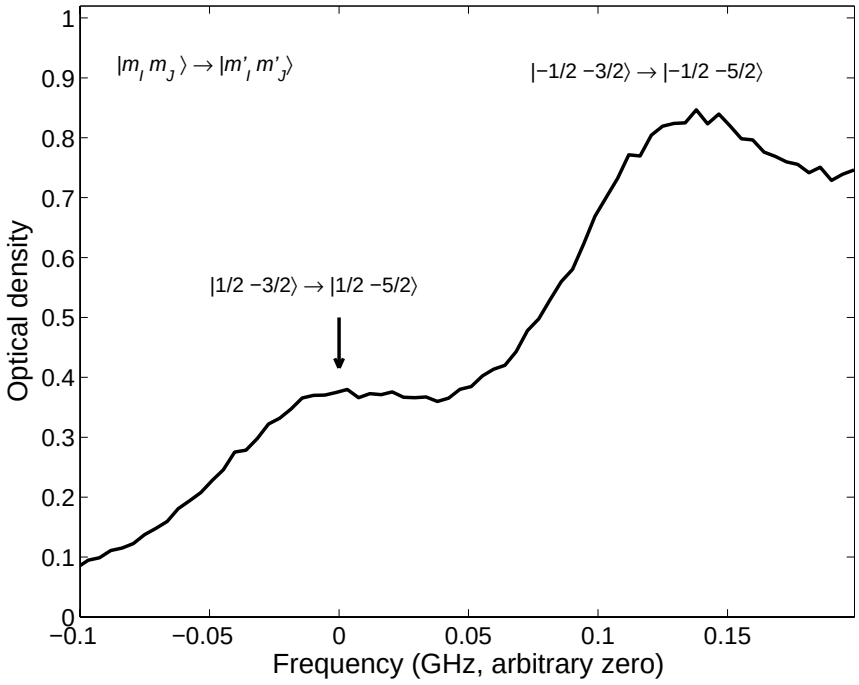

Figure 3.16: Spectrum of the Y field-saddle peaks (B=3.8 T) for the high-field-seeking $m_J = -3/2$ level. The spectrum is taken 62 GHz red of the field-free line. The peaks are from the two hyperfine levels ($I = 1/2$). The vertical arrow indicates where we set the laser frequency for the absorption time profiles of the $m_J = -3/2$ level.

$m_I = -1/2$ at the saddles, and $m_I = +1/2$ atoms at some lower field. The outer peak gives us a cleaner measurement. Similarly, for the LFS, we choose the outer (blue) peak, which again happens to correspond to the $m_I = 1/2$ hyperfine state. The transition strength does not depend on m_I, so it's not actually necessary to choose the same m_I value for the HFS and LFS transitions used in monitoring the populations.

The measured profiles for the first 10 ms after the ablation pulse are shown in Fig. 3.17. The number of LFS atoms decreases rapidly due to inelastic collisions. We calculate the Zeeman temperature from Eq. (3.3) and compare to the translational temperature (Fig. 3.17).[8] It appears that the Zeeman temperature has already

[8]We again use the measured Sc translational temperature since we do not have a

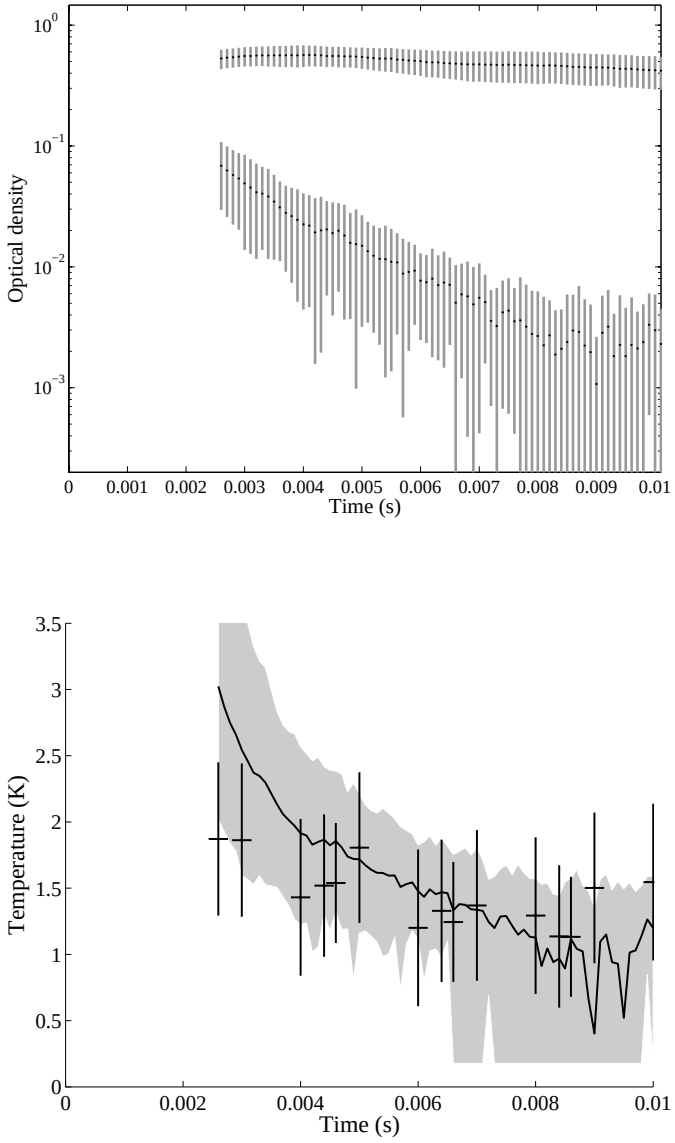

Figure 3.17: Zeeman level populations and temperature comparison for Y atoms in a 3.8 T field. The upper plot shows the observed peak optical density (proportional to atom number) of Y atoms in the $m_J = \pm 3/2$ levels as a function of time following a 6 mJ ablation pulse at $t = 0$. The vertical bars and points are the mean and standard deviation obtained by time binning the combined data from 20 $m_J = -3/2$ and 15 $m_J = +3/2$ profiles. The Zeeman temperature found from the ratio of these two populations (Eq. (3.3)) is shown in the lower plot (black line with error bars indicated by the shaded region), along with the measured translational temperature (black crosses). The Zeeman temperature tracks the translational temperature of the gas due to a high rate of inelastic collisions.

relaxed to the translational temperature at 2 ms, however, it is difficult to say this conclusively due to the large error bars on both the Zeeman and translational temperature measurements. We take 6 ms to be the upper limit on the inelastic decay time and place a lower limit on the Y-^{3}He inelastic collision rate of $\Gamma_{\rm in} > 5\times10^{-15}$ cm^3 s^{-1}. This puts an upper limit on the ratio of elastic to inelastic collisions of $\gamma < 3 \times 10^4$.

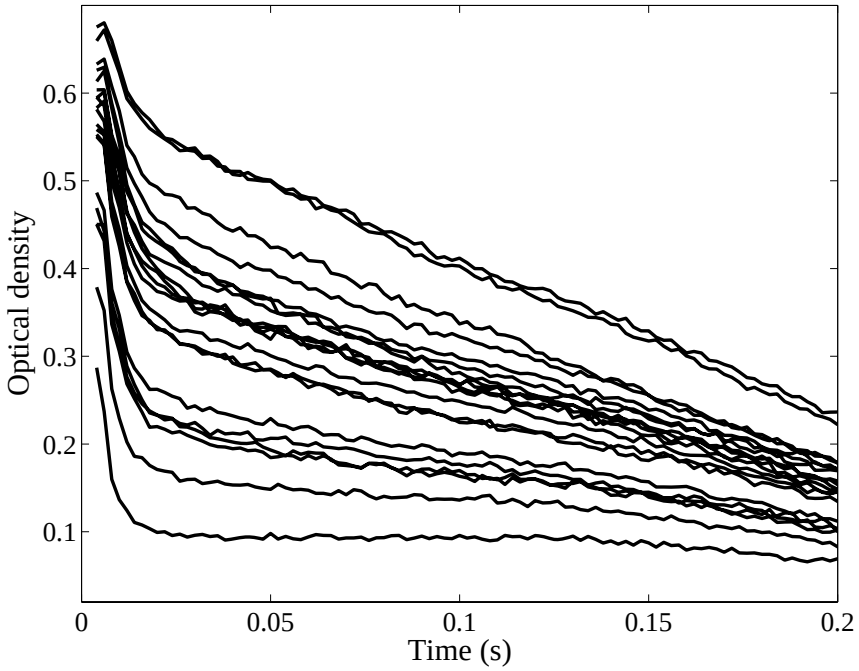

Figure 3.18: Successive absorption profiles for the yttrium $m_J = -3/2$ state at the field saddles following an ablation pulse at time $t = 0$. The large variation in profiles is likely due to laser drift.

The large error in the Zeeman temperature is due mainly to large variations in the absorption time profile for atoms in the HFS state. Fig. 3.18 shows several successive absorption profiles for the HFS, $m = -3/2$ level. The various HFS curves have very different shapes. This indicates that either the mass motion of the atoms is different shot-to-shot (this seems unlikely), or the laser frequency is drifting appreciably with

diode for the 408 nm yttrium transition.

time and is moving from the field saddle peak.

3.6.3 Hyperfine spectrum

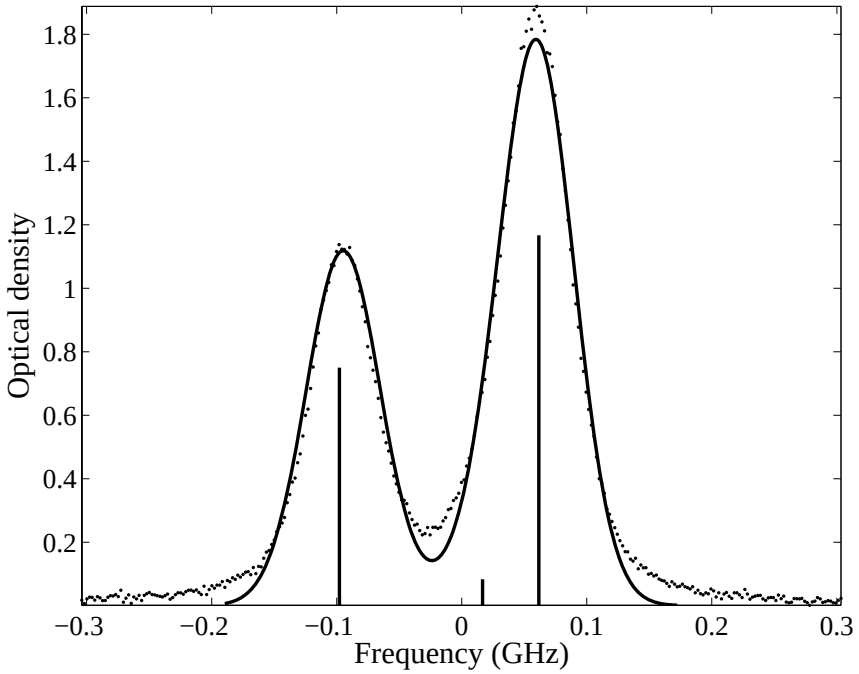

Figure 3.19: Y zero-field spectrum for the $^2D_{3/2} \rightarrow {}^2F_{5/2}$ transition at 408 nm. The fit to the spectrum shown by the solid line gives values for the excited state magnetic dipole hyperfine constant, $A' = (15 \pm 2)$ MHz. The vertical lines give the three line positions and relative intensities from the fit.

At zero magnetic field, the hyperfine interaction splits the ground (excited) levels of Y into two states with $F = 1, 2$ ($F' = 2, 3$), resulting in three transition lines. While the magnetic coupling constant for the ground state is known ($A = -57.217$ MHz) [80], we were unable to find a value for the excited state ($^2F_{5/2}$) constant in the literature.[9] We determine A' by fitting our measured zero-field Y spectrum using the formulas for the line positions and relative intensities found in

[9]There is no electric quadrupole interaction for Y ($I = 1/2$) since this interaction exists only for $I, J \geq 1$.

Appendix A. We find $A' = (15 \pm 2)$ MHz (see Fig. 3.19).

3.7 Zirconium

We are unable to measure the Zr-^{3}He inelastic collision rate due to inconsistent Zr ablation yields. Fig. 3.20 shows the average optical density $t = 0.2$ to 0.4 s after the ablation pulse for 9 successive pulses. The average optical density is proportional to ablation yield. After a few ablation pulses, the yield drops off dramatically. While the ablation beam may be steered to a new spot on the target to bring the yield back up, the yield again decreases after a few pulses. Inspection of the target does not reveal any hole-burning. The initial higher yields are probably due to surface roughness; there are likely narrow features on the surface that are easily ablated that get vaporized in the first few pulses. The bulk material remaining is more difficult to ablate and the yield decreases. This difficulty in ablating the bulk material is likely related to zirconium's high boiling point (4409 °C, compared to 2836 °C and 3287 °C for Sc and Ti, respectively).

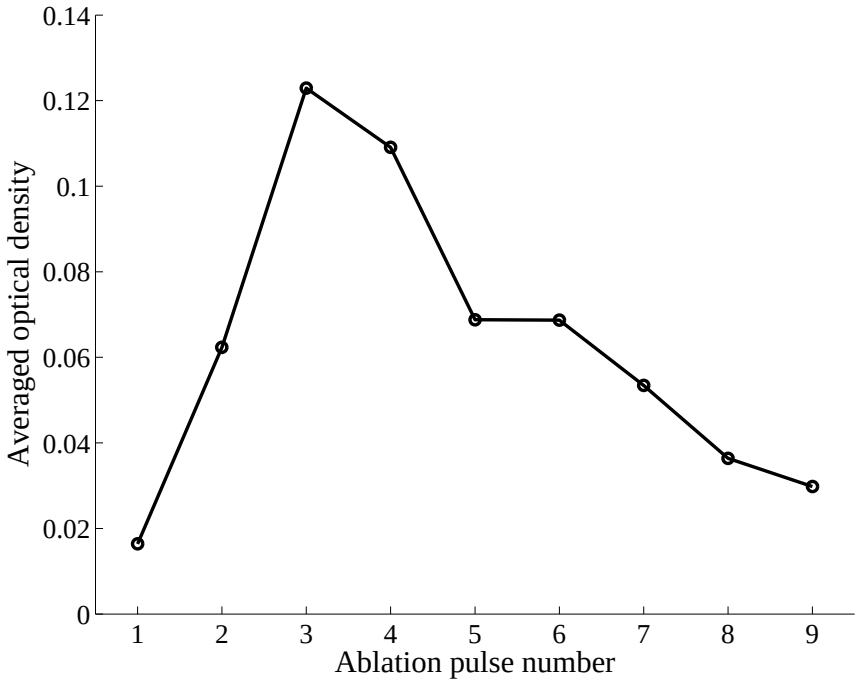

Figure 3.20: Erratic ablation yields for Zr. Plot shows the integrated optical density (proportional to ablation yield) for successive Zr ablations. After a few ablation cycles, the number of atoms produced in the ablation decreases rapidly.

Chapter 4

Theoretical calculations of Ti-He and Sc-He collisions

The interaction anisotropy in complexes involving non-S-state atoms couples the rotational motion of the collision complex with the atomic angular momentum resulting in Zeeman relaxation of magnetically trapped atoms. Theoretical studies have shown that this interaction is strong in collisions of main-group non-S-state atoms Sr(P), Ca(P), and O(P), yielding ratios of the rate constants for elastic to inelastic collisions near unity [28, 37, 29].

We proposed that inelastic collisions would be suppressed in collision complexes with transition-metal atoms due to shielding of the unpaired electrons by a filled outer s shell. Our measurements of the elastic to inelastic collision rate ratio in Ti-He scattering bear this out (see Section 3.5.3).

Motivated by our experimental work, the elastic to inelastic collision rate ratios for Sc-He and Ti-He complexes were calculated by Krems *et al.* using *ab initio* interaction potentials [40, 81, 49]. They find that the interaction anisotropy is dramatically suppressed in each case, leading to ratios of elastic to inelastic collision rates orders

of magnitude larger than those for main-group atoms and in agreement with the experiment results. In this chapter we describe the theoretical framework for collisions of non-S-state atoms with helium and we provide a description of the above theoretical results for Ti-He and Sc-He collisions.

4.1 Theoretical framework

The total Hamiltonian describing the collision of an open-shell atom with finite orbital angular momentum L and electronic spin S with a structureless atom (e.g. helium) may be written as [29]

$$H = -\frac{1}{2\mu}\frac{d^2}{dR^2} + \frac{\boldsymbol{l}^2}{2\mu R} + V_{\rm SO} + V_{\rm ES} + V_{\rm B}, \tag{4.1}$$

where $\mathbf{R}$ is the internuclear separation, l is the orbital angular momentum of the collision, μ is the reduced mass, $V_{\rm SO}$ is the spin-orbit interaction in the open-shell atom, $V_{\rm ES}$ is the electrostatic interaction between the two atoms, and $V_{\rm B}$ is the interaction of the open-shell atom with the external magnetic field.

The second term in the Hamiltonian leads to the centrifugal barrier in the collision, and its eigenvalues are $l(l+1)/2\mu R^2$ for states of well defined orbital quantum number l.

The spin-orbit term is given by $V_{\rm SO} = A\ \mathbf{L}\cdot\mathbf{S}$, where A is a constant describing the spin-orbit coupling in the open-shell atom, and has eigenvalues corresponding to the energy levels of j states of the open-shell atom, where j is the total electronic angular momentum, $\mathbf{j} = \mathbf{L} + \mathbf{S}$.[1]

[1]It is clear from the identity $\mathbf{L}\cdot\mathbf{S} = \frac{1}{2}(j^2 - L^2 - S^2)$ that the eigenvectors of $V_{\rm SO}$ are the eigenvectors of j^2.

The centrifugal operator and the spin-orbit interaction are therefore diagonal in the uncoupled $|lm_l\ jm_j\rangle$ basis, where m_l and m_j are the projections of l and j on a space-fixed quantization axis. These basis functions correspond to the asymptotic states of the colliding atoms. We next consider the electrostatic interaction, which will in general not be diagonal in this representation and will provide coupling between the states. We defer discussion of the external field term to later in the chapter.

4.2 The electrostatic interaction

The electrostatic interaction between an open-shell atom and a closed-shell atom such as helium may be represented as a Legendre series [82, 83]

$$V_{\rm ES}(\mathbf{R}, \hat{\mathbf{r}}) = \sum_{\lambda} V_\lambda(R) P_\lambda(\hat{\mathbf{r}} \cdot \hat{\mathbf{R}}), \tag{4.2}$$

where $\mathbf{r}$ denotes collectively the position vectors of the electrons in the P-state atom. The $\lambda = 0$ term is spherically symmetric, while the terms with $\lambda > 0$ have angular dependence and represent the anisotropy of the electrostatic interaction. Due to symmetry considerations, the only non-zero terms in the expansion are for $\lambda = 0, 2, \ldots, 2L$.

For a more intuitive picture of the interaction, the expansion coefficients $V_\lambda(R)$ may be expressed in terms of the molecular Born-Oppenheimer interaction potentials $V_\Lambda(R)$, where Λ denotes the projection of the electronic orbital angular momentum $\mathbf{L}$ on the molecular axis. For a D-state atom, there are three Born-Oppenheimer potentials, V_Σ, V_Π, and V_Δ, where the subscripts Σ, Π, Δ, etc. correspond to $\Lambda = 0$,

1, 2, etc. The expansion coefficients V_λ are

$$\begin{aligned} V_0 &= 1/5(V_\Sigma + 2V_\Pi + 2V_\Delta) \\ V_2 &= (V_\Sigma - V_\Delta) + (V_\Pi - V_\Delta) \\ V_4 &= 9/5(V_\Sigma - V_\Pi) + 3/5(V_\Delta - V_\Pi). \end{aligned} \tag{4.3}$$

There are four Born-Oppenheimer potentials for an F-state atom, V_Σ, V_Π, V_Δ, and V_Φ. One has for the expansion coefficients

$$\begin{aligned} V_0 &= 1/7(V_\Sigma + 2V_\Pi + 2V_\Delta + 2V_\Phi) \\ V_2 &= 5/7(V_\Sigma - V_\Phi) + 15/14(V_\Pi - V_\Phi) \\ V_4 &= 9/7(V_\Sigma - V_\Delta) + 3/7(V_\Pi - V_\Delta) + 9/7(V_\Phi - V_\Delta) \\ V_6 &= 13/7(V_\Sigma - V_\Pi) + 13/14(V_\Delta - V_\Pi) + 13/70(V_\Delta - V_\Phi). \end{aligned} \tag{4.4}$$

In each case, the isotropic component (V_0) of the electrostatic interaction is given by an average of the potentials, while the anisotropic components ($V_{2,4,\ldots}$) depend on differences between the potentials. This makes intuitive sense since each potential represents a different orientation of the open-shell atom with respect to the internuclear axis. If the open-shell atom were fairly spherical, its orientation during the collision would not be too important and so the interaction potentials would be nearly degenerate. The anisotropic components of the electrostatic interaction would then be small according to Eq. (4.4), as expected. If the open-shell atom were very aspherical, the various potentials would be quite different, giving rise to large anisotropic terms in the electrostatic interaction according to Eq. (4.4). The amount of splitting between the various interaction potentials therefore gives the degree of anisotropy in the electrostatic interaction.

4.3 Suppression of the interaction anisotropy for transition-metal complexes

The Born-Oppenheimer potentials for Sc(^3D)-He and Ti(^3F)-He were determined using *ab initio* calculations [40, 81] and are shown in Figs. 4.1 and 4.2. In both

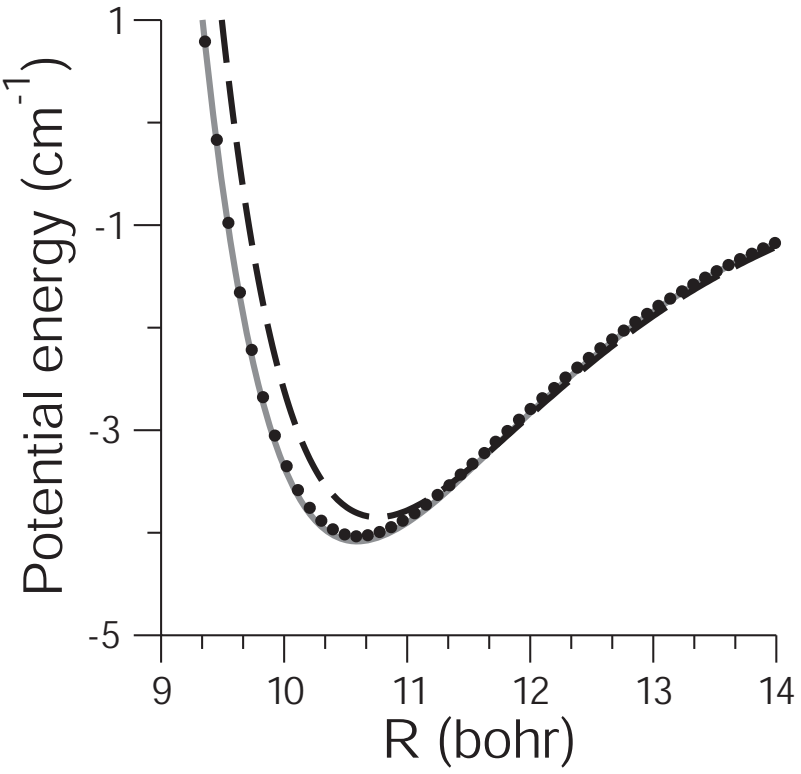

Figure 4.1: Sc(^3D)-He Born-Oppenheimer potentials: solid line—Σ symmetry; dashed line—Δ symmetry; filled circles—Π symmetry. From Reference [40].

cases, the van der Waals minima are very shallow and the potential curves are nearly degenerate at all R. From Eq. (4.4), the small splittings indicate that the anisotropy in the electrostatic interaction in the Sc-He and Ti-He complexes is suppressed.

The energy splitting between the potential curves (and thus the degree of the interaction anisotropy) may be characterized by the difference in the binding energy[2]

[2]The binding energy is the absolute value of the potential energy at the van der

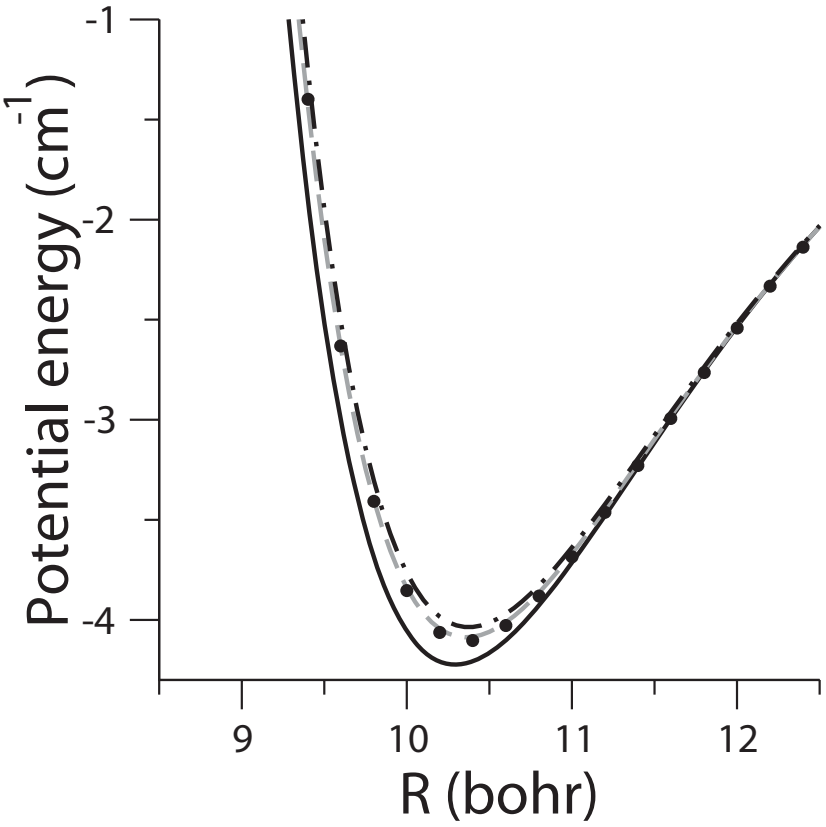

Figure 4.2: Ti(^3F)-He Born-Oppenheimer potentials: solid line—Σ symmetry; dashed line—Π symmetry; dot-dashed line—Φ symmetry; filled circles—Δ symmetry. From Reference [40].

of the different electronic states. We compare the binding energy difference in Ti and Sc complexes with those of main group atoms in Table 4.1. The differences in binding energy for Sc and Ti complexes with He are orders of magnitude smaller than for main group atoms.

We attribute the suppression of the interaction anisotropy for the transition-metal atoms to the shielding of the unpaired $3d$ electrons by the filled $4s$ shell. The average radius of the $4s$ orbital is more than two times larger than that of the $3d$ orbital [86] due to d-orbital collapse [42]. The helium atom experiences the strong, repulsive

Waals minimum.

Table 4.1: The absolute magnitude of the difference in the binding energy, ΔD, of the different electronic states for various open-shell atom-He complexes, representing the anisotropy of electronic interaction near the van der Waals minimum. [a]Measurements performed by glory analysis in a molecular beam at $T \sim 10^3$ K.

Atom	Configuration	ΔD (cm^{-1})	Reference
C(^{3}P)	$2p^2$	$D_\Sigma - D_\Pi = 25.31$	Theory [84]
O(^{3}P)	$2p^4$	$D_\Sigma - D_\Pi = 11.51$	Theory [29]
		$D_\Sigma - D_\Pi = 13.70$	Expt. [30][a]
Al(^2P)	$3p$	$D_\Sigma - D_\Pi = 15.74$	Theory [84]
S(^3P)	$3p^4$	$D_\Sigma - D_\Pi = 9.37$	Theory [84]
Cl(^2P)	$3p^5$	$D_\Sigma - D_\Pi = 13.83$	Theory [85]
		$D_\Sigma - D_\Pi = 5.27$	Expt. [31][a]
Ga(^2P)	$4p$	$D_\Sigma - D_\Pi = 24.87$	Theory [84]
Se(^3P)	$4p^4$	$D_\Sigma - D_\Pi = 8.69$	Theory [84]
Sc(^2D)	$3d4s^2$	$D_\Sigma - D_\Pi = 0.05$	Theory [40]
		$D_\Sigma - D_\Delta = 0.24$	Theory [40]
Ti(^3F)	$3d^24s^2$	$D_\Sigma - D_\Pi = 0.138$	Theory [40]
		$D_\Sigma - D_\Delta = 0.120$	Theory [40]
		$D_\Sigma - D_\Phi = 0.187$	Theory [40]

exchange interaction due to overlap with the $4s$ shell before it is able to sample the anisotropy of the submerged $3d$ shell. The exchange interaction is isotropic due to the spherical symmetry of the 4s shell, leading to nearly degenerate interaction potentials.

While the above mechanism is certainly plausible, one may nonetheless wonder if the suppression of the anisotropy is instead due to the D or F character of the atomic terms (main group elements are exclusively S or P ground states). To investigate this possibly, we make two comparisons. The first is to look at the first excited state of oxygen, O($2p^4\ ^1D$), which may be directly compared to Sc, also a D state. The O(^{1}D)-He interaction potentials found from *ab initio* calculations are shown in Figure 4.3 [81, 40]. The van der Waals minima are deep compared to the Sc case, with large splittings between the potentials. The binding energy difference between the Σ and Π states is 32.3 cm^{-1}– even higher than that for the O(^3P) ground state.

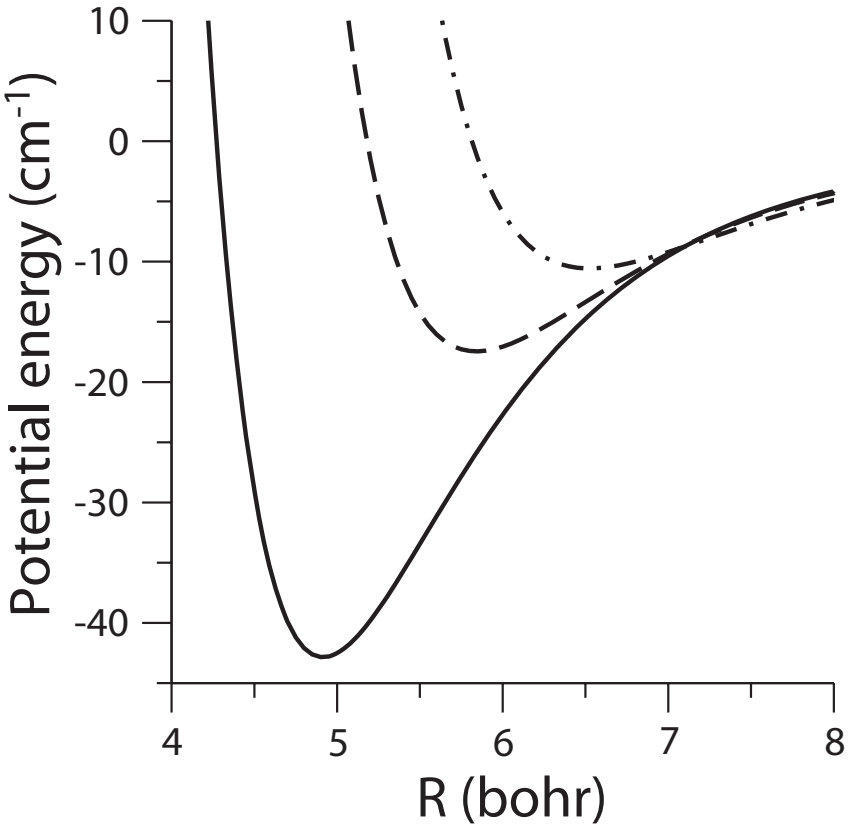

Figure 4.3: O(^1D)-He Born-Oppenheimer potentials: solid line—Σ symmetry; dashed line—Π symmetry; dot-dashed line—Δ symmetry. From Reference [40].

To further support the case that it is the shielding by the outer shell that suppresses the interaction anisotropy, we look at what happens when the $4s$ shell is removed from the titanium atom. The interaction potentials for the Ti^{2+}-He complex are shown in Figure 4.4 [81, 40]. The charged Ti^{2+} ion is able to polarize the He atom much more effectively than the neutral Ti atom can, so the magnitude of the electrostatic interaction is greatly increased. This charge-induced-dipole interaction should affect all three potentials in the same way since the helium polarizabilty is isotropic, resulting only in an overall change in the energy scale. The large splittings seen in the potentials[3] are due to the dispersion interaction, the allowance for

[3]Interestingly, the Σ and Φ potentials for Ti^{2+} are nearly degenerate, with a bind-

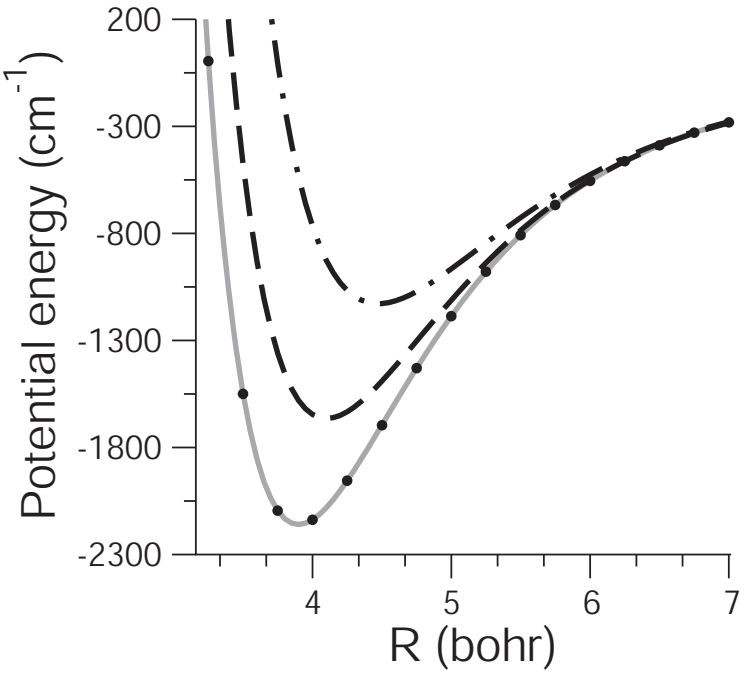

Figure 4.4: $Ti^{2+}(^3F)$-He Born-Oppenheimer potentials: solid line—Σ symmetry; dashed line—Π symmetry; dot-dashed line—Δ symmetry; filled circles—Φ symmetry. From Reference [40].

sd_σ hybridization which may reduce occupation of antibonding orbitals [87], and the strongly anisotropic exchange interaction due to the overlap of the now-exposed $3d$ Ti orbitals with the $1s$ He orbital. The large electrostatic anisotropy seen in the Ti^{2+}-He complex again reinforces the notion that the suppression of anisotropy in the Ti-He and Sc-He complexes is due to shielding by the outer $4s$ shell.

---

ing energy difference of 27 cm^{-1}. This difference is much larger than for neutral Ti, but the energy scale of the potentials is greatly increased for Ti^{2+} by the charge-induced-dipole interaction. Scaling this down by the ratio of the Σ binding energies for the doubly ionized and neutral Ti complexes, we have a binding energy difference of 27 $cm^{-1} \times (4)/(2200) = 0.04$ cm^{-1}, which is similar to the binding energy differences in the neutral Ti case.

4.4 Comparison of *ab initio* collision rates to experiment

Since the electrostatic interaction anisotropy provides the mechanism for angular momentum transfer in a collision, the suppression in the anisotropy for Sc and Ti complexes with helium should lead to a suppression in the inelastic collisions when an external magnetic field is applied (represented by the V_B term in Eq. 4.1).

The ratios of elastic to inelastic collision rates are calculated using the *ab initio* potentials as described in Reference [40] for Sc(^2D)-He and Ti(^3F)-He scattering at a field of 3.8 T and a temperature of 1.8 K and are listed in Table 4.2. The ratios of rate constants for O(^3P)-He and O(^1D)-He scattering are also shown for comparison [29, 40]. The large anisotropy in the electrostatic interaction seen for the oxygen complexes leads to dismal collision rate ratios near unity, while the inelastic collisions are suppressed for Sc-He and Ti-He, leading to elastic-to-inelastic ratios orders of magnitude larger.

Table 4.2: Ratio γ of rate constants for elastic and inelastic collisions at T=1.8 K and B=3.8 T.

Complex	γ_{theory}	γ_{exp}
O(^3P)-He	3	
O(^1D)-He	1.6	
Sc(^2D)-^{3}He	800	$< (1.6 \pm 0.3) \times 10^4$
Ti(^3F)-^{3}He	7000	$\sim (4.0 \pm 1.8) \times 10^4$

The theory for results for Sc-He and Ti-He scattering may be compared to the experimental measurements from the last chapter. The experimental values are again listed in Table 4.2 for convenience. The theory result for the ratio of elastic to inelastic collisions for Ti-He scattering is somewhat lower than the experimental value, but it

is within the error of the theory calculation. The collision rate ratio is sensitive to the splitting between the Ti-He potential curves (Figure4.2); due to the near degeneracy of the potentials the splitting cannot be precisely measured, resulting in a substantial error in the theoretical values for γ.

4.5 Implications for 2-body collisions and for the rare earths

These experimental and theoretical results have broad implications beyond collisions with Ti and Sc. All of the non-S-state transition-metal (TM) and rare-earth (RE) atoms have filled outer s shells which should suppress the interaction anisotropy in collisions. Additionally, the collapse of the d and f orbitals occurs in all of these atoms (see Section. 1.2.1). Naïvely, one would expect the suppression of inelastic collisions for RE-He collisions to be even larger than for the transition metals since the unpaired electrons in RE atoms are more deeply submerged beneath multiple filled shells. As described in the next chapter, this naïve expectation turns out to be correct. We do see a dramatic suppression of inelastic collisions for RE-He scattering with γ ranging 30,000 to 450,000, depending on the RE species. These large values for γ indicate that the electrostatic interaction is nearly spherical for RE-He collision complexes.

The low anisotropy of the electrostatic interaction for non-S-state TM and RE complexes with He suggests that the polarizabilty of these atoms is nearly isotropic and that angular momentum transfer in the atom-atom collisions must also be suppressed [41]. This is encouraging for the prospects for evaporative cooling of non-S-state TM and RE atoms to ultracold temperatures.

Chapter 5

Rare earth results

Following our observation of the suppression of Zeeman relaxation in Ti-He collisions, we decided to study the non-S-state rare-earth (RE) atoms. We expect a higher degree of suppression of inelastic collisions in the rare-earths since their unpaired electrons are further submerged beneath multiple filled shells. In addition, provided that the collision rates are favorable, their large magnetic moments make them amenable to trapping in our current apparatus. Table 5.1 gives the ground state term, magnetic moment and electron configuration for the entire row of lanthanides. For the experiment, we focus on the paramagnetic non-S-state lanthanides whose unpaired electrons are exclusively in the $4f$ shell since these atoms will benefit from shielding by two filled s shells ($5s$ and $6s$): Pr, Nd, Tb, Dy, Ho, Er, and Tm.[1] In this chapter we report on the suppression of Zeeman relaxation and magnetic trapping of these atoms.

[1]Pm would be on the list but has only radioactive isotopes.

Table 5.1: The Lanthanides. Listed are the ground-state term, magnetic moment μ (in units of μ_B) and electron configuration. The atoms studied (paramagnetic atoms whose unpaired electrons are exclusively in the $4f$ shell) are marked with a ✓. †Pm has no naturally occurring isotopes, and so is not included.

Atom	Term	μ/μ_B	Configuration	
La	$^2D_{3/2}$	1.20	[Xe]5d6s^2	
Ce	$^1G_4$	3.78	[Xe]4f5d6s^2	
Pr	$^4I_{9/2}$	3.29	[Xe]4f^{3}6s^2	✓
Nd	$^5I_4$	2.41	[Xe]4f^{4}6s^2	✓
Pm	$^6H_{5/2}$	1.83	[Xe]4f^{5}6s^2	†
Sm	$^7F_0$	–	[Xe]4f^{6}6s^2	
Eu	$^8S_{7/2}$	6.98	[Xe]4f^{7}6s^2	
Gd	$^9D_2$	5.30	[Xe]4f^{7}5d6s^2	
Tb	$^6H_{15/2}$	9.94	[Xe]4f^{9}6s^2	✓
Dy	$^5I_8$	9.93	[Xe]4f^{10}6s^2	✓
Ho	$^4I_{15/2}$	8.96	[Xe]4f^{11}6s^2	✓
Er	$^3H_6$	6.98	[Xe]4f^{12}6s^2	✓
Tm	$^2F_{7/2}$	3.99	[Xe]4f^{13}6s^2	✓
Yb	$^1S_0$	–	[Xe]4f^{14}6s^2	
Lu	$^2D_{3/2}$	1.20	[Xe]4f^{14}5d6s^2	

5.1 Stray fields

At the beginning of this run, we found that the absorption lines were asymmetric and greatly broadened. Figure 5.1a shows an example of a ^{48}Ti spectrum and the best Voigt profile fit. While we expect the gas temperature to be ∼1 K, the fit gives $T = 3.4$ K (a linewidth of 150 MHz, compared to an expected linewidth of 85 MHz).

We attribute the distorted line shape to Zeeman broadening caused by ferromagnetic samples in the cell. Immediately following the cooldown, the new magnet center tap (see Section 2.1.2) is tested by ramping each coil to 20 A, producing a field of 2 T at the samples. The samples reach their saturation magnetization in this field and, once magnetized, continue to generate a field in the cell even when the magnet coils are ramped to zero current.

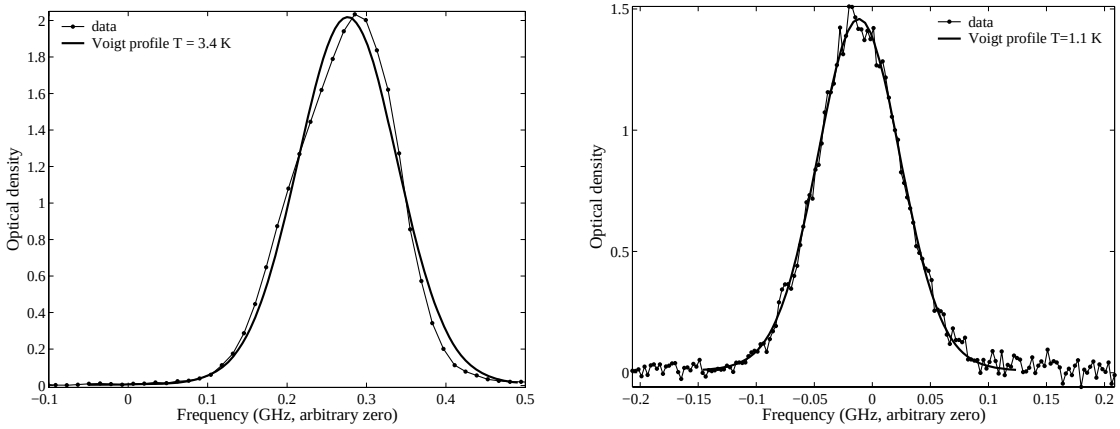

(a) Distorted peak (b) Normal peak

Figure 5.1: Ti absorption spectra with zero current in the magnet coils. (a) Spectrum taken early in the run, showing an asymmetric shape and broadening. The measured linewidth (FWHM) is 150 MHz. The broadening of the line is likely due to magnetized ablation targets in the cell. (b) Spectrum taken much later in the run, with a fit to a Voigt profile which gives a temperature of 1 K, as expected. The linewidth here is only 85 MHz.

We simulate the spectrum of Ti atoms in a uniform field using the method detailed in Section 2.2.6. We find that for atoms at a temperature of 1 K, a 45 Gauss field is required to reproduce the composite linewidth of 150 MHz. This field is too large to be accounted for by trapped fluxes in the superconducting magnet wire (the field from trapped fluxes was measured to be ∼10 Gauss [56]). We calculate that the field from a completely magnetized 0.1 mm × 3 mm × 3 mm piece of iron foil (this is the geometry of the Fe target in the cell) is roughly 10 Gauss at a distance of 1 cm. In addition to the iron target (a complete list of targets is given in Section 2.1.3), there are a number of ablation targets in the cell which are ferromagnetic at cryogenic temperatures, including Gd, Tb, Dy, Ho, Er and Tm.[2] It is a reasonable conclusion

[2]The Curie temperatures of Gd, Tb, Dy, Ho, Er, and Tm are 293, 220, 90, 20, 19 and 32 K, respectively.

that the observed line broadening is due to fields from these ferromagnetic targets.

In an attempt to demagnetize the targets, we ramp back and forth between positive and negative currents in the coils in an effort to scramble the magnetic domains in each target. We begin at a current of ± 1 A per coil, and decrease the magnitude of the current in 0.1 A steps until we are at 0 A. This has little effect on the lineshape. We find, however, that the samples do demagnetize over time. Figure 5.1b shows a Ti absorption spectrum taken late in the run, seven weeks after the initial spectrum. The peak fits well to a 1 K Voigt profile. The magnet is ramped up and down producing Tesla fields at the samples throughout the run, so it is unclear why his demagnetization occurs at all.

5.2 Zero-field spectra

All of the atoms studied have multiple naturally occurring isotopes and/or isotopes with finite nuclear spin. We were unable to find in the literature the isotope shifts and/or excited state hyperfine constants for Pr, Nd, Dy, Ho, and Er for the transitions used in the absorption detection (see Table 2.3). We are able to measure these constants from our zero-field spectra, and we present these results here.

We simulate each zero-field spectrum with the isotope shifts and excited-state hyperfine constants as variable parameters. For atoms with multiple isotopes, the peak heights in the simulations are fixed by the natural abundances. Hyperfine spectra are modeled using the formulas for line shifts and relative line intensities found in Appendix A. The simulation uses a Voigt profile for all absorption peaks with the temperature as a variable parameter.

The spectra are measured with the magnet ramped to zero current, and the leads disconnected from the power supply. Each spectrum is taken during one upward

or downward frequency sweep of the laser. The laser is ramped at 5 or 10 Hz, so each spectrum is taken over 50 or 100 ms. This is comparable to the diffusion time (Table 5.4) so we compensate for the loss of atoms during the measurement by applying factor $\exp(\Delta t/\tau_{\mathrm{d}})$ point-by-point across the spectrum, where τ_{d} is the diffusion time and Δt is the time relative to the start of the laser ramp.

Our results for the isotope shifts and hyperfine coupling constants are summarized in Tables 5.2 and 5.3, respectively. The measured zero-field spectra and fits are shown in Figure 5.2-5.6. The zero-field spectra for Pr and Ho span several GHz due to their large hyperfine coupling, and as a result, the individual absorption peaks occupy a small fraction of the scan width. For these atoms, the spectra are undersampled and the peaks appear broadened.[3] This does not much affect the values for the hyperfine coupling constants since this broadening is symmetric and we are still able to measure the peak center frequencies. The Dy spectrum appears to suffer from Zeeman broadening (see Sec. 5.1). The rest of the spectra, however, are taken later in the run when the ferromagnetic samples in the cell have demagnetized.

[3]The signals from each PMT are low-pass filtered, with the cutoff set to half the sampling rate.

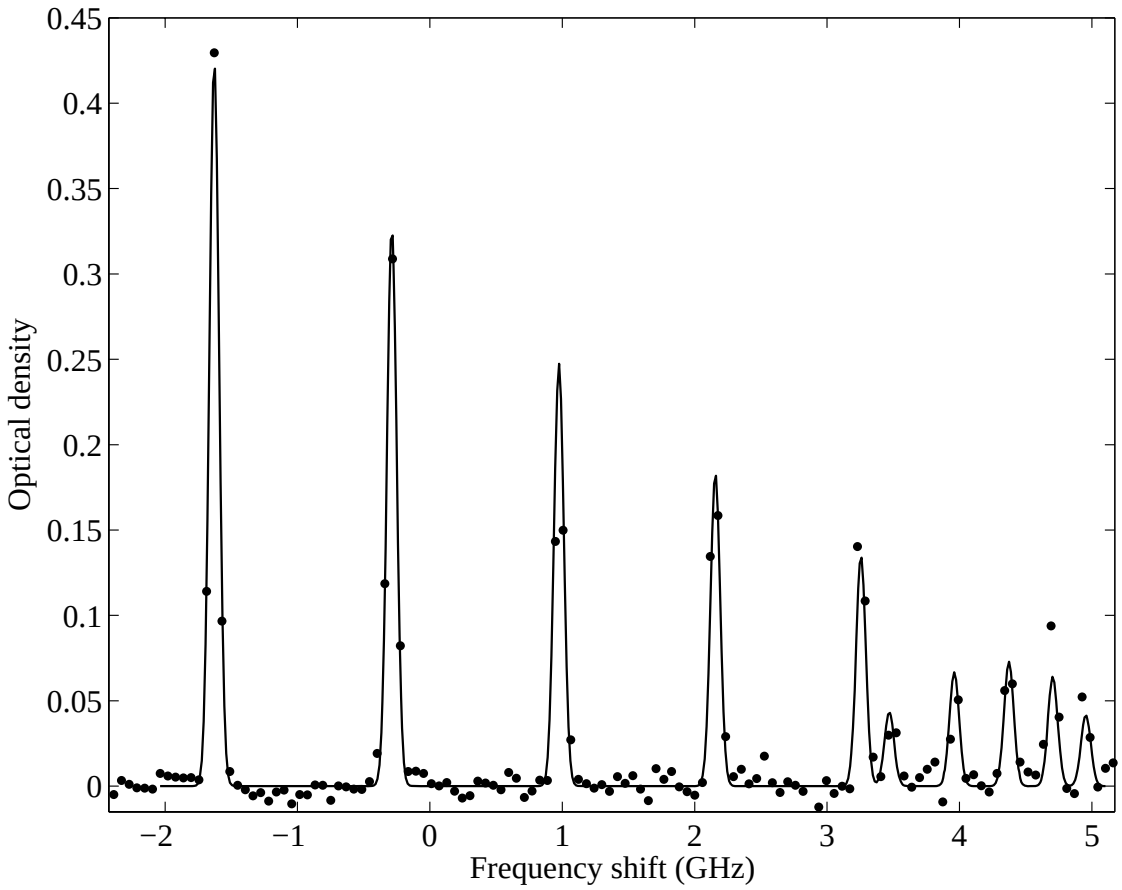

Figure 5.2: Pr zero-field spectrum for the $^4I_{9/2} \rightarrow {}^4L_{7/2}$ transition at 474 nm. Pr has one stable isotope, ^{141}Pr. The ground state hyperfine constants are A=926.209 MHz and B=-11.878 MHz [88]. The fit to the spectrum shown by the solid line gives values for the excited state hyperfine constants, $A' = (845 \pm 5)$ MHz and $B' = (0 \pm 100)$ MHz. This spectrum is somewhat undersampled, resulting in a broadening of the individual absorption peaks.

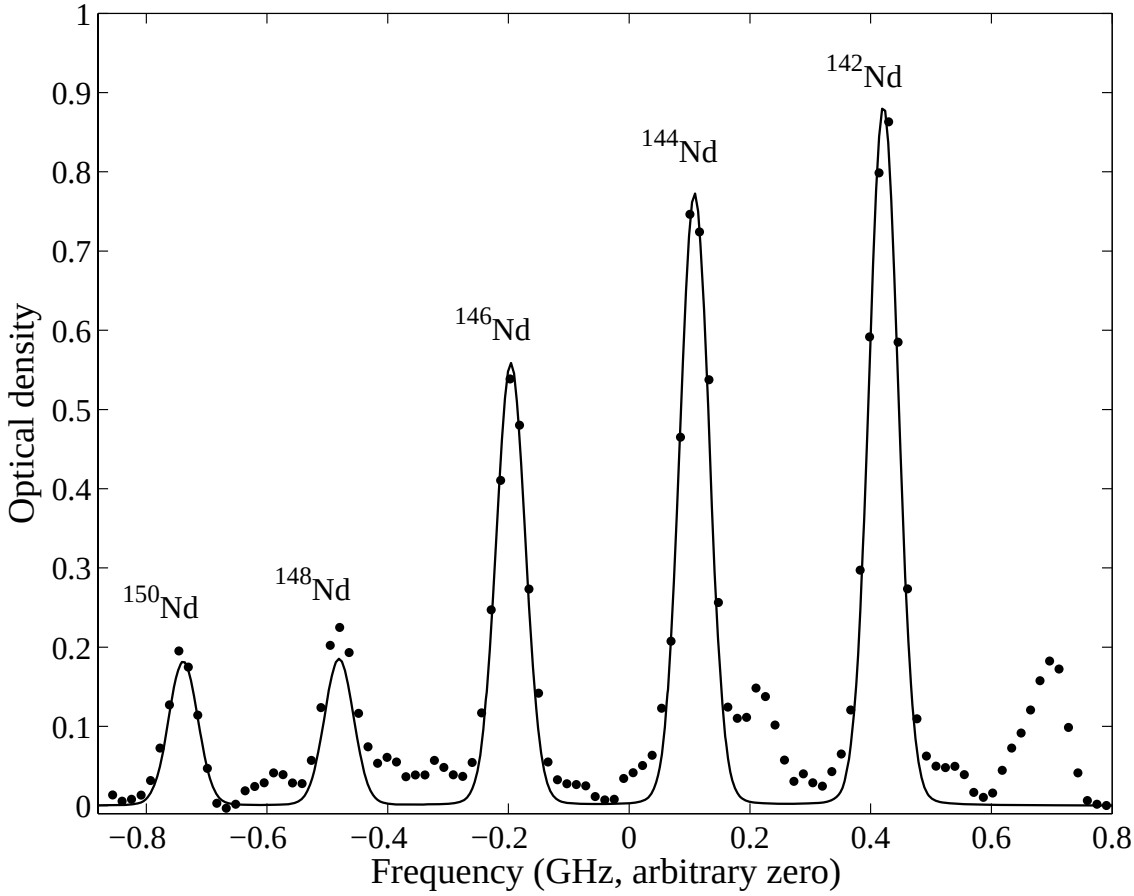

Figure 5.3: Nd zero-field spectrum for the ${}^5I_4 \rightarrow {}^5H_3$ transition at 464 nm. Nd has 7 stable isotopes, five with $I = 0$ (^{142}Nd, ^{144}Nd, ^{146}Nd, ^{148}Nd, ^{150}Nd) and two with $I = 7/2$ (^{143}Nd, ^{145}Nd). The simulation (solid line) includes only the $I = 0$ isotopes; the remaining peaks are hyperfine lines from ^{143}Nd and ^{145}Nd. The measured isotope shifts are listed in Table 5.2.

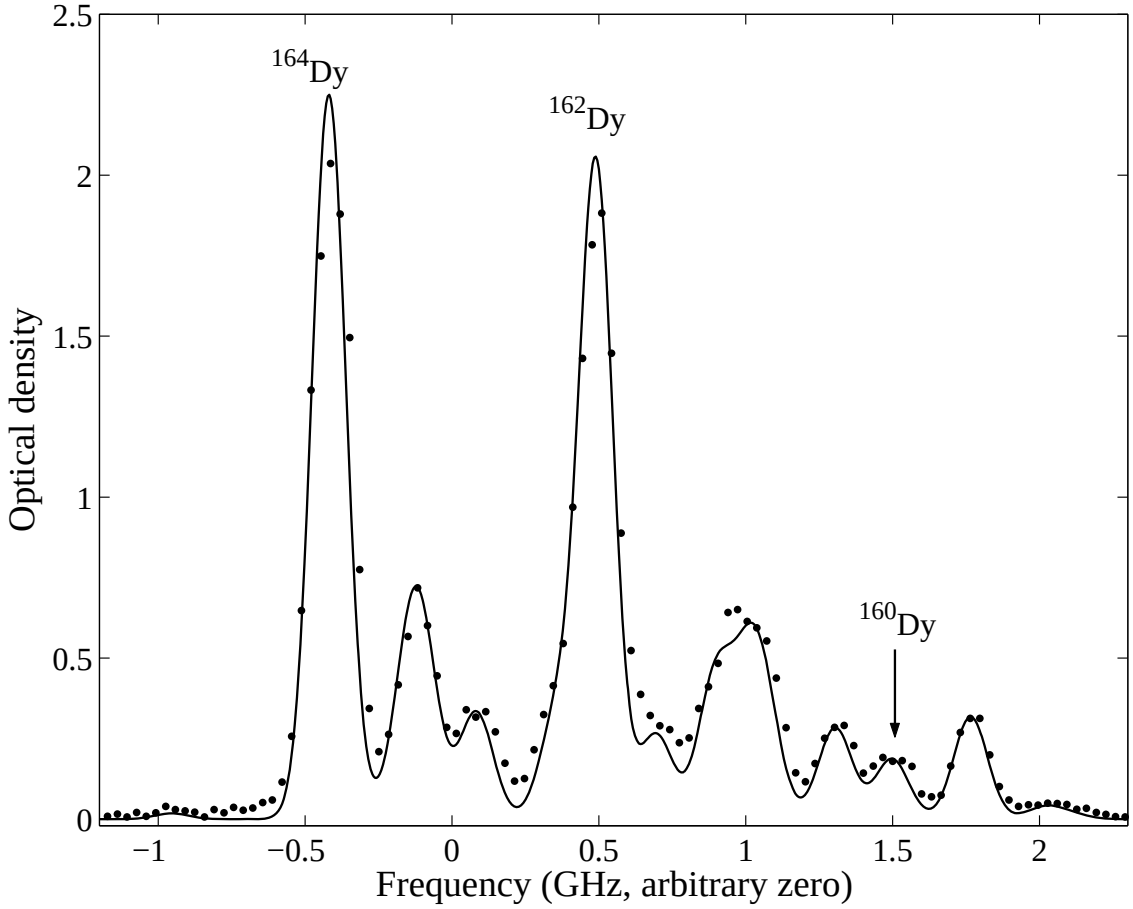

Figure 5.4: Dy zero-field spectrum for the $^5I_8 \rightarrow {}^5K_9$ transition at 421 nm. Dy has 5 stable isotopes with $> 1\%$ natural abundance, three with $I = 0$ (^{160}Dy, ^{162}Dy, ^{164}Dy) and two with $I = 5/2$ (^{161}Dy, ^{163}Dy). The absorption peaks from the isotopes with zero nuclear spin are indicated; the remaining peaks are hyperfine lines from ^{161}Dy and ^{163}Dy. We fit both the isotope shifts and excited state hyperfine coupling constants; the best fit is shown by the solid line (the ground state hyperfine constants are found in Reference [89]). The measured values are given in Tables 5.2 and 5.3. The absorption lines are broadened beyond the expected natural linewidth and Doppler broadening. This additional broadening is probably due to Zeeman broadening caused by the fields from magnetized ferromagnetic ablation targets in the cell.

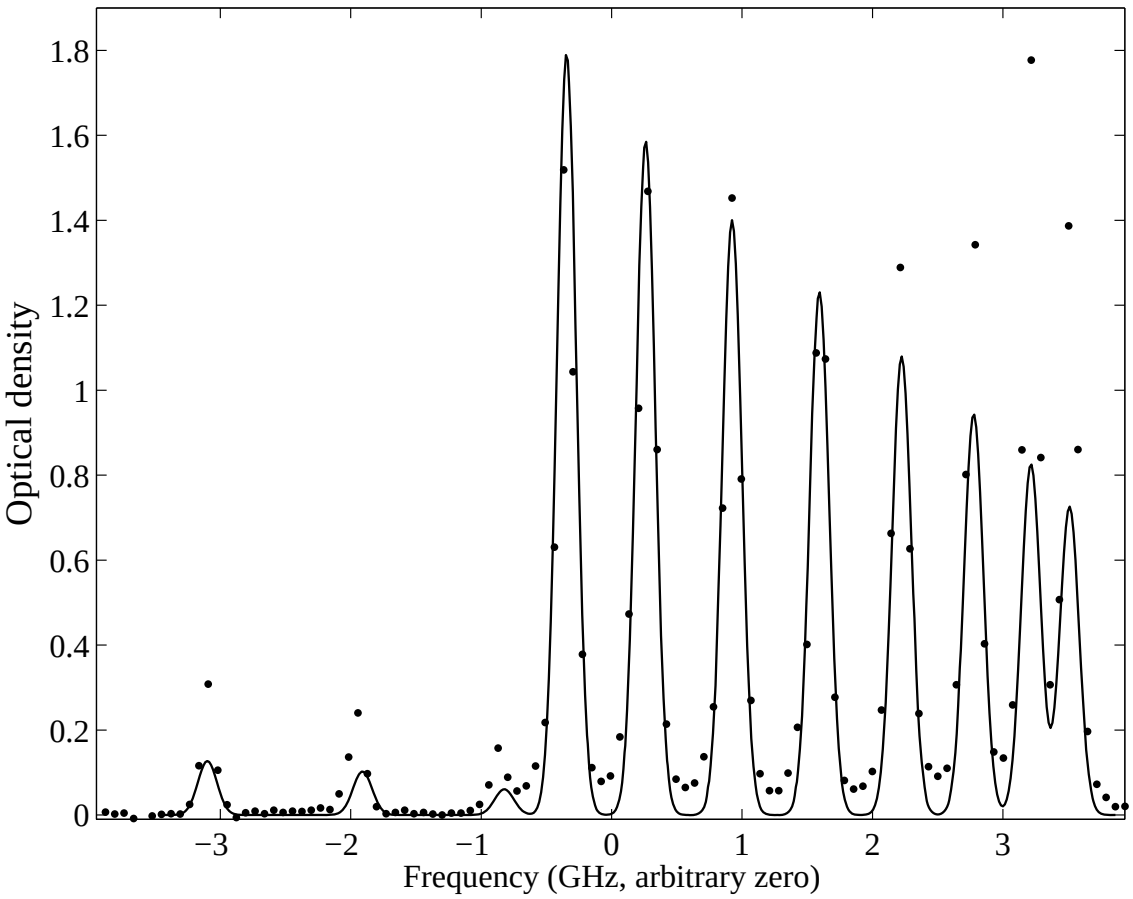

Figure 5.5: Ho zero-field spectrum for the 0 cm^{-1} $\rightarrow$ 24360.81 cm^{-1} transition at 411 nm. Ho has one stable isotope, ^{165}Ho. The ground state hyperfine constants are A=800.583645 MHz and B=-1668.00527 MHz [90]. The fit to the spectrum shown by the solid line gives values for the excited state hyperfine constants, $A' = (653 \pm 2)$ MHz and $B' = (-500 \pm 200)$ MHz. This spectrum is somewhat undersampled, resulting in a broadening of the individual absorption peaks. There are additional hyperfine peaks extending toward the red which are cut off in this spectrum.

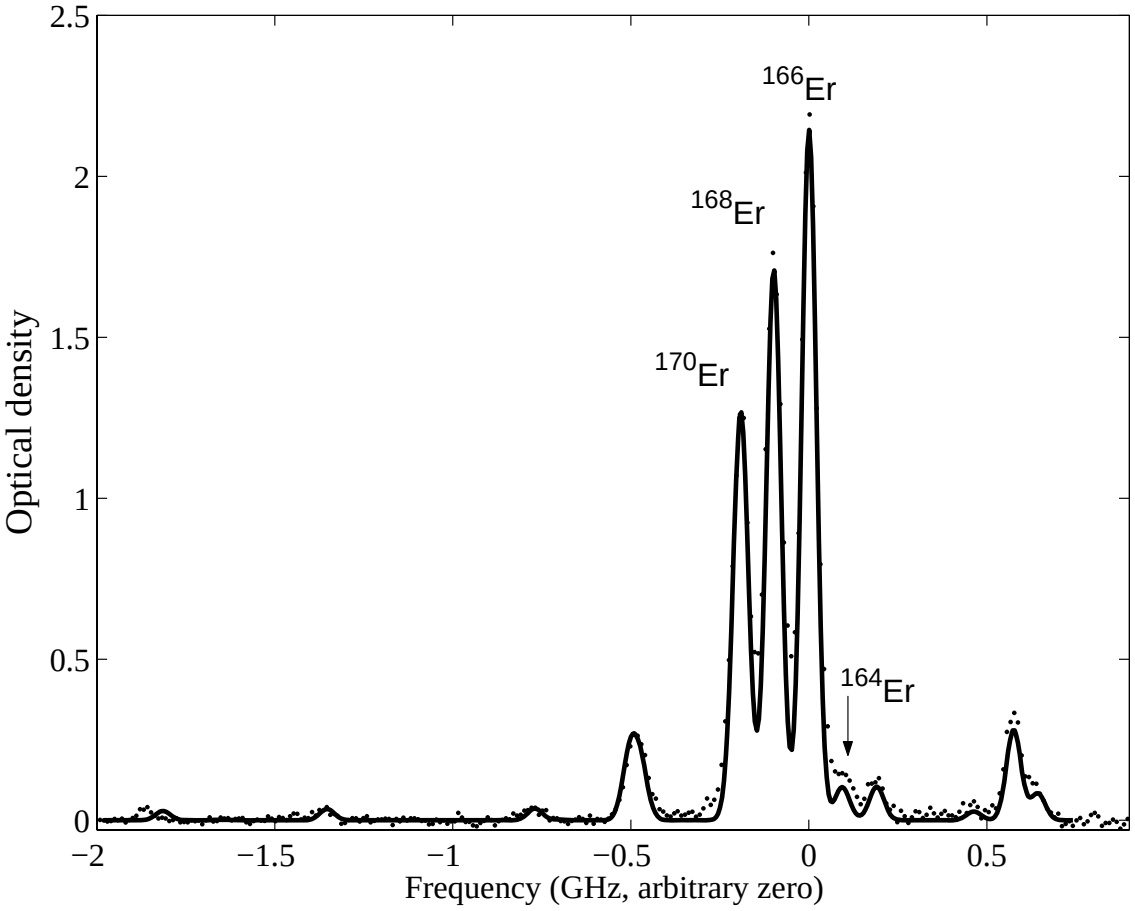

Figure 5.6: Er zero-field spectrum for the $^3H_6 \rightarrow {}^7M_5$ transition at 415 nm. Er has five stable isotopes, four with $I = 0$ (^{164}Er, ^{166}Er, ^{168}Er, ^{170}Er) and one with $I = 7/2$ (^{167}Er). The ground state hyperfine constants for ^{167}Er are known, A=-120.486 MHz and B=-4.553 GHz [91]. We fit for both the isotope shifts and ^{167}Er excited state hyperfine coupling constants; the best fit is shown by the solid line. The fit gives $A' = (-147 \pm 2)$ MHz and $B' = (-1800 \pm 200)$ MHz. The absorption peaks from those isotopes with zero nuclear spin are indicated; the remaining peaks are hyperfine lines from ^{167}Er. The measured isotope shifts are given in Table 5.2.

Table 5.2: Measured isotope shifts for Nd, Dy, and Er. Following convention, a negative sign indicates that the lighter isotope is shifted to higher frequency.

Atom	Wavelength(nm)	Isotope pair	Δf (GHz)
Nd	464	142-144	−0.31(3)
		142-146	−0.62(3)
		142-148	−0.90(3)
		142-150	−1.16(3)
Dy	421	160-164	−1.88(2)
		161-164	−1.62(2)
		162-164	−0.89(2)
		163-164	−0.61(2)
Er	415	164-166	−0.095(10)
		166-167	−0.063(20)
		166-168	−0.101(10)
		166-170	−0.193(10)

Table 5.3: Measured excited state hyperfine coupling constants for Pr, Dy, Ho and Er.

Isotope	I	Level (cm^{-1})	A (MHz)	B (MHz)
^{141}Pr	5/2	21106	845±5	0±100
^{161}Dy	5/2	23734	-87±3	1700±200
^{163}Dy	5/2	23734	122±2	1900±200
^{165}Ho	7/2	24361	653±2	-500±200
^{167}Er	7/2	24083	147±2	1800±200

5.3 Elastic collisions with He

We measure the rare earth – ^{3}He elastic collision rate by observing the diffusion of the rare-earth atoms through the buffer gas with the magnet ramped to zero current and applying Eq. (3.1). For the temperature of the gas, we use our Ti measurements from late in the run, when the ferromagnetic samples have demagnetized and a clean measurement can be made. We fit Voigt profiles to Ti spectra taken at zero field, and find $T = 1.1 \pm 0.3$ K (see Figure 5.1b for an example of one of the fits). We use the same ablation pulse energy (10 mJ) for all elastic cross-section measurements as

is used for Ti, so we assume the gas temperature will be similar atom to atom.

We find the buffer-gas density in the cell by observing the rate of diffusion of Ti atoms, whose elastic collision cross section is found in Section 3.5.2. We find a Ti diffusion time of (64 ± 4) ms, giving a buffer-gas density of $n_{\mathrm{He}} = (7.6 \pm 3.3) \times 10^{15}$ cm^{-3}. A summary of our elastic-collision cross-section measurements for the rare earths is given in Table 5.4.

Table 5.4: Measured diffusion time constants and elastic-collision cross-sections for rare-earth – ^{3}He collisions at a temperature of (1.1 ± 0.3) K.

Atom	τ_{d} (ms)	σ_{el} (10^{-14} cm^2)
Pr	58 ± 5	1.3 ± 0.6
Nd	58 ± 4	1.3 ± 0.6
Tb	83 ± 10	1.9 ± 0.9
Dy	60 ± 8	1.4 ± 0.6
Ho	60 ± 4	1.4 ± 0.6
Er	62 ± 4	1.4 ± 0.6
Tm	65 ± 5	1.5 ± 0.7

5.4 Inelastic collisions with He in the Helmholtz field

We first attempt to measure the inelastic RE-^{3}He collision rates in the Helmholtz field in the same fashion as our improved Ti measurements discussed in Section 3.5.4. We ablate the atoms into the buffer gas with a magnetic field of ∼1.1 Tesla (corresponding to 10 A in each coil) in the cell. We monitor the populations of the high-field-seeking (HFS) and low-field-seeking (LFS) states with time. While both levels should be equally populated by the ablation pulse, the LFS atoms relax over time to HFS

states due to inelastic collisions. In addition, the populations of all levels decrease with time due to diffusion.

Figure 5.7a shows the HFS ($m_J = -7/2$) and LFS ($m_J = 7/2$) population time profiles for thulium. The HFS atoms diffuse out of the cell with a time constant of 75 ms, which is slightly longer than the 65 ms timescale observed at zero field. This slight lengthening of the diffusion time is not surprising since the atoms will feel a significant force from the inhomogeneous magnetic field. What is interesting here is the LFS atom decay– the LFS atoms stick around a lot longer than had been seen for the transition metals. We observe exponential decay early on with a time constant of 21 ms, compared to the 12 ms time constant seen for Ti LFS decay at the same buffer-gas density. In addition, a significant component of this decay may be due to drift / diffusion.

Figure 5.7b shows the corresponding Zeeman temperature calculated using Eq. (3.3), along with the translational temperature measured for Ti at zero-field. (We expect the Tm translation temperature profile to be similar to that for Ti since the similar ablation pulse powers and buffer-gas densities are used.) The Tm Zeeman temperature relaxes to the translational temperature over about 50 ms.[4] The observed LFS decay over this time can be used to put an upper limit on the inelastic Tm-^{3}He collision rate coefficient, $\Gamma_{\rm in} < (\tau n_{\rm He})^{-1}$. We call this an upper limit since we are unsure of the effect of drift on the LFS diffusion time. We find $\Gamma_{\rm in} < 7 \times 10^{-15}$ cm^3 s^{-1} at a temperature of $T = 1$ K, which puts a lower limit on the ratio of elastic to inelastic collisions of $\gamma > 2 \times 10^4$.

It should be possible to get a better measurement of the inelastic collision rate by

[4]The Zeeman temperature appears to dip slightly below the translational temperature– it's possible that the translational temperatures are systematically shifted high due to pressure broadening.

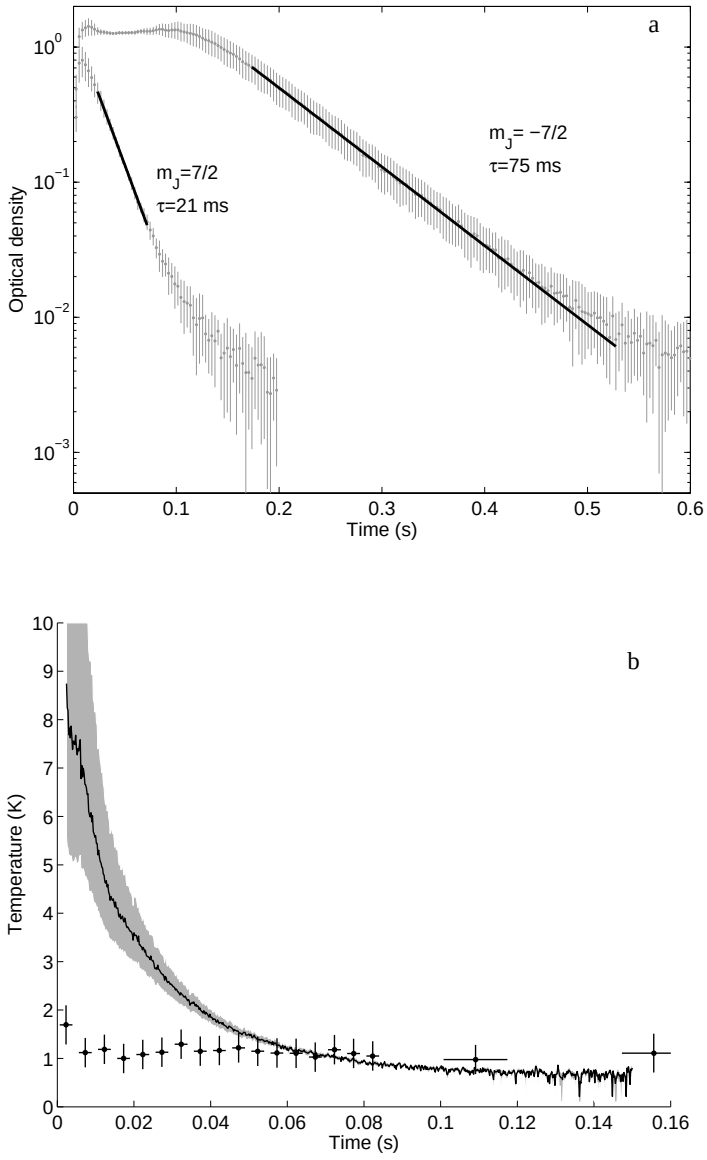

Figure 5.7: Zeeman level populations and temperature comparison for Tm atoms in a 2.2 T field. (a) Observed peak optical density (proportional to atom number) of Tm atoms in the $m_J = \pm 7/2$ levels as a function of time following a 10 mJ ablation pulse at $t = 0$. The gray vertical bars and points are the mean and standard deviation obtained by time binning the combined data from 8 profiles. One-body fits are shown by the black lines; the measured exponential decay time constants are listed. (b) Comparison of the Zeeman and translational temperatures. The Zeeman temperature (black line with error indicated by the shaded region) is calculated from the level populations using Eq. (3.3). The measured Ti translational temperature is shown by the circles, with error bars indicated by the crosses. We expect the Ti and Tm translational temperature profiles to be similar.

adding more buffer gas to the cell—a higher buffer-gas density will result in a shorter Zeeman relaxation time while lengthening the diffusion time. We find, however, that at high buffer-gas densities we get "extra light" in the signal beam following the ablation. In other words, the probe light collected in the signal PMT *increases* in intensity after the ablation. Our observations of this unexpected and unexplained phenomenon are detailed in Appendix C.

While the long LFS decay time makes it difficult to extract a precise inelastic collision rate, this is, of course, the kind of problem we like to have. The large suppression of Zeeman relaxation in Tm-^{3}He collisions means that Tm should be trappable in our cell. It turns out that the inelastic collision rates with He are even lower for the other rare-earths we studied. We now move on to discuss our efforts to magnetically trap the non-S-state rare earths.

5.5 Trapping

To look for trapping, we return the magnet to the anti-Helmholtz current geometry, which creates a spherical quadrupole trapping field with depth of up to 2.7 T for a 60 A current. For the rare-earth atoms studied, this corresponds to trap depths ranging from 4.5 to 18 K. For trapping, we expect to see low-field-seeking atoms collect near the center of the trap, and to observe low-field-seeker lifetimes significantly longer than the zero-field diffusion time. The buffer-gas density is held constant throughout the trap loading process, at $n_{\mathrm{He}} = (7.6 \pm 3.3) \times 10^{15}$ cm^{-3}.

Figure 5.8 shows early time spectra of low-field-seeking Tb atoms at a trap depth of 1.15 T obtained via absorption spectroscopy on the $J = 15/2 \rightarrow J' = 13/2$ transition at 434 nm (see Table 2.3). For this transition, the strongest absorption lines for low-field-seeking atoms are broadened to the red by the Zeeman level shifts, while

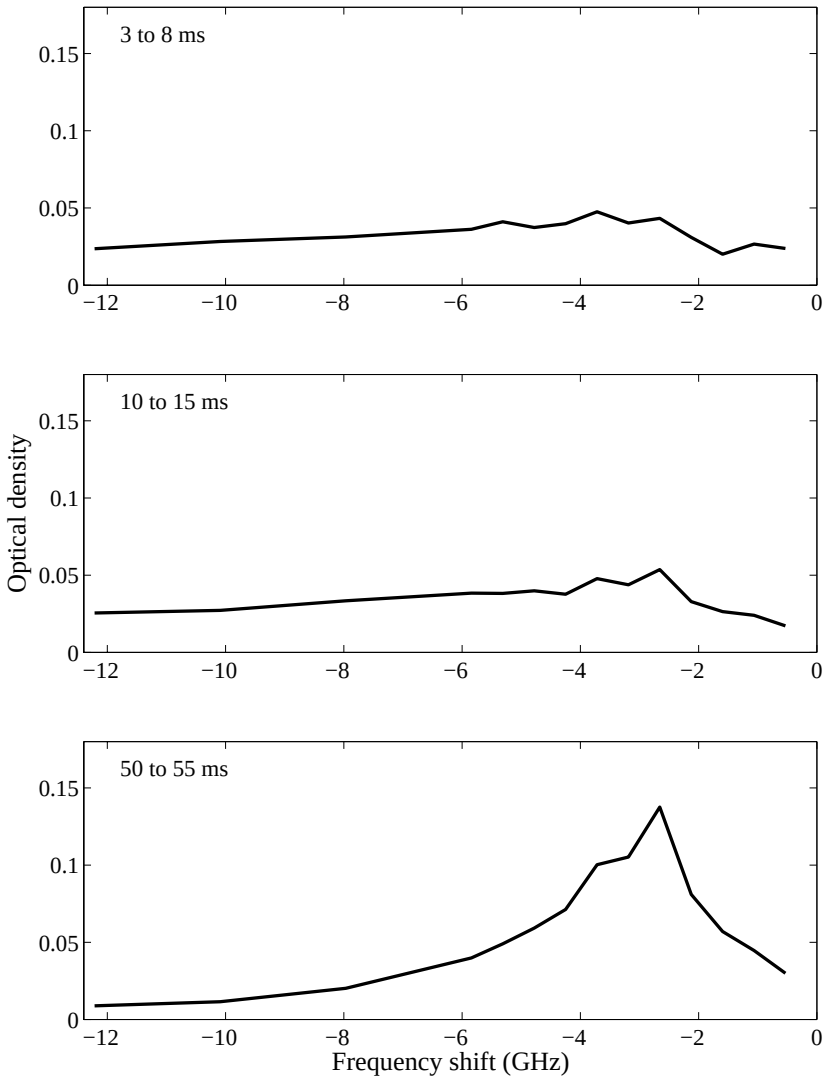

Figure 5.8: Time progression of Tb trapping. The panels show spectra of low-field-seeking Tb atoms at increasing times following the $t = 0$ ablation pulse. The frequency shift (relative to the field-free line) is proportional to the magnitude of the magnetic field. The optical density at a given frequency shift is proportional to the number of atoms at the corresponding field. The atoms fall towards low field over about ∼50 ms. The trap depth is 1.15 T, corresponding to a depth of 7.7 K for the $m_J = 7/2$ Zeeman level.

high-field-seeking lines are broadened to the blue of the field-free line. The figure shows the low-field-seeking portion of the spectrum for several times following the ablation pulse. As the Zeeman level shifts are linear with the magnitude of the applied magnetic field, the frequency shift is proportional to the magnetic field. The optical density at a given frequency shift is proportional to the number of atoms at the corresponding magnetic field strength. The peak near zero frequency shift builds with time, reflecting the movement of low-field-seeking atoms to the lower fields at the center of the trap. This initial "falling in" is complete by ~ 50 ms after ablation.

The spectrum shown in the final panel reflects a thermal distribution of trapped Tb atoms which may be fit for the number of atoms and the temperature of the gas.[5] A number of Zeeman levels are trapped at this field value, so this spectrum likely has contributions from multiple levels, not just the $m_J = J$ state. Less strongly trapped atoms will extend farther out spatially, and so will give a broader absorption line. If the populations in these other levels aren't accounted for and only the $m_J = J$ state is assumed, the temperature fit will be artificially high. To get some handle on the relative contributions from less trapped Zeeman levels, we model the time evolution of the Zeeman level populations under the influence of drift, diffusion, and inelastic collisions. In addition, the model enables us to fit the observed loss from the trap and obtain the rate constant for inelastic collisions with helium.

5.5.1 Trap loss model

The level of confinement for a particular Zeeman level is characterized by the parameter η, which is the ratio of the trap depth to the translational temperature of the gas, $\eta = g_J m_J \mu_B B_t/(kT)$, where B_t is the field magnitude at the edge of the trap.

[5]See Reference [56] for a thorough discussion of the spectrum fitting model used

Figure 5.9, taken from Reference [56], shows the trap lifetime as a function of η in the absence of inelastic collisions.[6] The lifetime increases steeply with η, and for $\eta > 7$ is enhanced by more than a factor of 10 over the zero-field diffusion time. For Tb atoms at a trap depth of 1.1 T and a temperature of 1 K, $\eta = 7.7$, 6.7, and 5.6 for the first three Zeeman levels, m_J =15/2, 13/2, and 11/2, respectively. With a measured zero-field diffusion time of 83 ms, we expect each of these levels to have a significant contribution to the $t = 50$ ms spectrum shown in Figure 5.8.

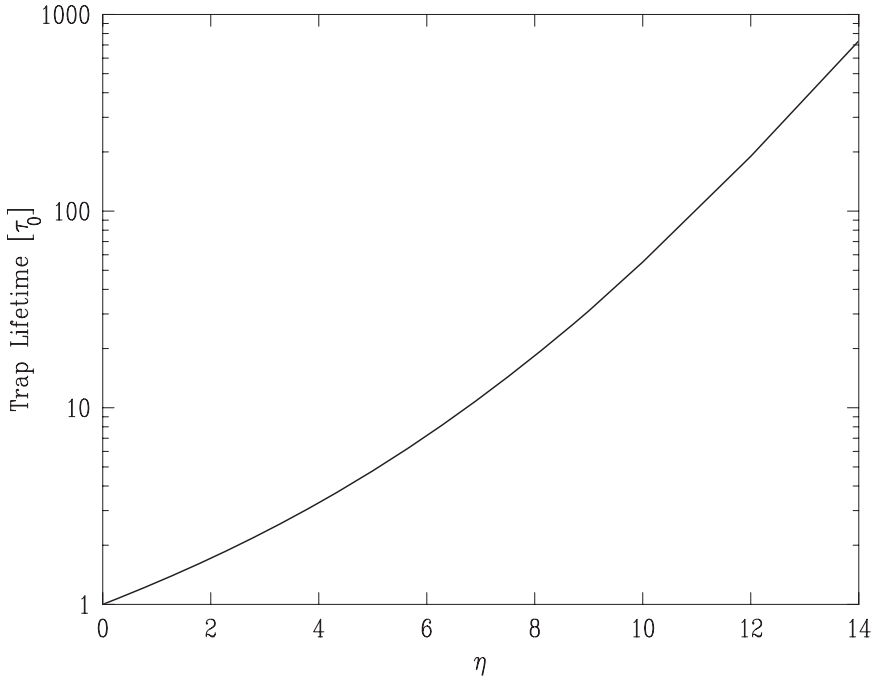

Figure 5.9: The trap lifetime $\tau(\eta)$ in the short-mean-free-path regime as calculated analytically for a spherically symmetric, linear trap in the absence of inelastic collisions. The lifetime is expressed in units of τ_0, the zero-field diffusion time. Taken from Reference [56].

In addition to the enhancement of the low-field-seeker lifetimes due to trapping, these atoms will also suffer depletion from Zeeman relaxation. To model the time

[6]The analytical model used assumes a linear, spherically symmetric trap with spherical cell walls. Numerical simulations using the real spherical quadrupole field and cylindrical cell geometry agree to within 20%, see Reference [56].

evolution of the level populations, we consider that atoms may move back and forth between levels due to inelastic collisions as done in Section 3.2. We also include loss due to drift/diffusion. For the inelastic collisions, we again assume that atoms are equally likely to be transferred to any level that is energetically allowed in the collision, and that the inelastic collision rate coefficient is $\Gamma_{\rm in}/(2J)$ for such a transition. We choose the denominator, $2J$, so that the total inelastic rate constant for the $m_J = J$ state is $\Gamma_{\rm in}$. We therefore have that an atom in an arbitrary Zeeman level $|m\rangle$ is free to move to a lower energy state during an inelastic collision, however promotion to a higher lying Zeeman level $|m'\rangle$ with $m' > m$ will be suppressed by a factor $\exp\left(-g_J\mu_{\rm B}(m'-m)B/kT_{\rm trans}\right)$, where $T_{\rm trans}$ is the translational temperature of the gas. The rate of change of the density of atoms in state $|m\rangle$ sitting in a field B is then

$$\begin{aligned}\dot{n}_m &= -\frac{\Gamma_{\rm in} n_{\rm He} n_m}{2J}\left[\sum_{m'>m} 1 + \sum_{m'>m} \exp\left(-\frac{g_J\mu_{\rm B}(m'-m)B}{kT_{\rm trans}}\right)\right] \\ &\quad + \frac{\Gamma_{\rm in} n_{\rm He}}{2J}\left[\sum_{m'>m} n_{m'} + \sum_{m'<m}\left(n_{m'}\exp\left(-\frac{g_J\mu_{\rm B}(m-m')B}{kT_{\rm trans}}\right)\right)\right] \\ &\quad - \Gamma_{\rm d} n_m, \end{aligned} \tag{5.1}$$

where $\Gamma_{\rm d} = \Gamma_{\rm d}(\eta)$ is the drift/diffusion rate, given by $\Gamma_{\rm d} = 1/\tau$, with τ found from Figure 5.9.

5.5.2 Trapping results

We determine the inelastic RE-^{3}He collision rates by fitting the observed decay of low-field-seekers from the trap. Figure 5.10 shows the measured Tb low-field-seeker peak optical density (proportional to the number of atoms) for a 1.15 T trap depth, along with the simulation of the low-field-seeker level populations from Eq. (5.1). The observed optical density increases for the first 50 ms, during which the low-field-

seeking atoms collect at low-field. The optical density then decreases exponentially, indicating one-body decay through diffusion and/or inelastic collisions with the buffer-gas. For the simulation, the level populations are set to be equal at $t = 0$, and then allowed to evolve under inelastic collisions and trap loss. The collection period is not included in the model. The level population proportions reach a steady value after about 100 ms, after which all levels decay at about the same rate. We tune Γ_{in} in the simulation so that this decay time matches the observed one-body decay. For Tb, the observed time constant for exponential decay is 107 ms, and for the simulation this requires an inelastic Tb-^{3}He collision rate constant of 1.5×10^{-15} cm^3 s^{-1}.

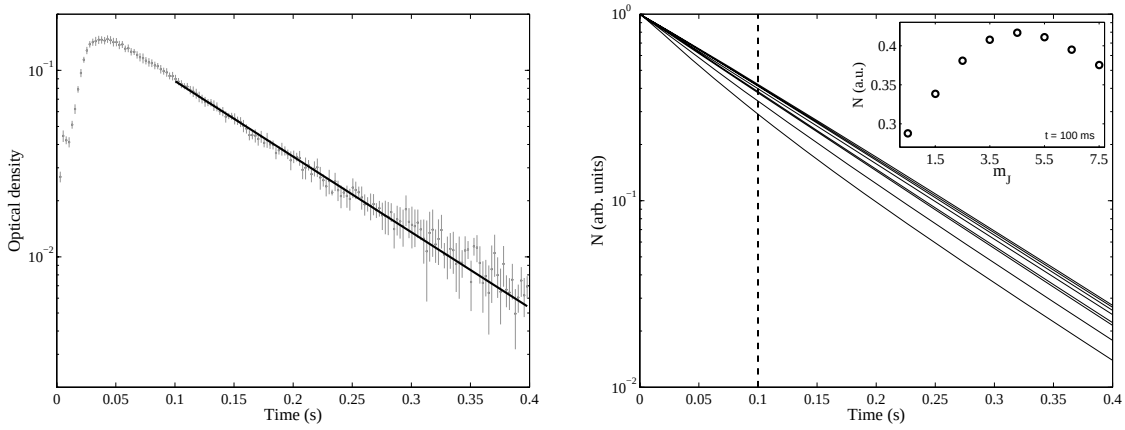

(a) Observed (b) Simulation

Figure 5.10: Decay of Tb low-field-seekers from the magnetic trap. (a) Observed peak optical density (proportional to atom number) following the $t = 0$ ablation pulse. A fit to exponential decay gives a time constant of 107 ± 10 ms. (b) Simulation of low-field-seeker level populations using Eq. (5.1). The inset shows the relative populations in the various low-field-seeking Zeeman levels at $t = 100$ ms.

The relative level populations found in the simulation are used in fitting the trapped spectra for number and temperature. For Tb, all low-field-seeking levels provide a significant contribution to the spectrum. This is not surprising since the

trap lifetime of 107 ms is only slightly longer than the zero-field diffusion time of 83 ms. A Tb spectrum taken 100 ms after the ablation is shown in Figure 5.11. We find that 7×10^{10} atoms are trapped at a temperature of 0.8 K.

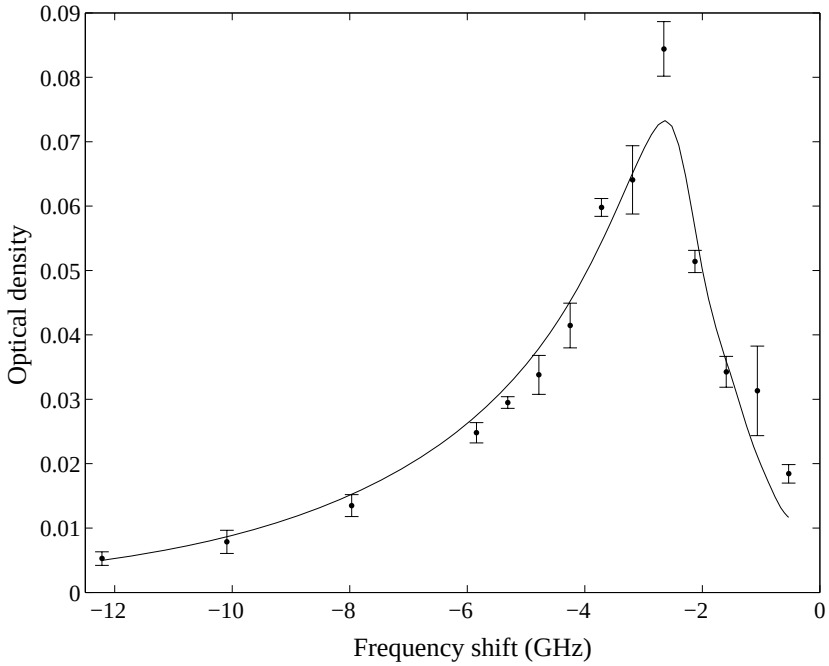

Figure 5.11: Tb trapped spectrum. Solid curve is a simulation of a trapped thermal distribution with 10^{11} atoms trapped at a temperature of 0.8 K.

In addition to Tb, spectra and trap decay measurements are taken for Pr, Nd, Dy, Ho, Er, and Tm. A summary of our results is presented in Table 5.5; individual spectra are presented in Appendix B. We find that for each species, $(0.2 - 2) \times 10^{12}$ rare-earth atoms are trapped at densities of $(0.2 - 8) \times 10^{12}$ cm^{-3} and temperatures of $\sim$800 mK. Inelastic collisions with helium are strongly suppressed for all the atoms studied, and interestingly, the suppression appears to increase with increasing L. The ratio of elastic to inelastic collisions, γ, ranges from 30,000 to upwards of 500,000 for Dy. Figure 5.12 shows a spectrum taken of trapped Dy atoms a full second after the ablation pulse, showing 3×10^{10} atoms remaining. Note that the temperature has

Table 5.5: Summary of rare-earth trapping and collision rate results for collisions with ^{3}He. Atoms are arranged according to term. Inelastic collision rate data taken at $T = 0.8$ K.

Atom	Term	μ/μ_B	Number trapped	$\Gamma_{in}(\text{cm}^3\ \text{s}^{-1})$	$\gamma \equiv \sigma_{el}/\sigma_{in}$
Tm	$^2F_{7/2}$	3.99	2×10^{11}	$(5.0 \pm 2.1) \times 10^{-15}$	$(2.7 \pm 1.4) \times 10^4$
Er	$^3H_6$	6.98	2×10^{11}	$(3.0 \pm 1.3) \times 10^{-15}$	$(4.3 \pm 2.3) \times 10^4$
Nd	$^5I_4$	2.41	1×10^{12}	$(1.4 \pm 0.7) \times 10^{-15}$	$(8.7 \pm 4.9) \times 10^4$
Tb	$^6H_{13/2}$	9.94	2×10^{11}	$(1.5 \pm 0.6) \times 10^{-15}$	$(1.2 \pm 0.6) \times 10^5$
Pr	$^4I_{9/2}$	3.29	3×10^{11}	$(9.1 \pm 4.3) \times 10^{-16}$	$(1.3 \pm 0.8) \times 10^5$
Ho	$^4I_{15/2}$	8.96	9×10^{11}	$(4.5 \pm 2.1) \times 10^{-16}$	$(2.8 \pm 1.6) \times 10^5$
Dy	$^5I_8$	9.93	2×10^{12}	$(2.8 \pm 1.1) \times 10^{-16}$	$(4.5 \pm 2.4) \times 10^5$

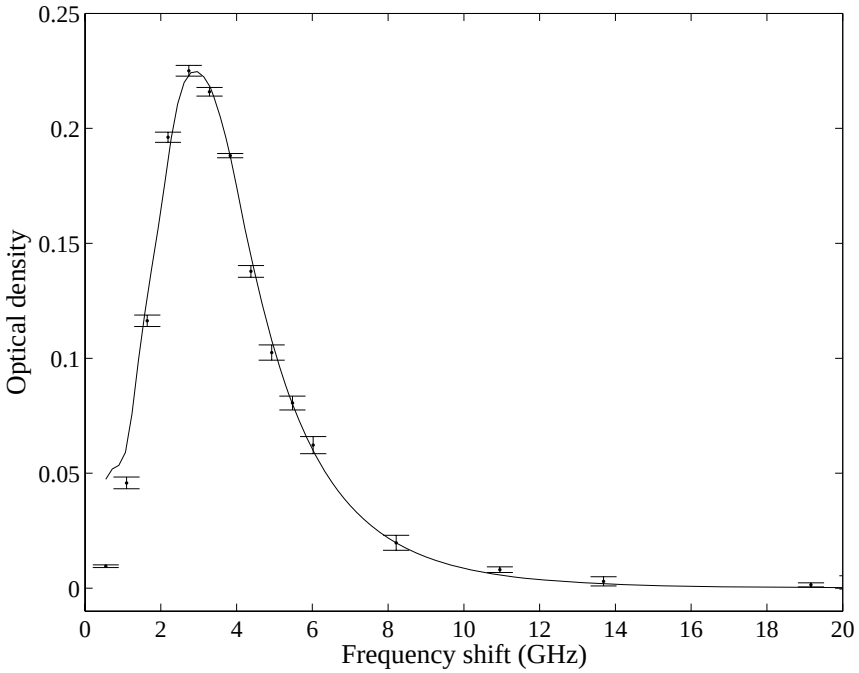

Figure 5.12: Dy trapped spectrum, taken 1 s after the ablation. Solid curve is a simulation of a trapped thermal distribution with 3×10^{10} Dy atoms trapped at a temperature of 0.5 K.

fallen during this time to 0.5 K due to the post-ablation cell cooling.[7]

[7]For these measurements, constant heating is applied to the cell to ensure that the buffer-gas density remains constant and the helium doesn't liquefy. The heating is such that the cell temperature cannot fall below 350 mK.

Following trapping, the next step is to thermally isolate the trapped atoms by removing the buffer gas. With the current apparatus, our only option for this is to cryopump the buffer gas by cooling the cell and allowing the He to liquefy onto the cell walls. Given that it takes of order 1 s to cool the cell, this method is feasible for isolating the longest-lived species, Dy and Ho.

5.5.3 Thermal isolation

Here we use a ^{4}He buffer gas to more easily achieve good vacuum after trapping. We use the cell temperature to control the buffer-gas density in the cell, taking advantage of the steep dependence of the He saturated vapor pressure on temperature in this temperature regime to swing the density over several orders of magnitude (see Figure 5.13). We heat the cell just prior to loading so that the buffer-gas density is

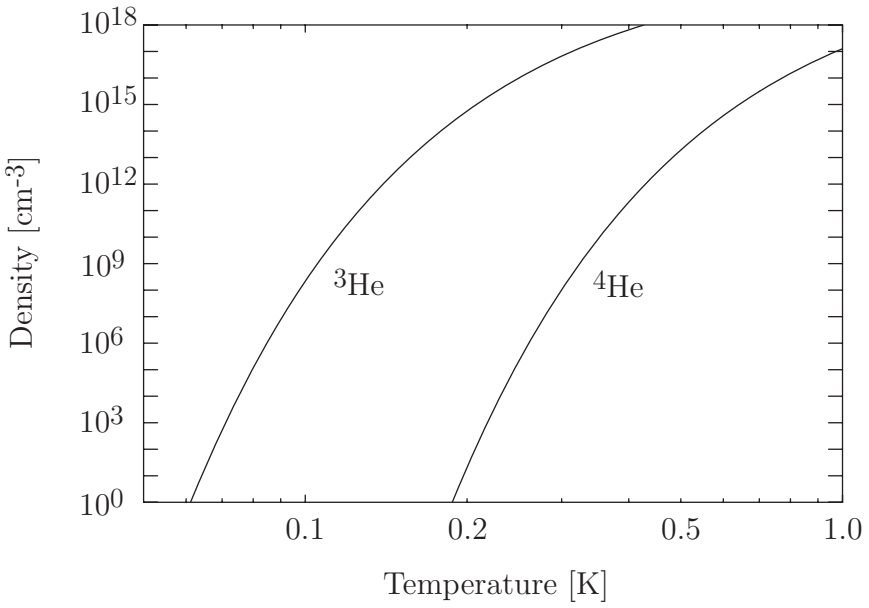

Figure 5.13: Equilibrium vapor density for ^{3}He and ^{4}He as a function of temperature. Taken from Reference [56].

$\sim 10^{16}$ cm^{-3}. We require that the density be high so that that hot atoms coming

off the ablation site thermalize with the buffer gas before reaching the cell walls. We cool the cell immediately following the ablation to reduce the helium density and break thermal contact between the trapped atoms and the cell walls. The resulting spectrum for Dy taken from 3.5 to 5.5 s after the ablation is shown in Figure 5.14. A fit of the spectrum indicates that 10^{11} Dy atoms are trapped at a temperature of 0.6 K. Figure 5.15 shows a spectrum of trapped Ho atoms following the buffer-gas removal. We are unable to fit for number and temperature here since the excited state g-factor is unknown.

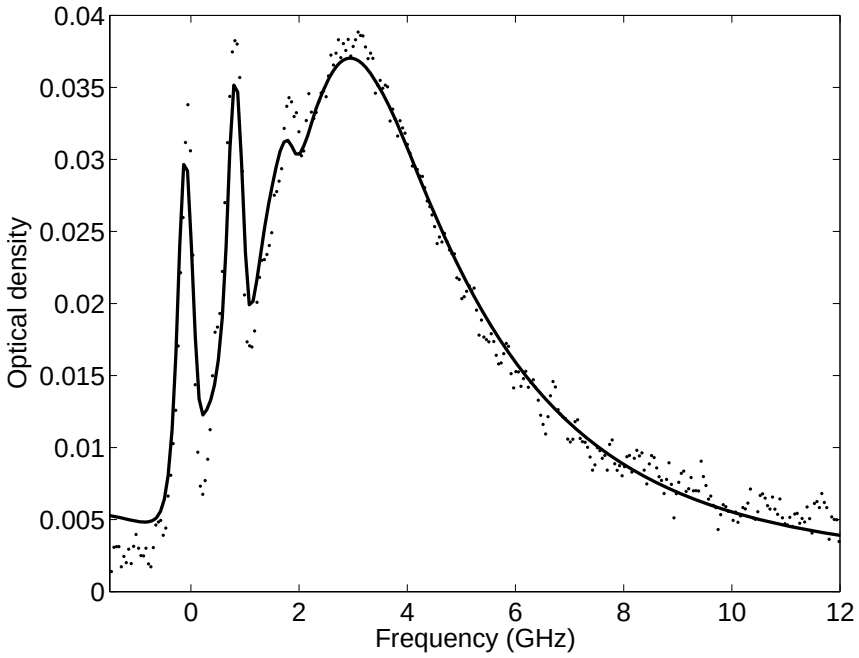

Figure 5.14: Trapped Dy spectrum following the removal of the ^{4}He buffer gas. The solid curve is a simulation of a trapped thermal distribution with 10^{11} Dy atoms trapped at a temperature of 600 mK.

As described in Reference [92], it is possible to remove the buffer gas on a much faster (50 ms) timescale by pumping the helium out of the cell through a large-aperture cryogenic valve. This timescale is shorter than all the trap lifetimes we observe, indicating that thermal isolation of each trapped rare-earth element would

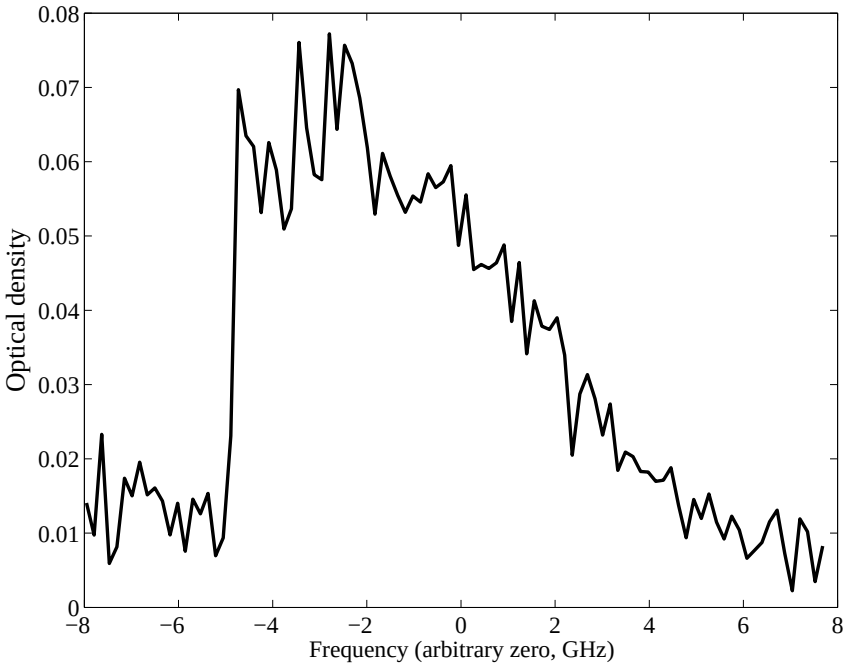

Figure 5.15: Trapped Ho spectrum following the removal of the ^{4}He buffer gas.

be made straightforward by incorporating such a valve into our apparatus.

Chapter 6

Molybdenum

Prior to our work with non-S-state atoms, we worked on the trapping and evaporative cooling of S-state transition metal atom molybdenum. Molybdenum is interesting since it is highly magnetic ($\mu = 6\ \mu_{\mathrm{B}}$) and has both bosonic and fermionic isotopes. Its large magnetic moment makes it straightforward to buffer-gas load into a magnetic trap and to achieve ample trap lifetimes for removing the buffer gas for thermal disconnect and subsequent evaporative cooling. Mo also provides an interesting comparison to atomic chromium, which has been previously studied in this lab.

6.1 Apparatus

The experimental apparatus is nearly identical to that used previously to evaporatively cool atomic Cr, and is described in detail in Reference [56]. Here we provide a brief review. Mo atoms are produced by laser ablation of a metal target inside a cylindrical double-walled plastic cell cooled by a dilution refrigerator (Figure 6.1). The jacket formed by the concentric cell walls is filled with superfluid ^{4}He that provides a

thermal link between the cell and the mixing chamber of the refrigerator. This type of heat link is advantageous since superfluid He has a high thermal conductivity at low temperatures [93] but is also electrically insulating. This enables us to ramp the magnetic field rapidly without undue heating from induced eddy currents.

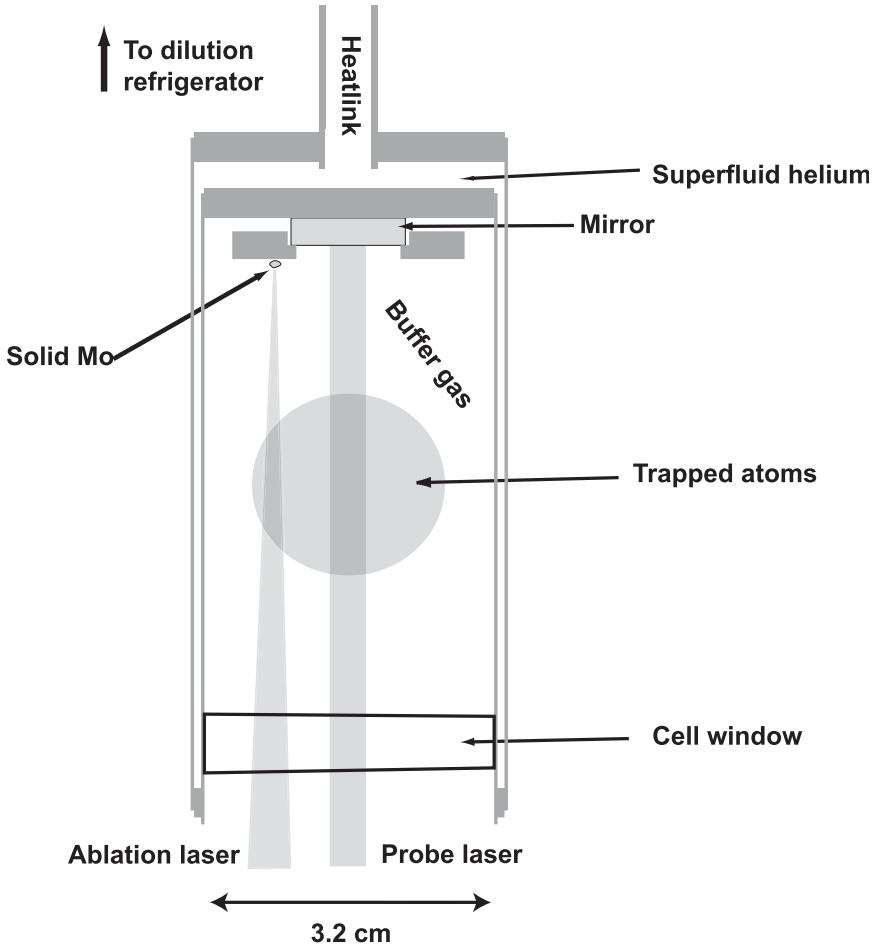

Figure 6.1: The experimental plastic cell.

The interior of the cell is filled with a fixed amount of ^{4}He which serves as the buffer gas. The density of buffer gas in the cell is set by the vapor pressure of ^{4}He and can be varied from $< 10^{12}$ to 10^{17} cm^{-3} by heating the cell from 0.2 to 1 K.

The molybdenum atoms are produced via laser ablation of a metal target that is mounted near the top of the cell. The target is a piece of natural isotopic abundance

molybdenum metal [94]. The target is ablated with a 15 mJ, 5 ns pulse from a frequency-doubled (532 nm) Nd:YAG laser [59].

6.1.1 Magnet trouble

Surrounding the cell is a superconducting anti-Helmholtz magnet which creates a spherical quadrupole trapping field.[1] After the experiment was cooled down, we found that there was a short between the magnet coils and the dewar. The short was probably due to inadequate electrical insulation around the magnet leads[2]—one of the leads likely made contact with either the magnet cask or the inner dewar walls when the dewar was raised. We did not check for a short at any time until the experiment was cooled, so we cannot tell whether the short only developed during the cooldown.

We connected the shorted lead to the negative terminal of the magnet power supply. We ramped the magnet first to 10 A and then 20 A without incident. We then attempted to ramp it to 60 A (the current at which we planned load Mo atoms into the trap), but the magnet quenched on the way, at ∼55 A. The maximum current for the magnet was previously found to be 78 A [56]. This premature quenching probably comes as a result of heating at the short site, which drives a portion of the superconducting lead normal and triggers the quench. This theory is consistent with an increase in the helium boiloff from the cryostat that we observe when the magnet is powered.

We decided to limit the maximum current used to 40 A, corresponding to a trap

[1]The design of this magnet is described in Reference [56], where it is referred to as "the new magnet."

[2]Mylar tape served as the sole insulation for a portion of the leads. It is possible that the tape came off or that one of the lead lugs broke through as we were raising the dewar.

depth of 7.2 K (2.3 T). While it's possible that we could have gotten away with a slightly higher current, we were worried that if the magnet were held at an elevated current for an extended period of time, the heating would cause the magnet to quench even at currents somewhat less than observed quench current of 55 A.

6.2 Loading procedure

The loading procedure begins with a deep (7.2 K, 2.3 T) magnetic trap. The cell is heated to create a high density of buffer gas (10^{17} cm^{-3}) before firing the ablation pulse. Roughly 10^{12} molybdenum atoms are produced in the ablation. The Mo atoms quickly (few milliseconds) thermalize with the buffer gas, and the low-field-seeking Mo atoms fall into the magnetic trap. The high-field-seeking atoms are driven to the walls, where they stick. The cell is cooled to below 0.2 K within 10 s, causing the buffer gas to liquefy onto the cell walls, and leaving a magnetically trapped, thermally isolated sample of Mo atoms. At this point, the trap depth may be reduced to force evaporative cooling.

6.3 Detection

Molybdenum atoms are detected via laser absorption spectroscopy on the $a\ ^7S_3 \rightarrow z\ ^7P_2$ transition at 390 nm [39]. The optics chain used for detection is schematically the same as for the non-S-state atom experiments (Figure 2.3).

The probe light is produced using a grating-tuned diode laser.[3] Probe powers of $\sim$100 nW and a beam diameter of $\sim$2 mm are used. The probe power is chosen so that it is as high as possible (to limit the affect of shot noise) without affecting the

[3]This is the same diode laser [69] used for Sc detection; see Section 2.2.3.

loss rate or temperature of the trapped atoms.

The probe light is directed to an optical breadboard mounted on the bottom of the cryostat, where it is split into "signal" and "reference" legs. The reference beam passes directly through the beamsplitter to a PMT. The reference beam is used to divide out fluctuations in laser intensity. The signal beam passes through a series of cryostat windows (see Figure 2.3) before entering the cell. Wedged windows (2 degree wedge) are used for the cryostat [95] and cell [96] windows to prevent etaloning within each optic. Additionally, the cryostat windows are placed at askew angles ($\sim$1 degree from horizontal) to prevent intra-window etalons. The probe beam enters the cell axially and retroreflects from a 1" mirror [97] mounted at the top of the cell. It exits the cell and cryostat and is detected by a second PMT.

Each PMT outputs a current (few μA) proportional to the intensity of light collected. The current is converted to voltage using a large (10 kΩ) resistor. The voltage drop across the resistor is amplified [98] and digitized. Voltage offsets are used to zero out background room light. The recorded signal and reference voltages are therefore directly proportional to the laser light received at each PMT.

6.3.1 Etaloning in the cell mirror

The molybdenum measurements presented here "piggybacked" on an experiment whose main goal was to evaporatively cool atomic chromium [70]. The cell described above contained both Cr and Mo ablation targets, and the Cr and Mo measurements were taken during the same cooldown period. One of the goals for the Cr experiment was to attempt laser cooling in the magnetic trap (see Reference [70] for details). The laser cooling was to be performed after the buffer-gas had been cryopumped to the cell walls and after a stage of forced-evaporation via a reduction of the trap depth.

A major concern for this scheme was that the optical pumping beam might create a hot-spot at the cell mirror where the ^{4}He film would desorb, ruining the vacuum in the cell.

To minimize the heating and its effects on the cell vacuum, we took two precautions with the mirror. The first was to use a mirror with a very high reflectivity (>99.95%). To achieve this, we used a specialty dielectric coating on a fused-silica window [97]. This posed a potential problem for the Mo measurements since the coating was rather narrow-band and was optimized for the Cr transition at 427 nm rather than the Mo transition at 390 nm. According to the nominal reflectivity curves supplied by the manufacturer, the reflectivity dives off right around 390 nm. The measured reflectivity at 390 nm turned out to be ∼90% in room temperature tests of the cell mirror, which is plenty good for Mo absorption measurements. The second was to place the mirror "upside-down" in the cell so that the signal beam reflected off of the back surface. This was done so that if He desorbed due to heating from absorbed probe light, the gas would bounce around at the top of the cell and likely re-adsorb onto the cell walls before it could interact with the trapped atoms.

Much to our chagrin, using the back of the mirror as the reflection surface introduced etaloning in the probe beam.[4] Figure 6.2 shows an example of the etaloning seen. For the vertical axis, we divide the signal voltage by the reference to get rid of any dependence of the laser intensity on frequency. The curve shown is from a baseline measurement taken when there are no molybdenum atoms in the cell. The variation in signal intensity is due solely to etaloning in the cell mirror. This behavior is modeled in most optics textbooks. From Siegman's *Lasers* [99] for light incident

[4]Adding insult to injury, placing the mirror upside-down did not prevent problematic heating from the probe beam.

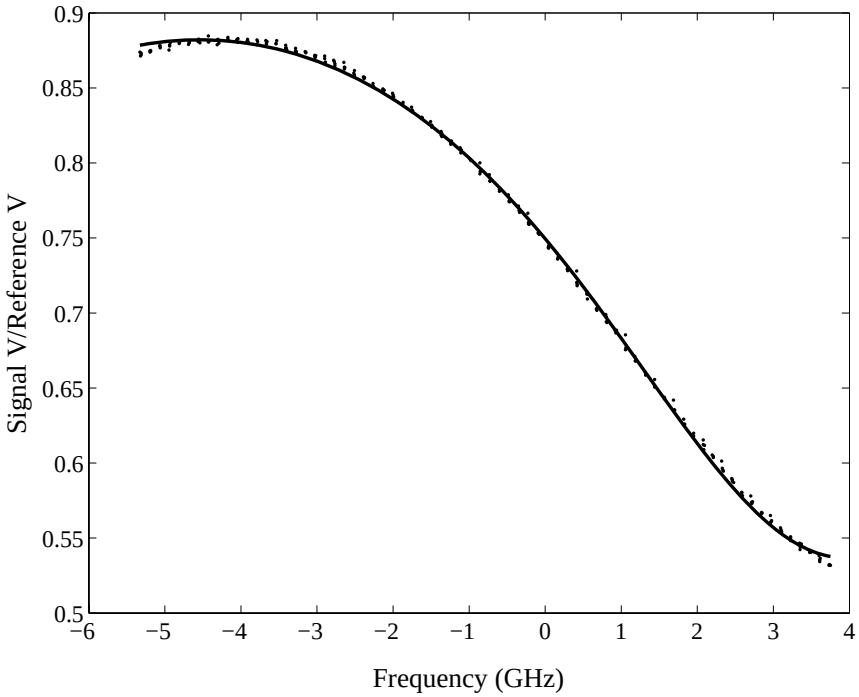

Figure 6.2: Etaloning of the probe beam due to the upside-down cell mirror. The data are shown by the dots. The solid line is a fit using Eq. 6.2.

on a cavity,

$$\frac{E_{\text{refl}}}{E_{\text{inc}}} = \sqrt{R_1} - \frac{(1 - A_1 - R_1)\sqrt{R_2}\exp(-2\alpha n L - 4i\pi f n L/c)}{1 - \sqrt{R_1 R_2}\exp(-2\alpha n L - 4i\pi f n L/c)}, \tag{6.1}$$

where E_{refl} is the total reflected field amplitude, E_{inc} is the incident field amplitude, R_1 and A_1 are the reflectivity and absorptance of the front surface of the cavity, R_2 is the reflectivity of the back surface, n is the index of refraction inside the cavity, L is the length of the cavity, α is the voltage absorption coefficient of the cavity medium (*i.e.* the roundtrip power reduction is $e^{-4\alpha L}$), f is the laser frequency and c is the speed of light. The ratio of signal to reference voltages is

$$\frac{\text{Signal V}}{\text{Reference V}} = g\left|\frac{E_{\text{refl}}}{E_{\text{inc}}}\right|^2, \tag{6.2}$$

where g is a numerical factor associated with the relative gains of the reference and signal PMTs and amplifiers, relative losses in the two optical paths, etc. For our cell

mirror, $L = 6$ mm. We assume that there are no losses in the fused-silica mirror substrate ($\alpha = 0$). We also assume zero absorptive loss at the front surface of the mirror since it is uncoated ($A_1 = 0$). We use $n = 1.47$, which is the index of refraction of fused-silica at 400 nm [100]. Figure 6.2 shows a fit of the observed etalon curve using Eq. 6.2 and allowing only parameters g, R_1, R_2 to vary. We also allow for an arbitrary offset of the laser frequency, f_0. The simulated curve agrees well with the data, and finds $R_1 = 0.05$ and $R_2 = 0.6$. The reflectivity at the front surface, R_1, is about what we would expect for an uncoated optic. The reflectivity of the back surface is lower than expected from our room temperature measurements. The reflectivity of the mirror is a steep function of frequency at 390 nm since it is near a node of the reflectivity curve. It's possible that the node position shifted slightly during the cooldown and resulted in a lower reflectivity at the probe wavelength.

If uncorrected for, the etaloning would appear as a 40% change in the absorption during the course of each frequency sweep. This is, of course, unacceptable. We attempt to correct for the etaloning by subtracting off a baseline spectrum measured with no atoms present. A baseline measurement is taken immediately before or after every absorption measurement. The subtraction is not perfect, however, due to jitter in the laser frequency. Any frequency jitter appears as noise on our absorption signal, limiting the sensitivity of our absorption measurements in this data run. Figure 6.3 shows an example of a measured Mo spectrum. For these data, the atoms are loaded at a trap depth of 7.2 K (2.3 T) and subsequently evaporatively cooled by reducing the trap depth to 0.9 K (0.3 T). This absorption is measured 50-55 s after the ablation pulse; the spectrum shown includes the baseline subtraction. There appears to be an absorption peak at the center of the spectrum, however the spectrum is quite noisy,

with the noise amplitude at about 0.2% absorption.[5] To improve the signal-to-noise, we would like to average data taken over multiple ablation pulses. Laser drift poses a potential problem, as discussed in the next section.

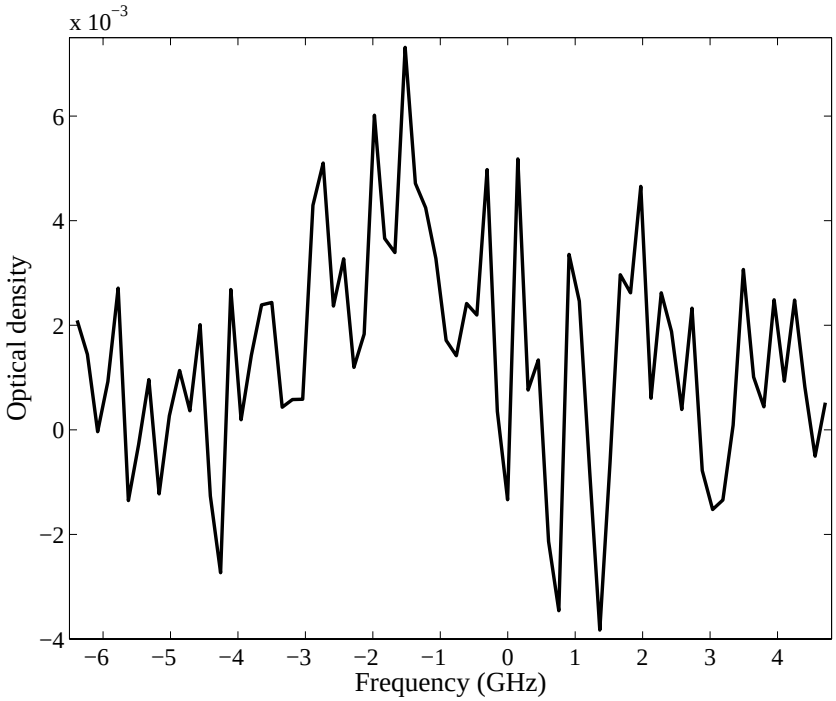

Figure 6.3: Molybdenum spectrum for a trap depth of 0.9 K (0.3 T). The noise seen is largely due to laser jitter which maps onto the absorption signal from the resulting error in the baseline subtraction.

6.3.2 Laser drift and spectrum averaging

We find that the diode laser used for Mo detection drifts hundreds of MHz in the course of an hour. The laser drift is monitored by observing the drift in the cell mirror reflectivity. Figure 6.4 shows the observed drift in the etalon curve for a series of measurements taken over a few hours. This drift is corrected for by shifting the

[5]Optical density $\approx$ absorption for values $\ll 1$.

individual spectra by the measured offset before averaging them together. Figure 6.5 shows the spectrum obtained from averaging 20 data sets, with each one taken in the same manner as the spectrum shown in Figure 6.3. The data set used for the latter figure is included in the average and is typical of the quality of the individual spectra. The noise in the averaged spectrum is sufficiently reduced that we are able to make out absorption peaks from multiple isotopes. This spectrum is discussed further in Section 6.6.

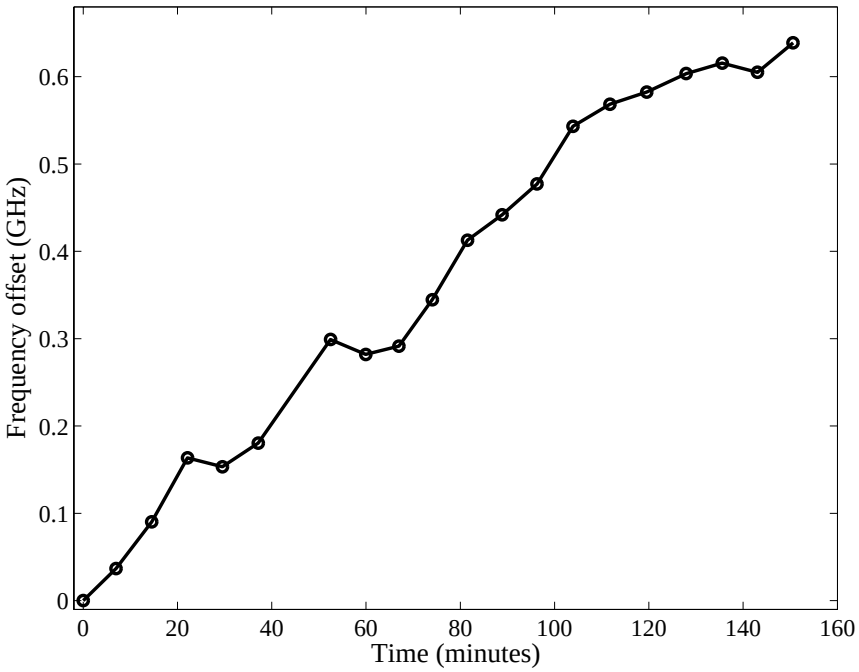

Figure 6.4: Drift in the diode laser frequency as measured by the frequency offset of the cell-mirror etalon curve. The laser is seen to drive hundreds of MHz over the course of an hour.

6.4 Molybdenum spectroscopy

Molybdenum has seven naturally occurring isotopes, all of which provide significant contributions to the absorption spectrum. The natural abundance, nuclear spin and

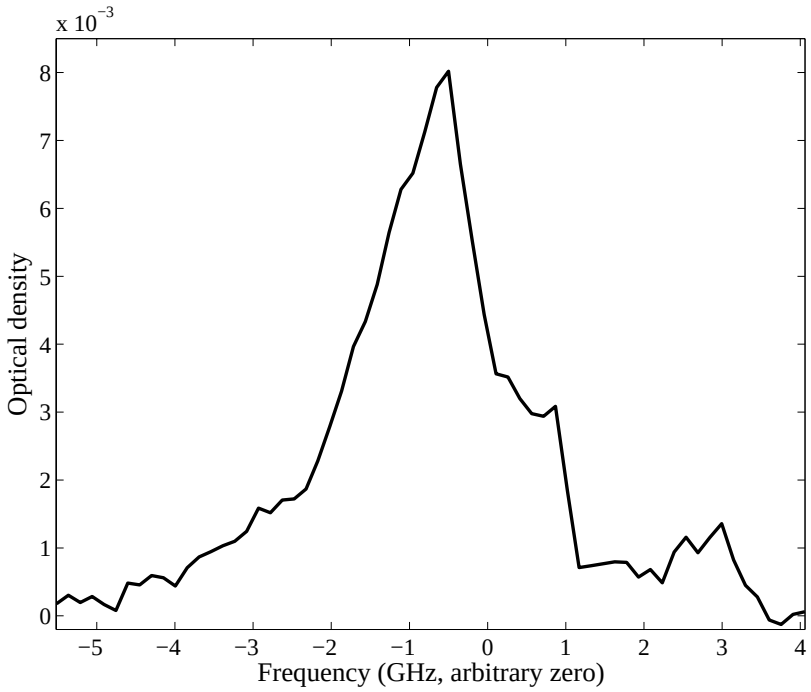

Figure 6.5: Spectrum of trapped Mo atoms for a trap depth of 0.9 K (0.3 T), averaged over 20 data sets.

isotope shift for each isotope are given in Table 6.1. All isotopes are included when modeling the trapped spectra. We fix the relative peak positions and heights using the isotope shifts and natural abundances listed. The model for simulating the trapped spectra is detailed in Reference [56].

Table 6.1: Stable isotopes of molybdenum. Isotope shifts are for the $a\ ^7S_3 \rightarrow z\ ^7P_2$ transition at 390 nm and are relative to ^{96}Mo [101]. Following convention, a negative shift indicates that the lighter isotope is shifted to higher frequency.

Isotope	Natural abundance (%)	Nuclear spin I	Isotope shift (MHz)
^{92}Mo	14.84	0	−0.9144
^{94}Mo	9.25	0	−0.4107
^{95}Mo	15.92	5/2	−0.3028
^{96}Mo	16.68	0	—
^{97}Mo	9.55	5/2	−0.0180
^{98}Mo	24.13	0	−0.2938
^{100}Mo	9.63	0	−0.7945

6.5 Magnetic trapping

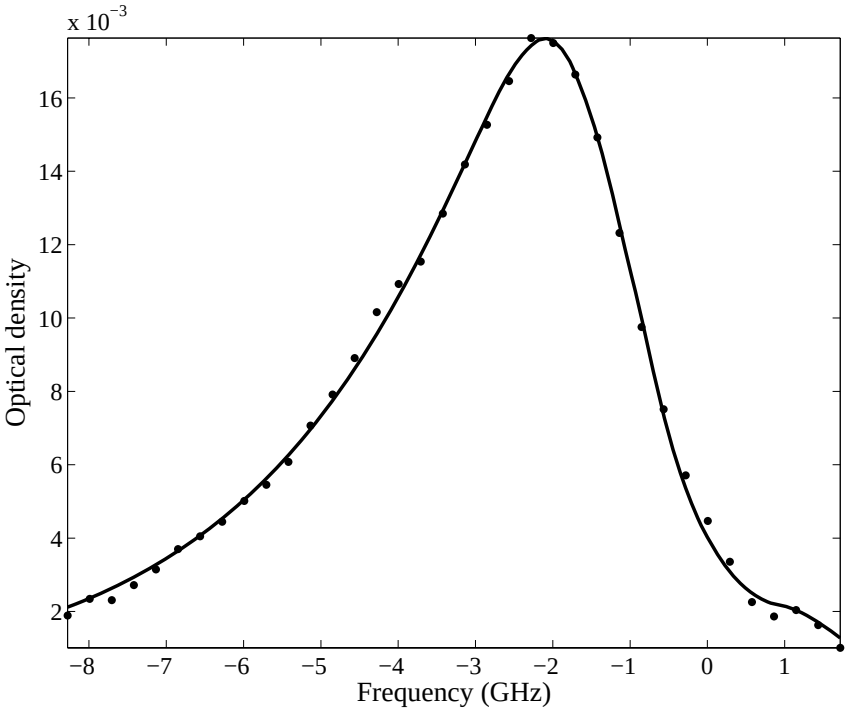

Figure 6.6: Absorption spectrum of trapped Mo at the loading trap depth of 7.2 K (2.3 T). The data are shown as filled circles. The solid line is a simulation of a trapped thermal distribution of atoms with number and temperature as free parameters. The fit indicates 2×10^{10} Mo atoms trapped at a peak density of 1×10^{11} cm^{-3} and a temperature of 500 mK.

Figure 6.6 shows a spectrum of trapped molybdenum atoms taken at the loading trap depth of 7.2 K (2.3 T) after cryopumping the buffer gas to the cell walls. The individual isotopes are unresolved due to the large magnetic broadening. A fit to the spectrum finds $(2 \pm 1) \times 10^{10}$ trapped molybdenum atoms at a temperature of 500 mK.

6.5.1 Inelastic Mo-Mo collisions

We monitor the decay of the trapped atoms to determine the Mo–Mo inelastic collision rate (Figure 6.7). The decay is fit to the expected functional form for two-body loss, $\mathrm{d}n/\mathrm{d}t = -1/8 g_{\mathrm{in}} n^2$, where g_{in} is the inelastic rate constant, n is the peak atom density in the cell, and the factor of 1/8 is a phase-space factor for our particular trapping geometry [26]. We find $g_{\mathrm{in}} = (1.2 +/- 0.6) \times 10^{-12}$ cm^3 s^{-1}. This is similar to the inelastic rate previously seen in Cr, which has the same valence electronic configuration and magnetic moment as Mo [18].

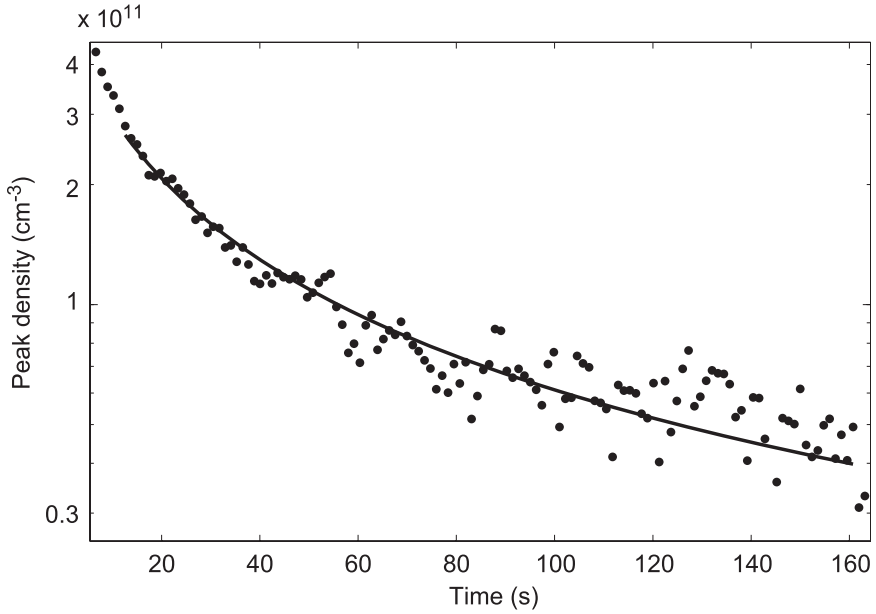

Figure 6.7: Peak density as a function of time for trapped Mo atoms. The observed time profile (filled circles) is fit for two body decay due to inelastic collisions, $\mathrm{d}n/\mathrm{d}t = -1/8 g_{\mathrm{in}} n^2$.

6.6 Evaporative cooling

Once the atoms are loaded into the trap, the trapping fields may be reduced to force evaporation. The atoms are cooled both by the evaporation and by adiabatic

expansion resulting from the reduced confinement. The electrically insulating plastic cell allows for fast ramping of the magnetic field without inducing eddy currents that would heat the cell. Figure 6.8 shows a spectrum taken after ramping the trapping fields to a depth of 0.9 K (0.3 T). Absorption lines are not observed for atoms in states other than the fully stretched state ($|m_J = 3\rangle$ for the 5 isotopes with zero nuclear spin, $|m_J = 3, m_I = 5/2\rangle$ for the 2 isotopes with $I = 5/2$). Although all m_J and m_I states are produced in the ablation, spin exchange purifies the sample by driving atoms either up in angular momentum to the fully stretched state or down to untrapped states.

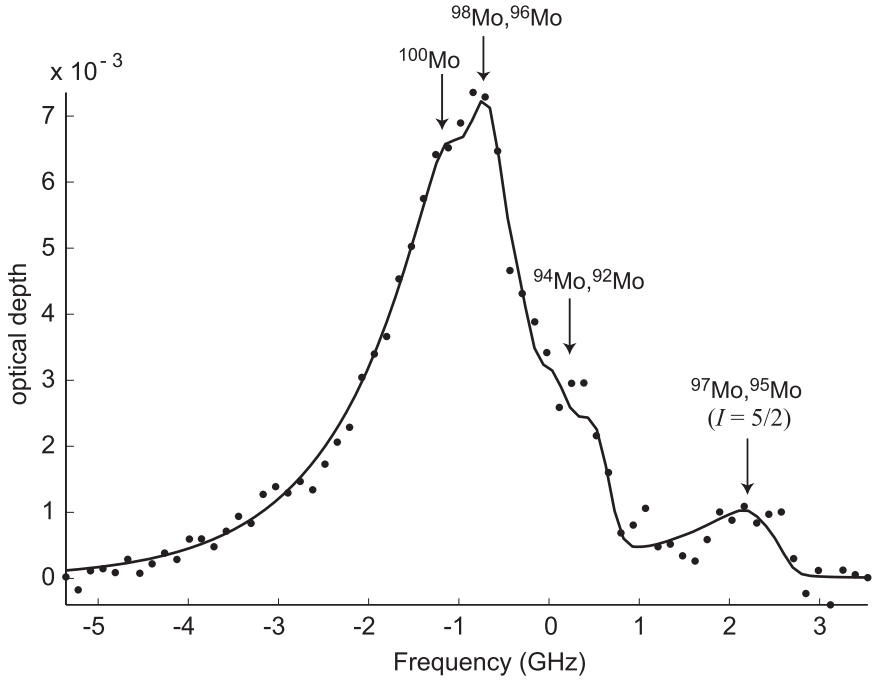

Figure 6.8: Absorption spectrum of trapped Mo after forced evaporative cooling. The trapping fields are reduced to a final trap depth of 0.9 K (0.3 T) from the loading depth of 7.2 K (2.3 T). Multiple isotopes are resolved as indicated.

The observed spectrum is fit to find the temperature and number of atoms remaining. The fit shown determines 8×10^8 atoms cooled to a temperature of 200 mK. Multiple isotopes are resolved. The known isotope shifts and relative natural abun-

Table 6.2: Hyperfine coupling constants for the $a\ ^7S_3$ [102] and $z\ ^7P_2$ [103] levels of ^{95}Mo and ^{97}Mo.

	$^7S_3$		$^7P_2$	
Isotope	A (MHz)	B (MHz)	A (MHz)	B (MHz)
^{95}Mo	−208.583	0.042	195.7	−1.5
^{97}Mo	−212.981	−0.085	199.8	15.1

dances are used to fix the relative peak positions and heights for isotopes with zero nuclear spin [101]. The known isotope shifts and hyperfine constants (see Table 6.2) are used to fix the positions of the ^{95}Mo and ^{97}Mo peaks [101, 102, 103], however their peak heights relative to the zero-nuclear-spin isotopes are allowed to vary in the fit. One might expect the height of the ^{95}Mo and ^{97}Mo peaks to be reduced by a factor of $2I + 1$, however we see a reduction only of a factor of 3. The fully stretched state population is enhanced after the ablation, possibly due to spin exchange, as was seen previously with Cr [18]. The trap density is too low to allow for a measurement of the inelastic rate at this temperature.

6.7 Conclusions and future prospects

In conclusion, we have magnetically trapped all naturally occurring isotopes of molybdenum in large numbers and evaporatively cooled them to a temperature of 200 mK. The inelastic Mo–Mo collision rate is measured and found to be similar to that found in Cr–Cr collisions. Further cooling of molybdenum to temperatures lower than 200 mK would benefit from a technique such as cooling by evaporation via optical pumping [104], which avoids the decrease in trap densities associated with the lowering of the magnetic trapping field. Another possibility is evaporation by moving the atom cloud to the cell wall [105].

Appendix A

Hyperfine spectrum simulation

The field-free Hamiltonian H of an atom with total electronic angular momentum $\mathbf{J}$ and nuclear spin $\mathbf{I}$ is

$$H = A\ \mathbf{I}\cdot\mathbf{J} + B\frac{\frac{3}{2}\mathbf{I}\cdot\mathbf{J}(2\mathbf{I}\cdot\mathbf{J}+1) - \mathbf{I}^2\mathbf{J}^2}{2I(2I-1)J(2J-1)}, \tag{A.1}$$

where A and B are the hyperfine magnetic dipole and electric quadrupole coupling constants.[1]

The eigenvectors are $|F, m\rangle$ states, whose eigenenergies are trivial to calculate by utilizing the identity $\mathbf{I}\cdot\mathbf{J} = \frac{1}{2}(\mathbf{F}^2 - \mathbf{I}^2 - \mathbf{J}^2)$. We find

$$E = A\frac{K}{2} + B\frac{3K(K+1) - 4I(I+1)J(J+1)}{8I(2I-1)J(2J-1)}, \tag{A.2}$$

with $K = F(F+1) - J(J+1) - I(I+1)$.

From conservation of angular momentum, we have the following selection rules for

[1]Note that the electric quadrupole interaction exists only for $I \geq 1$ and $J \geq 1$. Yttrium ($I = 1/2$) therefore has only the magnetic dipole interaction.

electric dipole transitions between hyperfine states of two different levels J and J'

$$\begin{aligned} \Delta F &= -1, 0, 1, \quad F + F' \geq 1, \\ \Delta m &= -1, 0, 1 \end{aligned} \tag{A.3}$$

The relative line intensities are derived in Reference [106]; we quote the results here. The relative line intensities for transitions between states $|\gamma JIF\rangle$ and $|\gamma' J' IF'\rangle$ are

$$S(\gamma JIF, \gamma' J' IF') = (2I+1) Q(IJF, IJ'F') S(\gamma J, \gamma' J'), \tag{A.4}$$

with

$$Q(IJF, IJ'F') = \frac{(2F+1)(2F'+1)}{2I+1} \left\{ \begin{array}{ccc} J & F & I \\ F' & J' & 1 \end{array} \right\}^2 . \tag{A.5}$$

$S(\gamma J, \gamma' J')$ is the total line strength. The label γ represents non-angular-momenta quantum numbers which specify the electronic state. Values for Q maybe calculated using the formulas in Table A.1 and the rule that the $6j$-symbol remains invariant under the transpose of any two columns, and under the transpose of the lower and upper arguments in each of any two columns.

Table A.1: Formulas for calculating $Q(xyz; xy'z')$

y'	z'	$Q(xyz; xy'z')$
y	z	$\frac{[y(y+1)+z(z+1)-x(x+1)]^2(2z+1)}{4y(y+1)(2y+1)z(z+1)(2x+1)}$
$y-1$	z	$\frac{(x+y+z+1)(y+z-x)(x+y-z)(x+z-y+1)(2z+1)}{4z(z+1)(2y-1)(2y+1)y(2x+1)}$
y	$z-1$	$\frac{(x+y+z+1)(y+z-x)(x+z-y)(y+x+1-z)}{4y(y+1)(2y+1)z(2x+1)}$
$y-1$	$z-1$	$\frac{(y+x+z)(y+x+z+1)(y+z-x-1)(y+z-x)}{4(2y-1)y(2y+1)z(2x+1)}$
$y+1$	$z-1$	$\frac{(x+z-y-1)(x+z-y)(x+y-z+1)(x+y-z+2)}{4(2y+1)(y+1)(2y+3)z(2x+1)}$

Appendix B

Rare-earth trapped spectra

Here we present individual trapped spectra for the rare-earth atoms Pr, Nd, Tb, Dy, Ho, Er, and Tm. The optical transitions used in the absorption detection are listed in Table 2.3. The Ho spectrum is taken using a single ablation pulse by frequency scanning the laser. The spectrum represents one ramp of the laser (plus baseline measurement) at $t = 90$ to 160 ms. All other spectra are taken by measuring the absorption time profile a single laser frequency at a time, and stepping across spectrum. Several measurements (each measurement consists of a baseline measurement and post-ablation time profile) are taken at each frequency so that variations in ablation yield may be averaged out. The standard deviations of these averages are indicated by the error bars at each point in the spectrum.

Each spectrum is fit for temperature and number of atoms trapped. There is a large error, ± 200 mK in the temperature fits due to the uncertainty in the relative populations of Zeeman levels in the trap. We find that the temperatures of all species agree within this error. This agreement is expected since the measured temperature in all cases should reflect the buffer-gas temperature, and should be roughly the same in each case. (The same ablation pulse energy of 10 mJ is used for each species, and

in each case, the buffer-gas density is held constant at $n_{\mathrm{He}} = (7.6 \pm 3.3) \times 10^{15}$ cm^{-3}.)

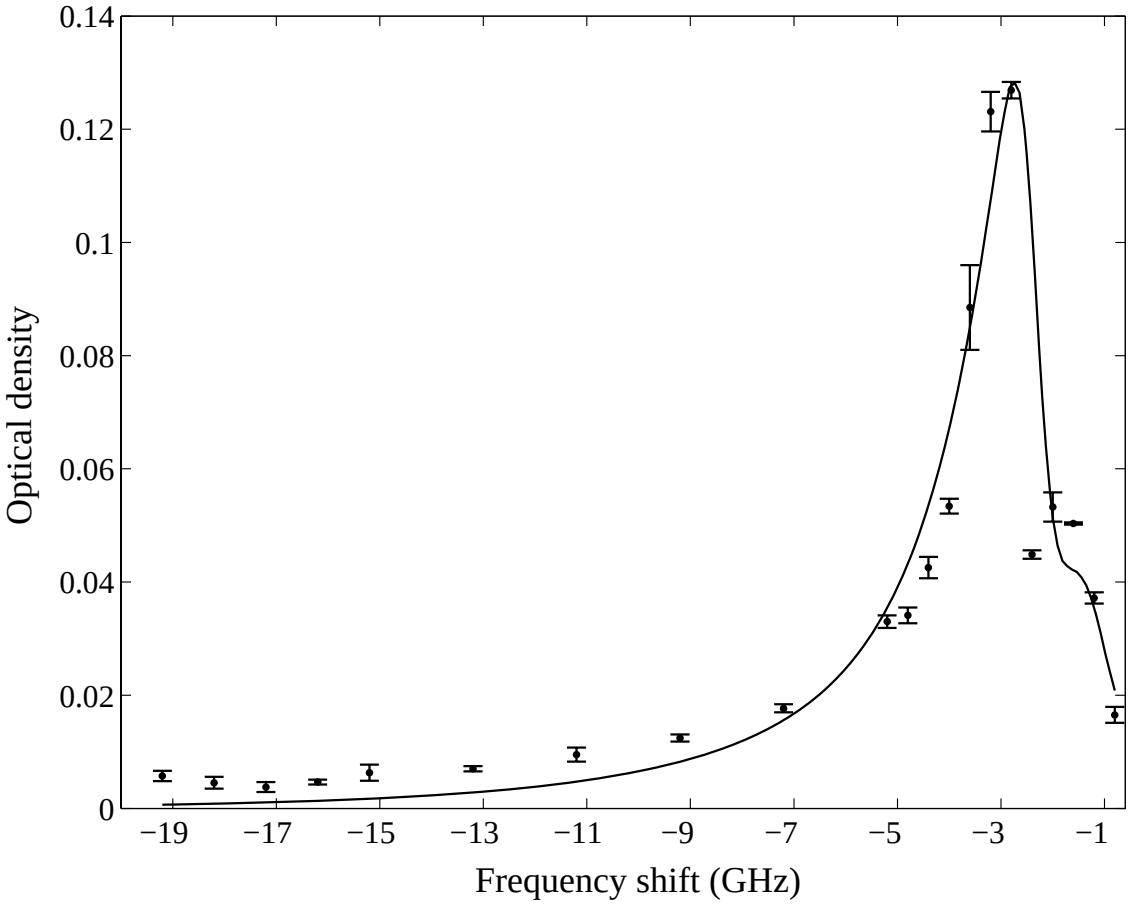

Figure B.1: Spectrum of trapped Pr atoms at a trap depth of 2.8 T taken 100 ms after the ablation pulse. The solid curve is a simulation of a trapped thermal distribution with 4×10^{11} Pr atoms trapped at a temperature of 700 mK.

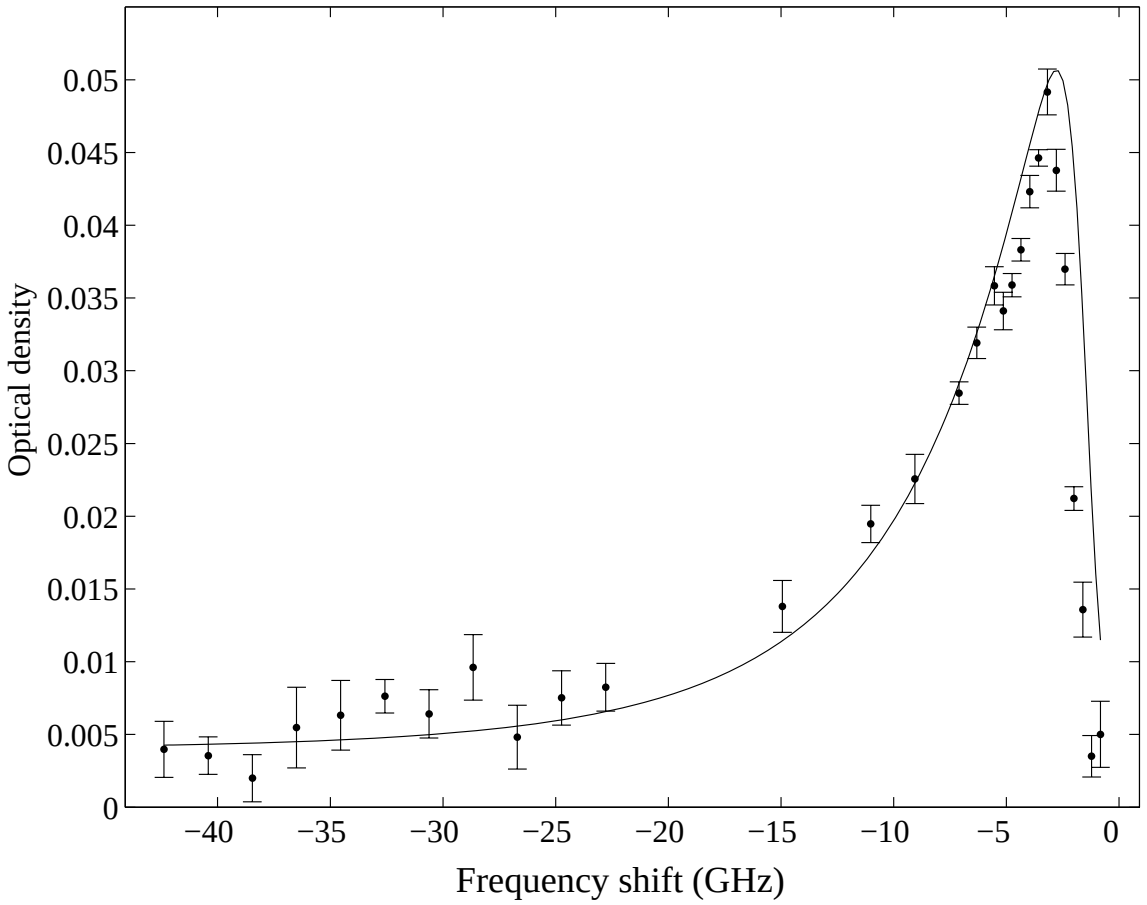

Figure B.2: Spectrum of trapped Nd atoms at a trap depth of 2.8 T taken 100 ms after the ablation pulse. The solid curve is a simulation of a trapped thermal distribution with 7×10^{11} Nd atoms trapped at a temperature of 1 K.

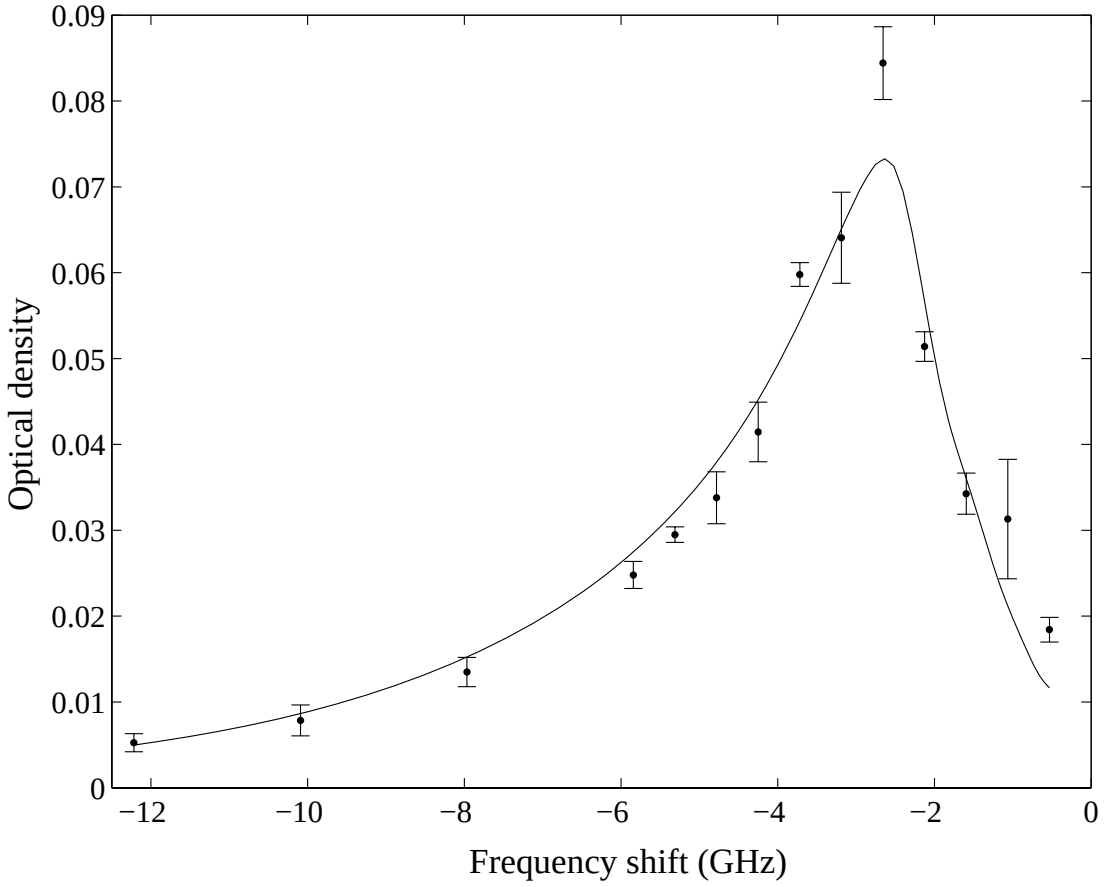

Figure B.3: Spectrum of trapped Tb atoms at a trap depth of 1.2 T taken 100 ms after the ablation pulse. The solid curve is a simulation of a trapped thermal distribution with 5×10^{11} Tb atoms trapped at a temperature of 0.9 K.

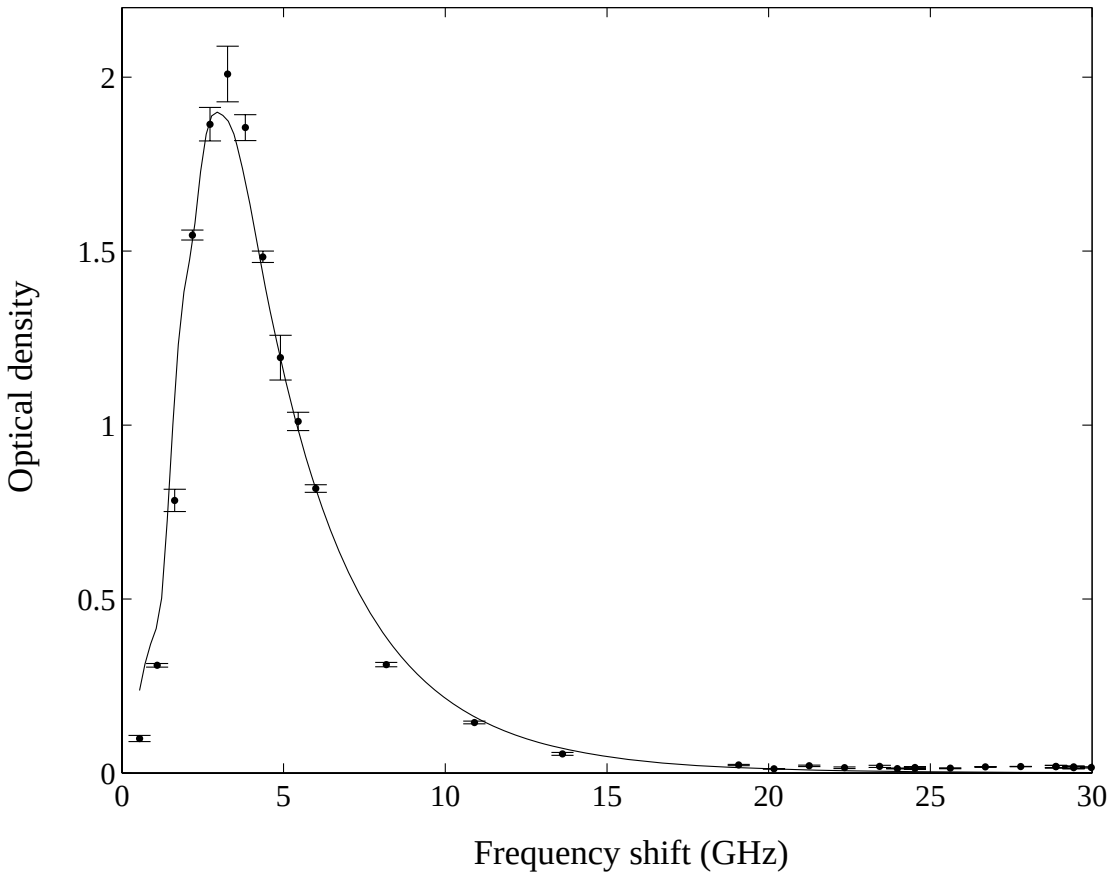

Figure B.4: Spectrum of trapped Dy atoms at a trap depth of 1.6 T taken 100 ms after the ablation pulse. The solid curve is a simulation of a trapped thermal distribution with 6×10^{11} Dy atoms trapped at a temperature of 0.9 K.

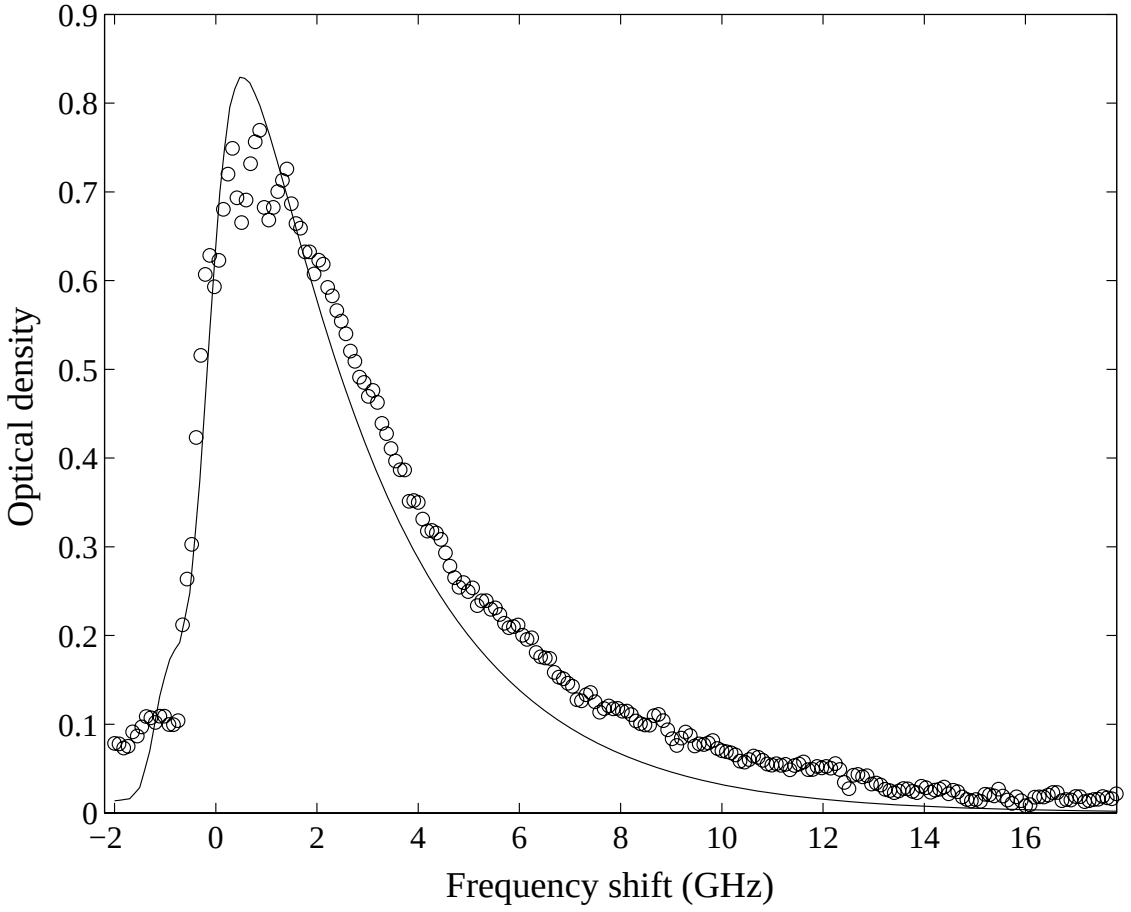

Figure B.5: Spectrum of trapped Ho atoms at a trap depth of 1.2 T taken from 90 to 160 ms after the ablation pulse. The solid curve is a simulation of a trapped thermal distribution. The g-factor for the excited state is unknown, so it is not possible to fit for the temperature of the atoms. A temperature of 1 K is assumed, and the g-factor is adjusted until a reasonable fit is achieved. The simulation uses a g-factor for the excited state of 1.4, and finds 1×10^{12} Ho atoms trapped.

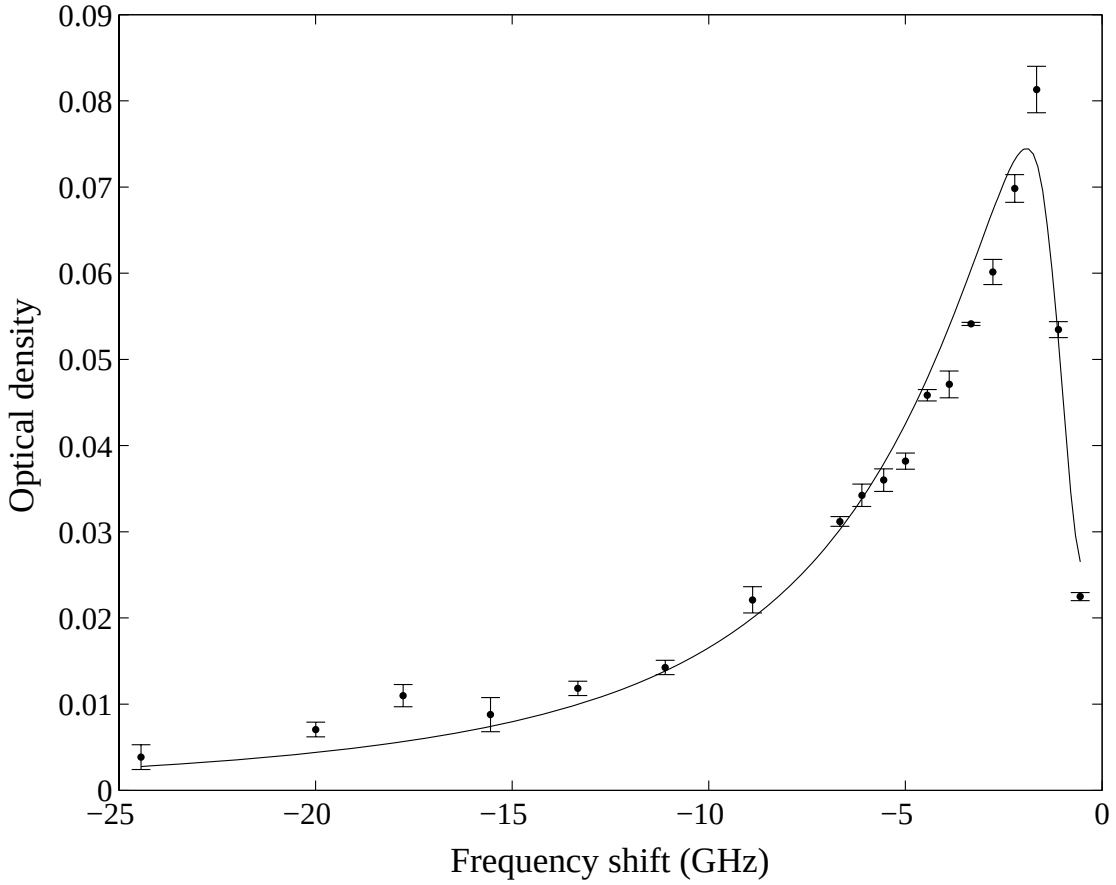

Figure B.6: Spectrum of trapped Er atoms at a trap depth of 1.6 T taken 100 ms after the ablation pulse. The solid curve is a simulation of a trapped thermal distribution with 5×10^{10} Er atoms trapped at a temperature of 0.6 K.

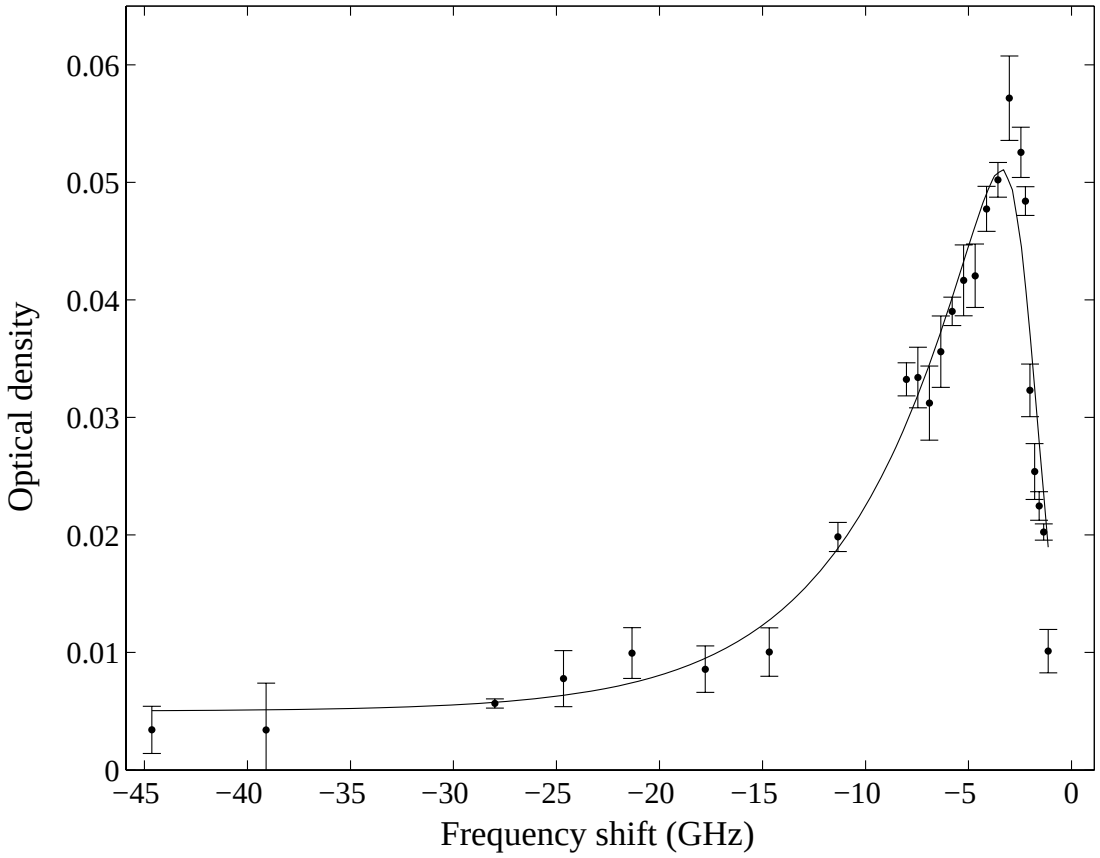

Figure B.7: Spectrum of trapped Tm atoms at a trap depth of 2.8 T taken 50 ms after the ablation pulse. The solid curve is a simulation of a trapped thermal distribution with 2×10^{11} Tm atoms trapped at a temperature of 0.8 K.

Appendix C

Extra light

At high buffer-gas densities we sometimes measured a *greater* amount of probe light at the signal PMT after the ablation than before. This runs counter to the usual situation where the ablated atoms absorb the probe light rather than add to it. While we don't have a physical explanation for the "extra light" events, we detail our observations in this Appendix.

Extra light was seen in Ti and Dy measurements at a buffer-gas density of $n_{\mathrm{He}} = (4 \pm 2) \times 10^{16}$ cm^3 (no other species were investigated for this effect). Extra light was not seen in measurements taken at half this buffer-gas density (no measurements were taken at intermediate values of n_{He}).

Absorption measurements

As shown schematically in Figure 2.3, the probe beam is split by a beamsplitter mounted below the dewar into two beams– "signal" and "reference." The reference beam passes through the beamsplitter and travels directly to the reference PMT. The signal beam reflects off of the beamsplitter and into the cell, where it is retroreflected and sent back out of the cryostat. It is then directed into the signal PMT. Each

PMT outputs a current proportional to the intensity of light collected. The current is converted to a voltage using a current preamplifier and digitized. Prior to digitization, an offset is applied to zero out background light. This is done by blocking the probe beam at the optics table and adjusting the current offset on the preamplifier so that the voltage output is 0 V.

Intensity fluctuations in the laser beam are divided out by taking a ratio of the signal and reference voltages. We call this ratio "the Divide" and denote as $D(t) \equiv V_{\text{signal}}(t)/V_{\text{reference}}(t)$.

A baseline measurement is taken prior to each ablation pulse. The absorption is given by:

$$A(t) = 1 - \frac{D(t)}{D_{\text{baseline}}}, \tag{C.1}$$

where D_{baseline} is the baseline divide measured before the ablation. The baseline is, in general, frequency dependent, so if the laser frequency is swept then

$$A(f,t) = 1 - \frac{D(f,t)}{D_{\text{baseline}}(f)}. \tag{C.2}$$

In this Appendix we generally plot the signal PMT voltage or measured absorption rather than optical density since the latter is undefined for "extra light."

Ti observations

Extra light was seen in Ti spectra taken during the first run of the non-S-state atom experiments. We first took spectra at zero-field and saw nothing unusual. We then ramped the (anti-Helmholtz) magnet to a current of 60 A to take spectra of the high-field-seeking (HFS) atoms at the field saddle. Figure C.1 shows two measured absorption spectra for the HFS atoms at the saddle, taken at different time delays

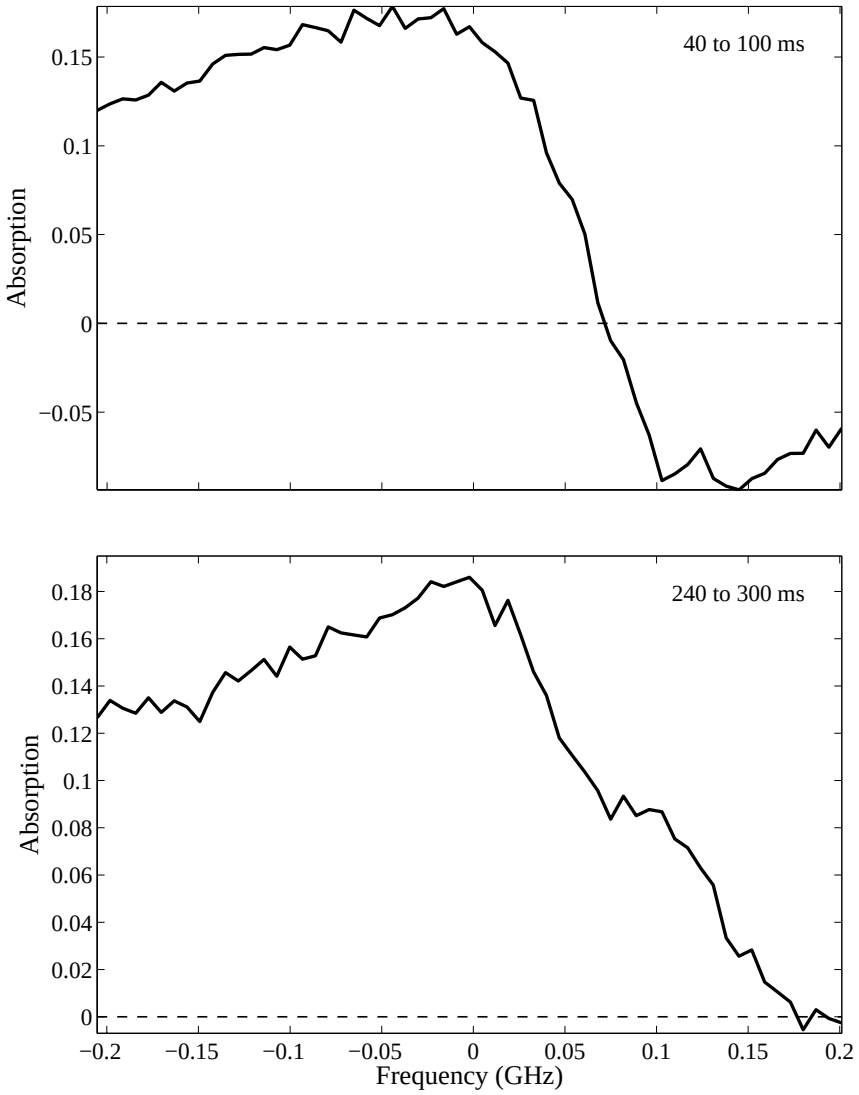

Figure C.1: Negative absorption in the high-field-seeker spectrum for Ti.

following the ablation. The later spectrum looks as expected and is similar to HFS spectra taken at lower buffer-gas densities following the ablation (*e.g.* Figure 3.11). In the earlier spectrum, however, we see the absorption go *negative*. This negative absorption corresponds to extra light reaching the signal PMT compared to the baseline measurement. The extra light is most pronounced at the shoulder of the HFS saddle peak. For further investigations, we park the laser frequency on or near this

shoulder.

The extra light seen strongly depends on ablation energy. Figure C.2 shows the Divide measured at the HFS shoulder for three different ablation energy. At the lowest ablation energy, there is no extra light seen.[1]

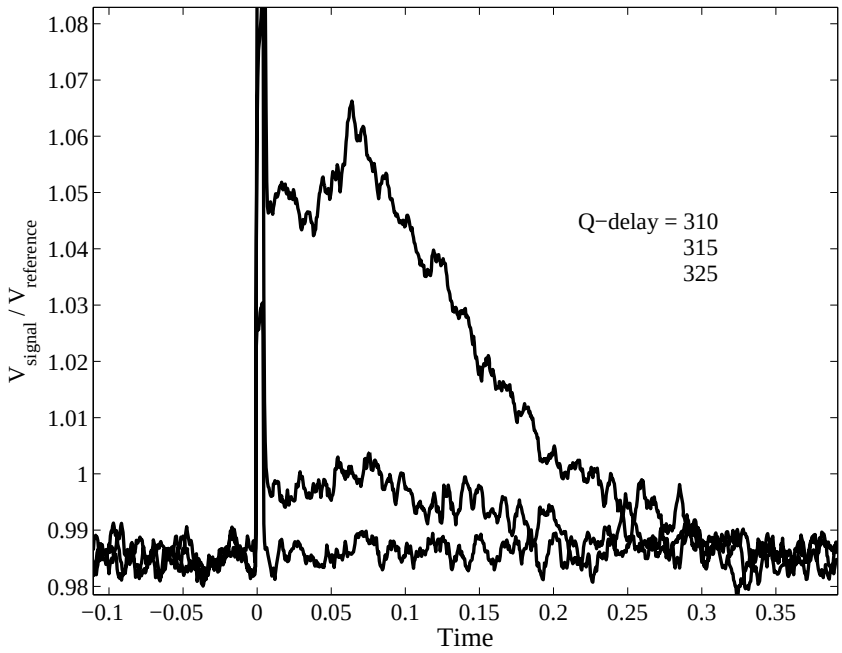

Figure C.2: "Extra light" dependence on ablation energy. Q-delays are given in μs. These curves are measured with the laser parked on the shoulder of the Ti HFS saddle peak.

The extra light strongly depends on laser frequency. As the laser frequency is shifted blue, away from the saddle peak, the amount of extra light decreases sharply. Figure C.3 shows the Divide for two different frequencies. Less extra light is seen in the gray curve, for which the laser is shifted 160 MHz farther (to the blue) from the HFS saddle peak. Extra light is only seen at frequencies just blue of the HFS

[1]The narrow spike in the Divide seen at $t = 0$ is due to light from the ablation pulse. The ablation light decays quickly, and disappears into the noise within 3 ms.

saddle peak. No extra light is seen near the low-field-seeker (LFS) saddle peak. This is perhaps not surprising since the LFS atoms relax to other states in the first few milliseconds after the ablation and the extra light is seen only near strong absorption peaks.

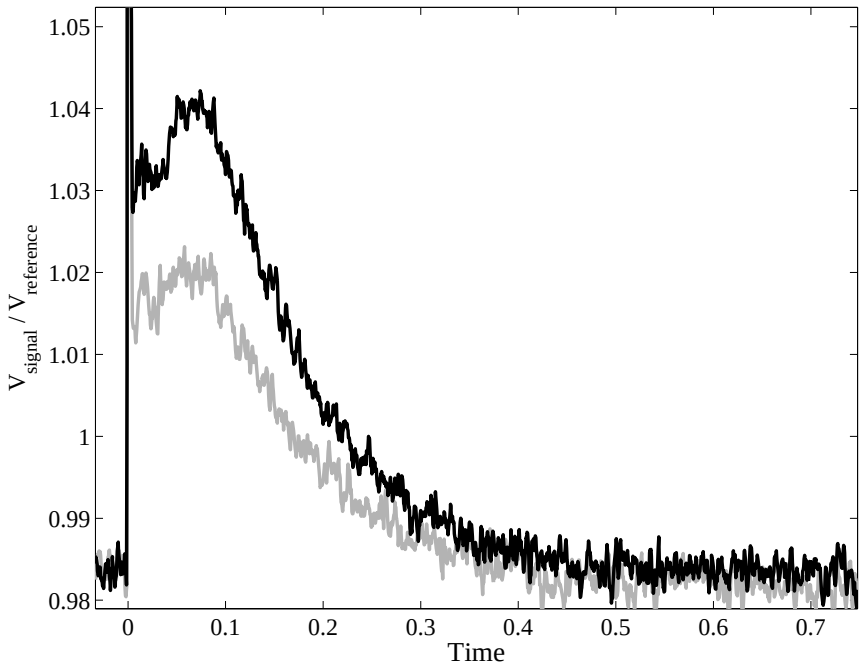

Figure C.3: "Extra light" profiles for two different laser frequencies. The gray curve is taken with the laser shifted 160 MHz farther away from the HFS field saddle peak than for the black curve.

The amount of extra light seen is proportional to probe beam intensity. Figure C.4 shows the measured signal voltage for two different probe intensities. In the bottom panel, the probe intensity is reduced by a factor of 4 compared to the top panel. The gain setting for the PMT is held constant, so the bottom panel shows a smaller absolute voltage (the amount of light collected is proportional to -V_{signal}). We see roughly 1/4 as much extra light in the bottom panel, consistent with the extra light being proportional to probe beam intensity.

The extra light is coherent. We speculated that the extra light was coming from

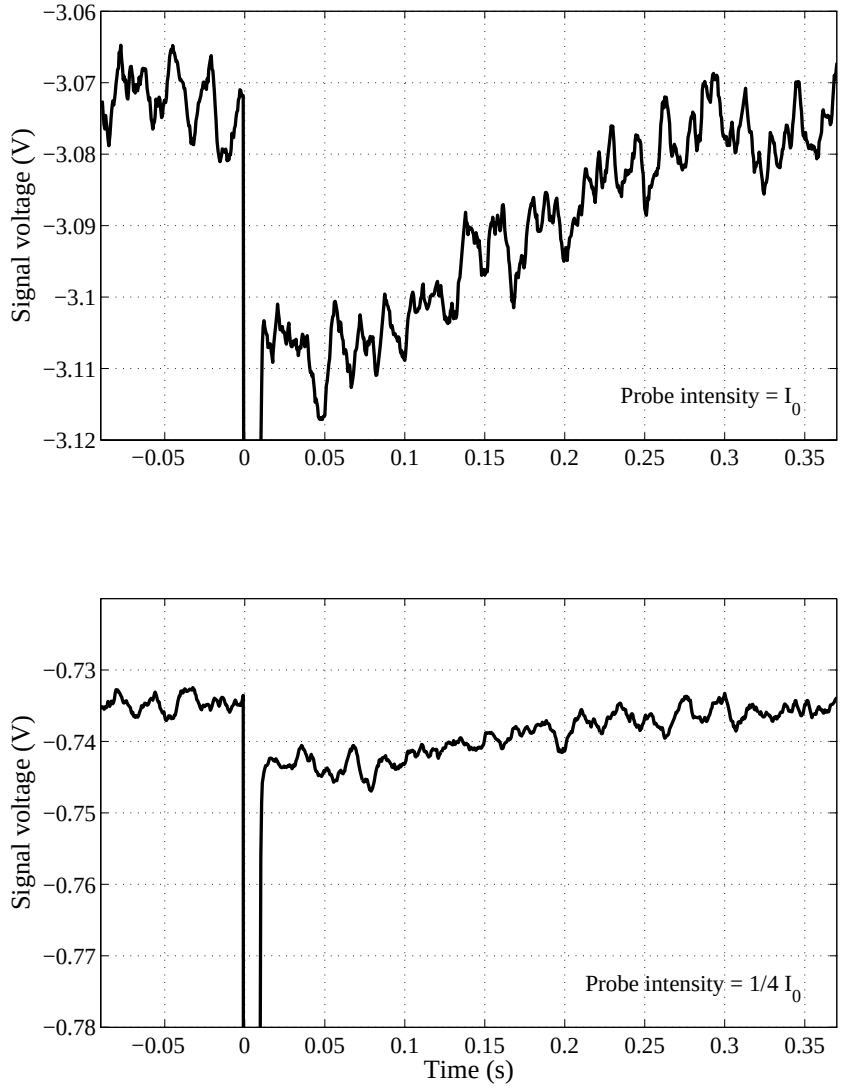

Figure C.4: Signal voltage versus time for two different probe beam intensities. The laser intensity in the upper plot is 4 times larger than in the lower plot. The amount of extra light seen is roughly 4 times greater in the upper plot, thus indicating that the amount of extra light collected at the PMT scales with probe beam intensity.

additional scattering in the cell that increased the light making its way to the signal PMT. In that case, the amount of extra light seen should decrease if the signal beam is irised before reaching the PMT, or if the PMT is moved farther away from the

cryostat. We saw, however, no effect on the amount of extra light seen in either case.

Dy observations

Extra light is seen in Dy measurements near both the HFS and LFS absorption peaks. In the Dy measurements, the magnet is run in the Helmholtz configuration with a current of 10 A. Figure C.5 shows the measured absorption profile with the laser

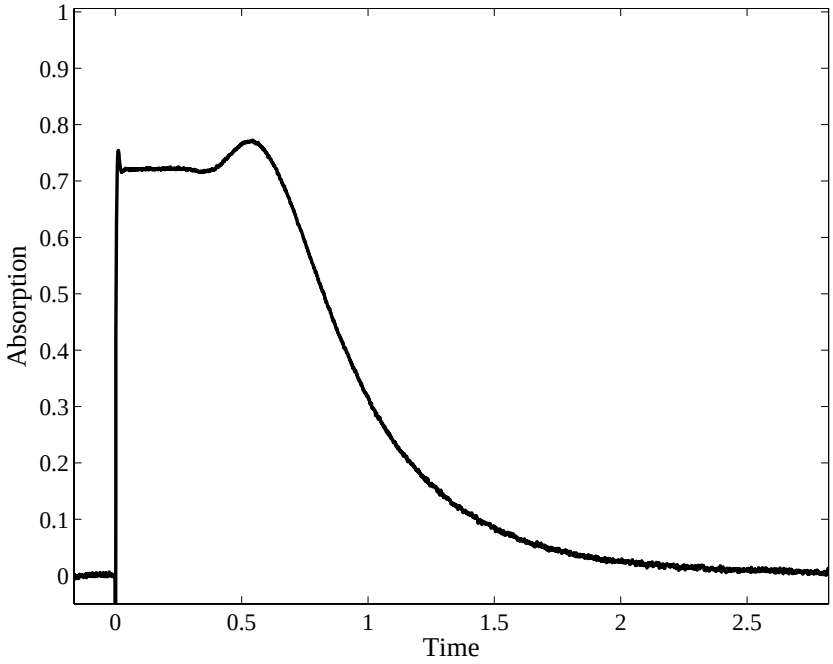

Figure C.5: Absorption time profile with the laser frequency parked directly on the high-field-seeker absorption peak for Dy. There appears to be extra light suppressing the absorption signal in the first 500 ms.

parked on the HFS absorption peak. While the absorption never goes negative, there does appear to be extra light in the first several hundred milliseconds. The absorption is remarkably constant from 40 to 300 ms considering that the atom density should be fall significantly during this time due to diffusion. Constant absorption for changing atom density is generally seen only for $A = 1$, *i.e.* when the probe beam is completely

absorbed as it passes through the cell, making the absorption insensitive to atom density. In the figure, however, the apparent absorption is only 72%. We believe that we do indeed have 100% absorption during this time, and the discrepancy seen is due to extra light. As the extra light decays, we eventually have an increase of apparent absorption, at $t \sim 500$ ms. There is also a period of higher absorption seen in the first 40 ms following the ablation—this is consistent with the extra light rise time seen in the Figure C.3 (black curve).

We also see extra light in the LFS spectra. Figure C.6 shows the absorption time profile seen for frequency sweeps across the LFS absorption peak. The measured absorption clearly dips below zero at times greater than 150 ms. The laser frequency ramp is overlaid for reference.

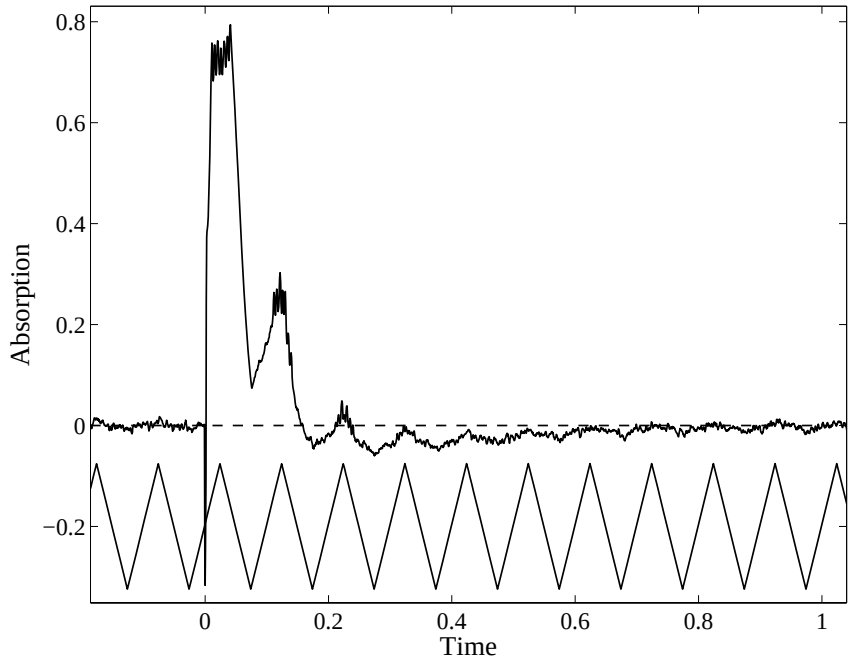

Figure C.6: Absorption time profile with the laser scanning over the Dy low-field-seeker absorption peak. The absorption dips below zero, indicating the presence of extra light.

Bibliography

[1] A. L. Migdall, John V. Prodan, William D. Phillips, Thomas H. Bergeman, and Harold J. Metcalf. First observation of magnetically trapped neutral atoms. *Physical Review Letters* **54**, 2596–2599 (1985).

[2] M.H. Anderson, J.R. Ensher, M.R. Matthews, C.E. Wieman, and E.A. Cornell. Observation of Bose-Einstein condensation in a dilute atomic vapor. *Science* **269**, 198 (1995).

[3] C. C. Bradley, C. A. Sackett, J. J. Tollet, and R. G. Hulet. Evidence of Bose-Einstein condensation in an atomic gas with attractive interactions. *Physical Review Letters* **75**, 1687–1690 (1995).

[4] K. B. Davis, M. O. Mewes, M. R. Andrews, N. J. van Druten, D. S. Durfee, D. M. Kurn, and W. Ketterle. Bose-Einstein condensation in a gas of sodium atoms. *Physical Review Letters* **75**, 3969–3973 (1995).

[5] R. Wynar, R. S. Freeland, D. J. Han, C. Ryu, and D. J. Heinzen. Molecules in a Bose-Einstein condensate. *Science* **287**, 1016–1019 (2002).

[6] E. A. Donley, N. R. Claussen, S. T. Thompson, and C. E. Wieman. Atom-molecule coherence in a Bose-Einstein condensate. *Nature* **417**, 529–533 (2002).

[7] M. Greiner, C. A. Regal, and D. S. Jin. Emergence of a molecular Bose-Einstein condensate from a Fermi gas. *Nature* **426**, 537–540 (2003).

[8] S. Jochim, M. Bartenstein, A. Altmeyer, G. Hendl, S. Riedl, C. Chin, J. Hecker Denschlag, and R. Grimm. Bose-Einstein condensation of molecules. *Science* **302**, 2101–2103 (2003).

[9] A. Widera, O. Mandel, M. Greiner, S. Kreim, T. W. Hansch, and I. Bloch. Entanglement interferometry for precision measurement of atomic scattering properties. *Physical Review Letters* **92**, 160406 (2004).

[10] Y.-J. Lin, I. Teper, C. Chin, and V. Vuletic. Impact of the Casimir-Polder potential and Johnson noise on Bose-Einstein condensate stability near surfaces. *Physical Review Letters* **92**, 050404 (2004).

[11] Yosuke Takasu, Kenichi Maki, Kaduki Komori, Tetsushi Takano, Kazuhito Honda, Mitsutaka Kumakura, Tsutomu Yabuzaki, and Yoshiro Takahashi. Spin-singlet Bose-Einstein condensation of two-electron atoms. *Physical Review Letters* **91**, 040404 (2003).

[12] Axel Griesmaier, Jorg Werner, Sven Hensler, Jurgen Stuhler, and Tilman Pfau. Bose-Einstein condensation of chromium. *Physical Review Letters* **94**, 160401 (2005).

[13] Robert deCarvalho, John M. Doyle, Bretislav Friedrich, Thierry Guillet, Jinha Kim, David Patterson, and Jonathan D. Weinstein. Buffer-gas loaded magnetic traps for atoms and molecules: a primer. *European Physical Journal D* **7**, 289–309 (1999).

[14] R. deCarvalho, N. Brahms, B. Newman, J.M. Doyle, D. Kleppner, and T. Greytak. A new path to ultracold hydrogen. *Canadian Journal of Physics* **83**, 293–300 (2005).

[15] Andrew J. Kerman, Jeremy M. Sage, Sunil Sainis, Thomas Bergeman, and David DeMille. Production and state-selective detection of ultracold RbCs molecules. *Physical Review Letters* **92**, 153001 (2004).

[16] M. Baranov, L. Dobrek, K. Goral, L. Santos, and M. Lewenstein. Ultracold dipolar gases - a challenge for experiments and theory. *Phys. Scr.* **T102**, 74 (2002). See also references therein.

[17] S. Yi and L You. Probing dipolar effects with condensate shape oscillation. *Phys. Rev. A* **66**, 013607 (2002).

[18] Jonathan D. Weinstein, Robert deCarvalho, Cindy I. Hancox, and John M. Doyle. Evaporative cooling of atomic chromium. *Physical Review A* **65**, 021604R (2002).

[19] Jinha Kim, Bretislav Friedrich, Daniel P. Katz, David Patterson, Jonathan D. Weinstein, Robert DeCarvalho, and John M. Doyle. Buffer-gas loading and magnetic trapping of atomic europium. *Physical Review Letters* **78**, 3665–3668 (1997).

[20] A. Derevianko and C. C. Cannon. Quantum computing with magnetically interacting atoms. *Physical Review A* **70**, 62319 (2004).

[21] David DeMille. Quantum computation with trapped polar molecules. *Physical Review Letters* **88**, 067901 (2002).

[22] V. A. Dzuba, V. V. Flambaum, and M. V. Marchenko. Relativistic effects in Sr, Dy, YbII, and YbIII and search for variation of the fine-structure constant. *Physical Review A* **68**, 022506 (2003).

[23] A. T. Nguyen, D. Budker, S. K. Lamoreaux, and J. R. Torgerson. Towards a sensitive search for variation of the fine-structure constant using radio-frequency E1 transitions in atomic dysprosium. *Physical Review A* **69**, 022105 (2004).

[24] M. D. Barrett, J. A. Sauer, and M. S. Chapman. All-optical formation of an atomic Bose-Einstein condensate. *Physical Review Letters* **87**, 010404 (2001).

[25] S. R. Granade, M. E. Gehm, K. M. O'Hara, and J. E. Thomas. All-optical production of a degenerate Fermi gas. *Physical Review Letters* **88**, 120405 (2002).

[26] W. Ketterle and N. J. Van Druten. Evaporative cooling of trapped atoms. *Advances in Atomic, Molecular, and Optical Physics* **37**, 181–236 (1996).

[27] Roman V. Krems, G. C. Groenenboom, and Alex Dalgarno. Electronic interaction anisotropy between atoms in arbitrary angular momentum states. *Journal of Physical Chemistry A* **108**, 8941–8948 (2004).

[28] Robin Santra and Chris H. Greene. Tensorial analysis of the long-range interaction between metastable alkaline-earth-metal atoms. *Physical Review A* **67**, 062713 (2003).

[29] Roman V. Krems and Alex Dalgarno. Disalignment transitions in cold collisions of ^3P atoms with structureless targets in a magnetic field. *Physical Review A* **68**, 013406 (2003).

[30] Vincenzo Aquilanti, Roberto Candori, and Fernando Pirani. Molecular beam studies of weak interactions for open-shell systems: the ground and lowest excited states of rare gas oxides. *Journal of Chemical Physics* **89**, 6157–6164 (1988).

[31] Vincenzo Aquilanti, David Cappelletti, Vincent Lorent, Emilio Luzzatti, and Fernando Pirani. Molecular beam studies of weak interactions of open-shell atoms: the ground and lowest excited states of rare-gas chlorides. *Journal of Physical Chemistry* **97**, 2063–2971 (1993).

[32] H. Katori, T. Ido, Y. Isoya, and M. Kuwata-Gonokami. *Atomic Physics XVII*. AIP Conf. Proc. No. 551. AIP, Melville, NY, 2001.

[33] S. Nagel, C. Simien, S. Laha, P. Gupta, V. Ashoka, and T. Killian. Magnetic trapping of metastable $^3P_2$ atomic strontium. *Physical Review A* **67**, 011401 (2003).

[34] X. Xu, T. H. Loftus, J. L. Hall, A. Gallagher, and J. Ye. Cooling and trapping of atomic strontium. *Journal of the Optical Society of America B* **20**, 968–976 (2003).

[35] J. Stuhler, P. O. Schmidt, S. Hensler, J. Werner, J. Mlynek, and T. Pfau. Continuous loading of a magnetic trap. *Physical Review A* **64**, 031405 (2001).

[36] D. P. Hansen, J. R. Mohr, and A. Hemmerich. Magnetic trapping of metastable calcium atoms. *Physical Review A* **67**, 021401 (2003).

[37] Viatcheslav Kokoouline, Robin Santra, and Chris H. Greene. Multichannel cold collisions between metastable Sr atoms. *Physical Review Letters* **90**, 253201 (2003).

[38] Piet O. Schmidt, Sven Hensler, Jorg Werner, Thomas Binhammer, Axel Gorlitz, and Tilman Pfau. Continuous loading of cold atoms into a Ioffe-Pritchard magnetic trap. *Journal of Optics B* **5**, S170–S177 (2003).

[39] NIST atomic spectra database, URL `http://physics.nist.gov/PhysRefData-/ASD/index.html`.

[40] R. V. Krems, J. Klos, M. F. Rode, M. M. Szczesniak, G. Chalasinski, and A. Dalgarno. Suppression of angular forces in collisions of non-s-state transition metal atoms. *Physical Review Letters* **94**, 103202 (2005).

[41] A.A. Buchachenko and R.V. Krems. Dipole polarizability anisotropy of rare earth atoms from cold collision experiment. *to be submitted* (2005).

[42] Donald C. Griffin, Kenneth L. Andrew, and Robert D. Cowan. Theoretical calculations of the $d-$, $f-$, and $g-$electron transition series. *Physical Review* **177**, 62–71 (1969).

[43] L. Santos, G. V. Shlyapnikov, P. Zoller, and M. Lewenstein. Bose-Einstein condensation in trapped dipolar gases. *Physical Review Letters* **85**, 1791 (2000).

[44] M. A. Baranov, M. S. Mar'enko, V. S. Rychkov, and G. V. Shlyapnikov. Superfluid pairing in a polarized dipolar Fermi gas. *Physical Review A* **66**, 013606 (2002).

[45] L. Santos, G. V. Shlyapnikov, and M Lewenstein. Roton-maxon spectrum and stability of trapped dipolar Bose-Einstein condensates. *Physical Review Letters* **90**, 250403 (2003).

[46] Andrew G. Truscott, Kevin E. Strecker, William I. McAlexander, Guthrie B. Partridge, and Randall G. Hulet. Observation of Fermi pressure in a gas of trapped atoms. *Science* **291**, 2570–2572 (2001).

[47] B. DeMarco and D. S. Jin. Onset of Fermi degeneracy in a trapped atomic gas. *Science* **285**, 1703 (1999).

[48] C. J. Myatt, E. A. Burt, R. W. Ghrist, E. A. Cornell, and C. E. Wieman. Production of two overlapping Bose-Einstein condensates by sympathetic cooling. *Physical Review Letters* **78**, 586–589 (97).

[49] Cindy I. Hancox, Stephen C. Doret, Matthew T. Hummon, Roman Krems, and John M. Doyle. Suppression of angular momentum transfer in cold collisions of transition metal atoms in ground states with nonzero orbital angular momentum. *Physical Review Letters* **94**, 013201 (2005).

[50] P. Doe, H. Ejirii, and S. R. Elliot. Neutrino studies in Mo-100 and MOON-Mo observatory of neutrinos. *Nuclear Physics A* **721**, 517C–520C (2003).

[51] A. Robert, O. Sirjean, A. Browaeys, J. Poupard, S. Nowak, D. Boiron, C. I. Westbrook, and A. Aspect. A Bose-Einstein condensate of metastable atoms. *Science* **292**, 461–464 (2001).

[52] F. P. Dos Santos, J. Leonard, J. M. Wang, C. J. Barrelet, F. Perales, E. Rasel, C. S. Unnikrishnan, M. Leduc, and C. Cohen-Tannoudji. Bose-Einstein condensation of metastable helium. *Physical Review Letters* **86**, 3459–3462 (2001).

[53] I. F. Silvera, C. Gerz, L. S. Goldner, W. D. Phillips, M. W. Reynolds, S. L. Rolston, R. J. C. Spreeuw, and C. I. Westbrook. Demonstration of a microwave trap for cesium atoms. *Physica B* **194-196**, 893–894 (1994).

[54] C. C. Agosta, I. F. Silvera, H. T. C. Stoof, and B. J. Verhaar. Trapping of neutral atoms with resonant microwave radiation. *Physical Review Letters* **62**, 2361–2364 (1989).

[55] J. D. Miller, R. A. Cline, and D. J. Heinzen. Far-off-resonance optical trapping of atoms. *Physical Review A* **47**(6), R4567 (1993).

[56] Jonathan D. Weinstein. *Magnetic trapping of atomic chromium and molecular calcium monohydride.* PhD thesis, Harvard University, 2001.

[57] Jinha Kim. *Buffer-gas Loading and Magnetic Trapping of Atomic Europium.* PhD thesis, Harvard University, 1997.

[58] General purpose silver coated 0.5" diameter round mirror, New Focus 5153. New Focus, `http://www.newfocus.com/`.

[59] Continuum Surelite I-10. Continuum. `http://www.continuumlasers.com/`.

[60] Parafilm M barrier film. Pechiney Plastic Packaging, available from most scientific supply houses.

[61] Dimitri Egorov. *Buffer-gas cooling of diatomic molecules*. PhD thesis, Harvard University, 2004.

[62] Charlotte E. Moore. *Atomic Energy Levels As Derived From the Analyses of Optical Spectra*, Volume II. National Bureau of Standards, 1971. NSRDS-NBS 35.

[63] K. B. Blagoev and V. A. Komarovskii. Lifetimes of levels of neutral and singly ionized lanthanide atoms. *Atomic Data and Nuclear Data Tables* **56**, 1–40 (1994).

[64] Coherent Verdi V10 Laser. Coherent, Inc., Santa Clara, CA. `http://www.coherentinc.com/`.

[65] Coherent 899-21 Ti:Sa Ring Laser. Coherent, Inc., Santa Clara, CA. `http://www.coherentinc.com/`.

[66] WA-1500 Wavemeter. Burleigh Instruments, Inc., `http://www.burleigh.com/`.

[67] LBO crystal, Type I SHG, Brewster cut. Conex Systems, Inc., Pleasanton, CA.

[68] Laser Analytical Systems Wavetrain CW. No longer manufactured. Superseded by the Spectra-Physics Wavetrain, Spectra-Physics, Mountain View, CA, `http://www.splasers.com/`.

[69] Toptica Photonics DL 100 grating stabilized diode laser system. Polytec PI, Inc., Auburn, MA.

[70] Robert deCarvalho. *Inelastic scattering of magnetically trapped atomic chromium*. PhD thesis, Harvard University, 2003.

[71] Stablized HeNe Lab Laser 05 STP 901, Melles Griot. `http://www.mellesgriot.com/`.

[72] Research Electro-Optics, Inc., Boulder, CO. `http://www.reoinc.com/`.

[73] S. Gasiorowicz. *Quantum Physics*. John Wiley & Sons, 1974.

[74] Robert Michniak. *Enhanced buffer gas loading: cooling and trapping of atoms with low effective magnetic moments*. PhD thesis, Harvard University, 2004.

[75] J. B. Hasted. *Physics of Atomic Collisions*. Second edition. American Elsevier, 1972.

[76] Roman V. Krems, private communication.

[77] Matthew T. Hummon, private communication.

[78] W. J. Childs. Off-diagonal hyperfine structure in ^{45}Sc. *Physical Review A* **4**, 1767–1774 (1971).

[79] HITRAN database, URL `http://cfa-www.harvard.edu/HITRAN`.

[80] P. Hannaford and G. W. Series. Determination of hyperfine structures in ground and excited atomic levels by level-crossing optogalvanic spectroscopy: application to ^{89}Y. *Physical Review Letters* **48**, 1326–1329 (1982).

[81] J. Klos, M. F. Rode, J. E. Rode, G. Chalasinski, and M. M. Szczesniak. Interactions of transition metal atoms with He. *European Physics Journal D* **31**, 429–437 (2004).

[82] Joseph Callaway and Ernest Bauer. Inelastic collisions of slow atoms. *Physical Review* **140**, A1072–A1084 (1965).

[83] R. H. G. Reid and A. Dalgarno. Fine-structure transitions and shape resonances. *Physical Review Letters* **22**, 1029–1030 (1969).

[84] Harry Partridge and Jr. Charles W. Bauschlicher. Theoretical study of the low-lying states of $TiHe^+$, $TiNe^+$, $TiAr^+$, VAr^+, $CrHe^+$, $CrAr^+$, $FeHe^+$, $FeAr^+$, $CoHe^+$, and $CoAr^+$. *Journal of Physical Chemistry* **98**, 2301–2306 (1994).

[85] R. Burcl, R. V. Krems, A. A. Buchachenko, M. M. Szczesniak, G. Chalasinski, and S. M. Cybulski. RG + Cl(^2P) (RG = He, Ne, Ar) interactions: ab initio potentials and collision properties. *Journal of Chemical Physics* **109**, 2144–2154 (1998).

[86] Stephen R. Langhoff and Jr. Charles W. Bauschlicher. *Ab initio* studies of transition metal systems. *Annual Review of Physical Chemistry* **39**, 181–212 (1988).

[87] David J. D. Wilson, Colin J. Marsden, and Ellak I. von Nagy-Felsobuki. *Ab initio* structures and stabilities of doubly charged diatomic metal helides for the first row transition metals. *Journal of Physical Chemistry A* **106**, 7348–7354 (2002).

[88] H. Lew. Hyperfine structure and nuclear magnetic moment of Pr-141. *Bulletin of the American Physical Society* **15**, 795 (1970).

[89] J. Ferch, W. Dankwort, and H. Gebauer. Hyperfine structure investigations in Dy I with the atomic beam magnetic resonance method. *Physics Letters* **49A**, 287–288 (1974).

[90] W. Dankwort, J. Ferch, and H. Gebauer. Hexadecapole interaction in the atomic ground state of ^{165}Ho. *Zeitschrift fur Physik* **267**, 229–237 (1974).

[91] W. J. Childs, L. S. Goodman, and V. Pfeufer. Hyperfine structure of the $4f^{12}6s^2\ ^3H$ and ^3F terms of ^{167}Er I by atomic-beam, laser-rf double resonance. *Physical Review A* **28**, 3402–3408 (1983).

[92] Jack G. Harris, Robert A. Michniak, Scott V. Nguyen, Wolfgang Ketterle, and John M. Doyle. Buffer-gas cooling and trapping of atoms with small magnetic moments. *Europhysics Letters* **67**, 198–204 (2004).

[93] Frank Pobell. *Matter and Methods at Low Temperatures*. Springer-Verlag, 1992.

[94] 99.95% purity molybdenum wire, 2 mm diameter, from Alfa Aesar. Stock #10040. Alfa Aesar, `http://www.alfa.com`.

[95] 3 inch outer diameter, 0.5 inch thick BK7 windows with a two degree wedge and antireflection coatings at 425 and 532 nm. Esco Products Incorporated, `http://www.escoproducts.com`.

[96] 2.484 ± 0.001 inch diameter, 0.5 inch thick BK7 window, with a 2° wedge, each face wedged 1°. Esco Products part number ZV224500C. Esco Products Incorporated, `www.escoproducts.com`.

[97] MAX-R /209 coating on a 1 inch fused silica window, Melles Griot part number 02 WLQ 005/209. Melles Griot, `http://www.mellesgriot.com/`.

[98] SR560 Low Noise Preamplifier. Stanford Research Systems, `http://www.srsys.com/`.

[99] Anthony E. Siegman. *Lasers*. University Science Books, 1986.

[100] The index of refraction for fused-silica was found on the CVI Laser website, `http://www.cvilaser.com/Common/PDFs/Index_of_Refraction.pdf`.

[101] P. Aufmuth, H.-P. Clieves, K. Heilig, A. Steudel, D. Wendlandt, and J. Bauche. Isotope shift in molybdenum. *Zeitschrift fur Physik A* **285**, 357–364 (1978).

[102] S. Buttgenbach, M. Herschel, G. Meisel, E. Schrodl, W. Witte, and W. J. Childs. Ground-state hyperfine-structure of Mo-95 and Mo-97. *Zeitschrift fur Physik* **266**, 271–274 (1974).

[103] G. Olsson, T. Olsson, L. Robertsson, and A. Rosen. Laser and radiofrequency spectroscopy of the hyperfine-structure in the $4d^45s^2\ ^5D_{3,4}$ and $4d^55p\ ^7P_{2,3,4}$ states in Mo I. *Physica Scripta* **29**, 61–65 (1984).

[104] I. D. Setija, H. G. C. Werij, O. J. Luiten, M. W. Reynolds, T. W. Hijmans, and J. T. M. Walraven. Optical cooling of atomic hydrogen in a magnetic trap. *Physical Review Letters* **70**, 2257–2260 (1993).

[105] D. M. Harver, J. M. McGuirk, J. M. Obrecht, and E. A. Cornell. Thermally induced losses in ultra-cold atoms magnetically trapped near room-temperature surfaces. *Journal of Low Temperature Physics* **133**, 229–238 (2003).

[106] I. I. Sobel'man. *Introduction to the theory of atomic spectra*. English edition. Pergamon Press, 1972.